Numerical Model of Sarsia tubulosa Jellyfish

Developing a numerical model to explore efficient kinematics of the prolate Sarsia tubulosa jellyfish.

Hydrodynamics

Evan van der Weide

Delft University of Technology

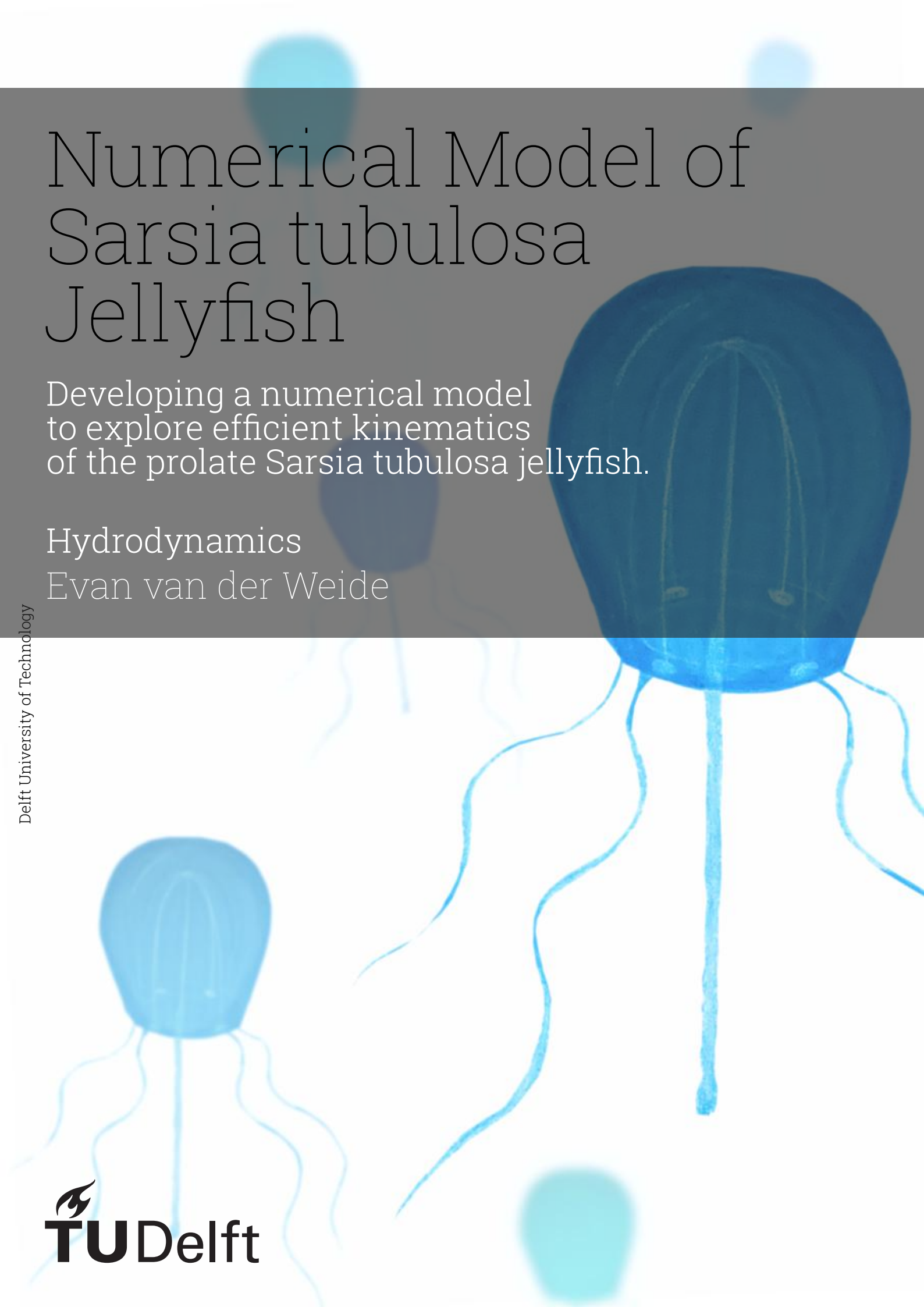

TU Delft

Numerical Model of Sarsia tubulosa Jellyfish

Developing a numerical model to explore efficient kinematics of the prolate Sarsia tubulosa jellyfish.

by

Evan van der Weide

to obtain the degree of Master of Science

at the Delft University of Technology,

to be defended publicly on Wednesday April 1, 2026 at 11:00 AM.

Student number:	5831393	
Project duration:	June 1, 2025 - April 1, 2026	
Faculty:	Faculty of Mechanical Engineering, Delft	
Thesis committee:	Dr. B. (Bernat) Font	TU Delft, supervisor
	Dr. A. (Artur) Lidtke	MARIN, supervisor
	Dr. A.J.L.L (Abel-John) Buchner	TU Delft

During the preparation of this thesis, the author used Large Language Models (LLMs) to support several aspects of the work. These tools were primarily used for literature summarisation, code verification and suggestions, and for improving the clarity and structure of written text. In addition, they were occasionally used as a sparring partner to reflect on ideas and approaches. All final decisions, interpretations, and conclusions presented in this thesis remain the authors' responsibility.

Cover: Klepelklokjes by A. de Graaf and S. Salverda
Style: TU Delft Report Style

TU Delft

Preface

This thesis was completed as part of the Master of Science programme in Marine Technology at Delft University of Technology. The research was carried out within the hydrodynamics branch. This model benefits the development of WaterLily and the field of biomimetic research on jellyfish. The development of a three-dimensional model of a physical problem proved to be a complicated process that continuously required out-of-the-box approaches.

I want to thank my supervisors, Bernat Font and Artur Lidtke, for their guidance and valuable feedback throughout this project. I enjoyed the cooperation and how they pushed me to a new level of scientific thinking. Their support and critical thinking have contributed to this project. I am also grateful to Matthias Claeys, Bart van Gelderen and Sake Salverda for the weekly discussions and technical support during the development of the computational model. Their support led to an acceleration in configuring the required software and administrative tasks.

Finally, I would like to thank my family, friends and girlfriend for their support during the completion of this thesis. The daily exchange of thoughts and ideas led to valuable new insights regarding the subject of this thesis. Their support led to the occasionally required boost of motivation and confidence during the project.

Evan van der Weide
Delft, March 2026

Abstract

Jellyfish exhibit one of the highest efficiencies observed in the animal kingdom, operating in the optimal Strouhal number range, despite their limited anatomy and morphology. Compared to other swimmers, such as salmon, the cost of transport of jellyfish can be up to 3.5 times smaller Gemmell et al. (2013). To understand their high efficiency, several numerical models have been developed. However, current numerical models that combine kinematics and hydrodynamics are limited by geometric simplifications, reduced dimensionality, and the absence of velar kinematics, complicating efficiency research. Accurate representation of realistic jellyfish kinematics, characterised by complex, time-varying geometry and active velar control, remains difficult. In particular, no validated fully three-dimensional model exists that simultaneously captures the full bell geometry and actively controlled velar kinematics of the *Sarsia tubulosa* jellyfish. This absence limits the ability to investigate efficiency metrics and three-dimensional vortex dynamics accurately.

This study presents the development, validation, and benchmarking of a new three-dimensional numerical model of *Sarsia tubulosa*, implemented in the computational fluid dynamics solver WaterLily. The geometry is represented using displacing control points connected by non-uniform rational B-splines (NURBS), enabling biologically accurate reconstruction of the bell, including active control of the (velum) kinematics. The Cartesian grid, combined with BDIM, avoids remeshing and enables the implementation of time-dependent kinematics by updating the signed distance function, reducing computational costs. Hydrodynamic forces are computed by integrating the pressure and viscous stresses over the body surface, where these stresses are obtained from the numerical solution of the incompressible Navier–Stokes equations. This avoids the analytical thrust and drag approximations commonly used in reduced-order approaches.

Model validation against experimental and numerical literature data demonstrated moderate agreement in both kinematics and dynamics. Normalised root-mean-square errors (NRMSE) of 0.113 were obtained for cavity volume and velar opening diameter, while force and velocity comparisons yielded values of 0.203 and 0.170, respectively. A velocity overshoot was observed during steady-state swimming, which is consistent with previous rigid-body medusan models. This problem was attributed to the absence of tentacle-induced drag and fluid–structure interaction phenomena, such as elasticity and passive dynamics. Applying prescribed kinematics was found to idealise the problem, as experimental jellyfish constantly adjust kinematics during swimming to achieve optimal vortex formation.

Kinematic variation studies found an optimal duty cycle in the range $0.4 < \gamma < 0.5$ for minimising the cost of transport (COT), whereas the biologically observed duty cycle is 0.2. This suggests that natural swimming is not optimised solely for energetic efficiency. In this study, the cost of transport was generally estimated to be low. Extended gliding intervals produced unrealistically low cost-of-transport values, indicating that inaccuracies in the force computation influence efficiency trends. Sensitivity analyses on the forces acting in this model confirmed that steady swimming behaviour is predominantly drag-controlled and tentacle-induced drag is not modelled. The absence of elastic force contribution in the cost definition lowers the cost of transport.

Overall, the developed model provides a computationally efficient three-dimensional framework for investigating trends and phenomena in *Sarsia tubulosa* swimming. It captures key hydrodynamic trends and vortex-formation phenomena, although modelling compromises were required for numerical feasibility. These compromises, combined with the use of rigid-body equations of motion, idealised kinematics, and the omission of elastic effects and tentacle dynamics, limit full physical realism to evaluate efficiency metrics. Recommendations for future work include improved force modelling, assessment of symmetry effects on vortex dynamics in 3D, higher-order geometric representations, and incorporation of passive elastic velum motion and tentacle effects.

Contents

Preface i

Abstract ii

Nomenclature viii

1 Introduction 1
- 1.1 Motivation . . . 1
- 1.2 Knowledge Gap . . . 1
- 1.3 Scope . . . 2
- 1.4 Research Questions . . . 2
- 1.5 Outline . . . 2

2 Literature Review 3
- 2.1 Biomechanics of Jellyfish Locomotion . . . 3
  - 2.1.1 Jellyfish Anatomy . . . 3
  - 2.1.2 Jellyfish Kinematics . . . 5
  - 2.1.3 Hydrodynamics of Jellyfish . . . 6
- 2.2 Validation of the Numerical Jellyfish Model . . . 8
  - 2.2.1 Overview of Modelling Approaches . . . 8
  - 2.2.2 Model Validation . . . 15
- 2.3 Control Problem of the Numerical Jellyfish Model . . . 16
  - 2.3.1 Flow Control Options . . . 16
  - 2.3.2 Applications of Flow Control . . . 17
  - 2.3.3 Efficiency Definitions for a Swimming Jellyfish . . . 17
- 2.4 Research on *Sarsia tubulosa* . . . 18

3 Methodology 20
- 3.1 The CFD Solver WaterLily . . . 20
- 3.2 The Numerical Jellyfish Model . . . 21
  - 3.2.1 Rescaling and Discretisation . . . 22
  - 3.2.2 Mass Conservation . . . 23
  - 3.2.3 Upsample Control Point Sets . . . 24
  - 3.2.4 Smoothing of Control Point Paths . . . 24
  - 3.2.5 Mapping to 3D . . . 25
  - 3.2.6 Prescribing Kinematics . . . 26
- 3.3 Simulation Framework . . . 27
  - 3.3.1 Governing Equations . . . 27
  - 3.3.2 Domain Size and Boundary Conditions . . . 30
  - 3.3.3 Signed Distance Function and Kernel Width . . . 32
- 3.4 Research Methodology . . . 33
  - 3.4.1 Convergence and Validation . . . 33
  - 3.4.2 Parametric Study Design . . . 34

4 Results 37
- 4.1 Numerical Verification . . . 37
  - 4.1.1 Grid Size . . . 37
  - 4.1.2 Domain Size . . . 37
  - 4.1.3 Time Step . . . 38
- 4.2 Validation . . . 39
  - 4.2.1 Geometry and Motion Validation . . . 39

4.2.2 Dynamics Validation . . . 41
4.3 Base Case . . . 42
4.3.1 A Comparison of the 2D and 3D Model . . . 42
4.3.2 Force Decomposition . . . 43
4.3.3 Vorticity and Wake Development . . . 44
4.4 Duty Cycle Variation . . . 46
4.5 Periodic Variation . . . 46
4.6 Gliding Intervals . . . 47
4.7 Combining Kinematic Variations . . . 47
4.8 Sensitivity Analyses on Hydrodynamic Forces . . . 48
4.8.1 Added Mass Coefficients . . . 48
4.8.2 Hydrodynamic Drag Force . . . 49

5 Discussion **51**
5.1 Methods . . . 51
5.2 Computational Feasibility . . . 52
5.3 Mechanics . . . 53
5.3.1 Kinematic and Dynamic Validation . . . 53
5.3.2 Kinematic Variation and Force Decomposition . . . 53
5.3.3 Vortex Dynamics . . . 54
5.4 Model Limitations . . . 55

6 Conclusions and Recommendations **56**
6.1 Conclusions . . . 56
6.2 Recommendations for Future Work . . . 57
6.2.1 Elaborate Sensitivity Analyses . . . 57
6.2.2 Elasticity Modelling . . . 57
6.2.3 Higher-order Geometric Representation . . . 57
6.2.4 Velum and Vorticity Studies . . . 57
6.2.5 Increasing Kinematic Datasets . . . 58
6.2.6 Reinforcement Learning . . . 58

References **59**

A Statistical Convergence Algorithm **63**

B Unfiltered Force Convergence **65**

C Vorticity Fields of Two-Dimensional Model **66**

D Vorticity Fields of Quarter Model **67**

List of Figures

2.1 Medusan Diversity across the medusozoa subphylum. Figure reproduced from (Costello et al., 2008) . . . 4
2.2 Hydromedusan swimming bell and muscle fiber structures. Figure reproduced from (Costello et al., 2021) . . . 4
2.3 Wake structure vorticity and velocity vectors of (A) Rowing Medusae and (B) Jetting Medusae. Reproduced from (Gemmell, Dabiri, et al., 2021) . . . 5
2.4 Oblate jellyfish vortex generation. Red areas represent stopping vortices, and blue areas represent starting vortices. Black arrows denote the direction of fluid circulation. Green arrows represent the direction of thrust contribution provided by the different vortex interactions. Figure reproduced from (Costello et al., 2021) . . . 7
2.5 The time variation of the bell morphology for the free-swimming hydromedusae S. tubulosa (upper) and A. victoria (lower) as reported by Sahin et al. (2009) . . . 10
2.6 Time histories of (a) the fineness ratio and (b) velocity, as determined by simulation in Park et al. (2015) or measured experimentally and reported by Colin and Costello (2002) 15

3.1 The realised enforcement of mass conservation. The fraction between the instantaneous volume V and the reference volume V_0, computed at $t = 0$, over a time range of 2 motion cycles, expressed as the phase ϕ. . . . 24
3.2 The constructed three-dimensional geometries of *Sarsia tubulosa* in the present model. The red area represents the location where the signed distance function equals 0. . . . 26
3.3 Evolution of the non-dimensionalised oral cavity volume for five kinematic configurations with a base case $T_1 = 1\,[s], \gamma = 0.4$, $\gamma = 0.2$ variation, $T_2 = 0.5\,[s], \gamma = 0.4$ variation, $T_g = 0.5\,[s], \gamma = 0.4$, variation and combined $T_2 = 0.5\,[s], T_g = 0.5\,[s], \gamma = 0.4$ variation. . . 27
3.4 The instantaneous force and velocity over 2 motion cycles for a case where the velocity is applied to the moving grid, and one where the grid does not move. The jellyfish does not translate in both cases. For the steady grid, there is only motion of the jellyfish in place. 28
3.5 The non-dimensional filtered and non-filtered hydrodynamic force signals over 2 motion cycles. A smoothing coefficient of $\alpha = 1 - e^{\frac{-\Delta t}{0.03\frac{TD}{U}}}$ was implemented for the smoothed signal. . . . 30
3.6 Comparison of non-dimensional forces between a full jellyfish model and a half/quarter geometry with a symmetry boundary condition replacing the other half/quarter. Comparisons are given for both the two-dimensional and three-dimensional cases. . . . 31
3.7 Two-dimensional slice of the three-dimensional domain with signed distance values of the geometry, at $t_i = 0$. . . . 32
3.8 Schematic overview of the region between the solid and fluid boundaries, reproduced from Lauber et al. (2022). The kernel width ϵ and the boundary smoothing region are shown. . . . 33
3.9 Seven base cases with $\gamma = 1 \rightarrow 12$ simulated to determine an optimal duty cycle of *Sarsia tubulosa*. . . . 35
3.10 Simulation matrices presenting the conducted simulations with the applied kinematic variations, studied with the present model. . . . 35
3.11 Simulation matrix presenting the simulations conducted where varying successive periods and gliding time are combined. . . . 35

4.1 Convergence statistics of the grid size D. The root mean square error (**a**) of the hydrodynamic force over 1 motion cycle (**b**), with respect to the finest grid size. . . . 38
4.2 The instantaneous hydrodynamic force signal for varying domain size over 1 motion cycle. 38

4.3 Convergence statistics of the numerical time step Δt. The root mean square error (**a**) of the hydrodynamic force over 1 motion cycle (**b**), for varying time step Δt, using the smallest time step as reference value. 39
4.4 Comparison of the geometry shape of the present model to the kinematic frames reproduced from Sahin et al. (2009) for 9 time steps in a single motion cycle. 40
4.5 Comparison of the oral cavity volume and velar opening diameter in the present model to the numerically computed volume reported by Lipinski and Mohseni (2009) over 2 motion cycles. 40
4.6 Comparison of the instantaneous non-dimensional velocity and drag coefficient to the numerically computed data in Sahin et al. (2009), respectively. The velocity of Sahin et al. (2009) was non-dimensionalised with the mean velocity U_{avg}. The WaterLily force coefficient was computed as $\frac{2Fx}{(UD)^2}$ 41
4.7 Comparison of the instantaneous fineness ratio and non-dimensionalised velocity to the experimental data reported by Colin and Costello (2002). The velocity of Colin and Costello (2002) was normalised with the mean velocity. 42
4.8 Comparison of the oral cavity volume in 2D, 3D and Lipinski and Mohseni (2009), over 2 motion cycles. 42
4.9 Comparison of the dynamical results between the 2D and 3D models over 3 motion cycles. 43
4.10 Force decomposition in the base case simulation. Presents pressure, viscous and added mass contributions over 2 fully evolved motion cycles. 43
4.11 Base case non-dimensional velocity and position of the geometry centre of mass. The blue area depicts the region of steady swimming, where a steady-state velocity is reached. The mean velocity is computed from this region. 44
4.12 Vorticity contours of the 3D model at several time steps in 1 fully evolved motion cycle. . . 45
4.13 Propulsive and efficiency metrics for varying duty cycle. 46
4.14 Propulsive and efficiency metrics for varying consecutive period T_2 with a duty cycle of $\gamma = 0.40, 0.45, 0.50$. 46
4.15 Propulsive and efficiency metrics for varying gliding interval T_g with a duty cycle of $\gamma = 0.40, 0.45, 0.50$. 47
4.16 Cost of transport for varying T_g and T_2 values with $\gamma = 0.4$. 47
4.17 The instantaneous velocity for added mass coefficients of several shape assumptions. . . 48
4.18 Decomposition of pressure and viscous forces during one actuation cycle and 5 periods of gliding. The Hoerner sphere drag is added as a reference value. 49
4.19 Comparison of the instantaneous drag force and velocity between the full WaterLily approach and a hybrid approach, implementing the Hoerner sphere drag as the viscous force on the model. 50

B.1 Convergence of the unfiltered force signal for varying time steps. 65

C.1 Vorticity fields of one evolved motion cycle of the two-dimensional model. 66

D.1 Vorticity contours of the quarter 3D model at several time steps in 1 fully evolved motion cycle. 67

List of Tables

3.1 Characteristic parameters of the *Sarsia tubulosa* model, reproduced from Sahin et al. (2009) 21
3.2 Kinematic settings of the base case. These are the same kinematic settings as in Sahin et al. (2009). 34

Nomenclature

Abbreviations

Abbreviation	Definition
2D	Two-dimensional
3D	Three-dimensional
AFC	Active Flow Control
ALE	Arbitrary Lagrangian–Eulerian
BDIM	Boundary Data Immersion Method
CFD	Computational Fluid Dynamics
CFL	Courant–Friedrichs–Lewy (condition)
CPU	Central Processing Unit
COM	Centre of mass
COT	Cost of transport
DC	Duty cycle
DRL	Deep Reinforcement Learning
FSI	Fluid–structure interaction
FR	Fineness ratio
GCL	Geometric Conservation Law
GPU	Graphics Processing Unit
LCS	Lagrangian Coherent Structures
LLM	Large Language Models
NS	Navier–Stokes (equations)
NRMSE	Normalised root mean square error
NURBS	Non-Uniform Rational B-Splines
PER	Passive Energy Recapture
PIV	Particle Image Velocimetry
Re	Reynolds number
RMSE	Root mean square error
SDF	Signed distance function
SIMPLE	Semi-Implicit Method for Pressure-Linked Equations
St	Strouhal number
UDF	User-defined function

Symbols

All variables are non-dimensional unless stated otherwise

Symbol	Definition	Unit
a	Acceleration of the centre of mass	[-]
A	Area	[-]
A	Added mass	[-]
C_{AM}	Added mass coefficient	[-]
C_d	Drag coefficient	[-]
C_p	Power coefficient	[-]
COT	Cost of transport	[-]
d	Signed distance function value	[-]
D	Drag	[-]

Symbol	Definition	Unit
D	Grid size	[-]
D_{bell}	Instantaneous bell diameter	[cm]
$D_{\max}$	Maximum bell diameter	[cm]
D_v	Velar opening diameter	[-]
$\mathbf{F}$	Hydrodynamic force vector	[-]
f	Instantaneous hydrodynamic force in translational direction	[-]
f	Actuation frequency	[1/s]
FR	Fineness ratio	[-]
h	Bell height	[-]
K	Biot-Savart kernel	[-]
L	Characteristic length scale	[-]
$\mathbf{n}$	Unit normal vector	[-]
n_{cycle}	Number of motion cycles	[-]
$NRMSE$	Normalised root mean square error	[-]
p	Pressure	[-]
p_{COM}	Position of centre of mass	[-]
P_{in}	Input power	[-]
P_{inst}	Instantaneous power	[-]
Re	Reynolds number	[-]
Re_k	Kinematic Reynolds number	[-]
r	Bell radius	[-]
s	Smoothed control-point path	[-]
St	Strouhal number	[-]
t	Time	[-]
Δt	Numerical time step	[-]
T	Thrust	[-]
T	Swimming period	[s]
T_1	Period of first motion cycle	[s]
T_2	Period of second motion cycle	[s]
T_{contr}	Contraction period	[s]
T_{exp}	Expansion period	[s]
T_g	Gliding interval period	[s]
$\mathbf{u}$	Fluid velocity vector	[-]
u_x	Centre-of-mass velocity in translation direction	[-]
U	Reference velocity	[-]
U_{avg}	Cycle-averaged swimming velocity	[cm/s]
U_{body}	Forward body velocity	[cm/s]
U_e	Jet velocity	[cm/s]
U_{ff}	Far-field velocity	[-]
U_∞ Uniform background flow		[-]
u_{scale}	Velocity scale	[-]
V	Volume	[-]
V_0	Initial bell volume	[-]
∇	Gradient operator	[-]
α	Exponential smoothing coefficient	[-]
α_{am}	Added mass coefficient	[-]
δ	Dirac delta function	[-]
ϵ	Kernel width	[-]
ϵ_V	Volume error	[-]
η_{Froude}	Froude efficiency	[-]
Γ	Circulation	[cm^2/s]

Symbol	Definition	Unit
γ	Duty cycle	[-]
μ	Dynamic viscosity	[-]
ν	Kinematic viscosity	[-]
ϕ	Phase (t/T)	[-]
ρ	Density	[kg/cm^3]
τ	Shear stress tensor	[-]
ω	vorticity strength	[-]
Ω_b	Solid domain	[-]
Ω_f	Fluid domain	[-]

1 Introduction

1.1. Motivation

Jellyfish combine unique anatomical structures with some of the highest propulsive efficiencies recorded in the animal kingdom, in terms of scaled swimming speed and cost of transport (Baldwin & Battista, 2021; Hoover et al., 2017). Rhythmic bell contractions and the generation of vortex rings are characteristic of jellyfish swimming. Jellyfish use fluid-dynamic interactions such as suction thrust, passive energy recapture, and virtual wall effects for locomotion (Costello et al., 2021; Dabiri et al., 2005). This forward motion is achieved while having limited muscle thickness and minimal neural complexity (Costello et al., 2008; Park et al., 2014).

Although jellyfish locomotion involves complex fluid–structure interactions that can be challenging to model, their anatomy and accessibility for observation make them ideal research subjects. Existing jellyfish research concerns the numerical modelling of hydrodynamics and the development of biomimetic propulsion systems (Costello et al., 2021; Frame et al., 2018; Xiao et al., 2013). Although advances in available computational fluid dynamics (CFD) methods and modelling have been made, designing accurate jellyfish models remains difficult. General challenges are model geometry construction, convergence reliability, simulation time and moving bodies that require adaptive mesh refinement or immersed boundary methods (Park et al., 2014). As a result, a detailed understanding of how specific kinematics and active flow control strategies contribute to their high swimming efficiency remains incomplete (Costello et al., 2021).

1.2. Knowledge Gap

A limitation across the literature is the absence of a non-simplified three-dimensional (3D) bell model, with a separately moving bell margin. All research applies simplification in some way, either through shape simplification (assuming a geometric parameterisation) or reduced dimensionality. Detailed morphological accuracy, in terms of having a flap and tentacles, is lacking, although several simplified options have been presented and discussed.

The flow-control mechanism of the jellyfish bell margin has been modelled as both active and passive across studies. As a result, several models exist, either employing active control via prescribed kinematics or passive control via fluid-structure interaction. No accurate 3D model, including velum control, is currently available. Wilson and Eldredge (2011) created a simplified model and stated that passive control is most efficient. However, the influence of bell margin kinematics on the propulsive efficiency of jellyfish has not been assessed with an accurate 3D model.

Achieving a validated 3D numerical jellyfish morphology model that can biologically accurately mimic jellyfish kinematics, including a kinematic control mechanism for bell and velum motion, would be an advancement in current modelling approaches. Determining the optimal kinematics to achieve the highest propulsive efficiency would provide new insights in this field of research. In particular, the influences of periodic variation and gliding intervals on efficiency have not been studied. As experimental hydrody-

namic data is available for hydromedusae in Colin and Costello (2002), it is straightforward to choose this type of jellyfish. Specifically, the *Sarsia tubulosa* species is chosen. To avoid the complexity of (semi-) passive bell margin modelling, the choice is made to control bell motion actively. As a result, the model cannot adequately capture passive effects, including velum deformation driven by the surrounding flow. Present studies have investigated the influences of Reynolds number, frequency and duty cycle variation, whereas periodic variation and gliding intervals have not been addressed. However, Colin and Costello (2002) experimentally found that these kinematics are continuously adjusted in jellyfish swimming.

1.3. Scope

The core objective of this research is to develop a validated numerical model of *Sarsia tubulosa* to help understand the kinematic and fluid dynamics phenomena underlying prolate jellyfish locomotion. This project aims to model the 3D shape and kinematics of *Sarsia tubulosa*, similar to previous work of Baldwin and Battista (2021), Colin and Costello (2002), Daniel (1983), McHenry and Jed (2003), Sahin and Mohseni (2009), and Sahin et al. (2009), in a biologically accurate way, by validating the model with available experimental and numerical data. Furthermore, an algorithm is developed to control the bell kinematics, to investigate the influence of kinematic settings on the propulsive efficiency of *Sarsia tubulosa*. The 3D model and kinematic algorithm are applied in a study to benchmark the numerical model performance.

An existing 2D numerical jellyfish model, developed by Dr Artur Lidtke, will serve as the foundation for research on jellyfish efficiency. This model numerically represents the flapping motion of the jellyfish bell responsible for jellyfish locomotion (Costello et al., 2021). Using motion data derived from the literature, this model will be adjusted to match known behaviours of both kinematics and fluid dynamics. Hydrodynamic simulations will be performed using WaterLily, a flow simulator developed by Weymouth and Font (2025).

1.4. Research Questions

A main research question was determined based on the defined knowledge gap:

"*How can a validated three-dimensional numerical jellyfish model be developed to investigate the locomotive efficiency of Sarsia tubulosa?*"

The following objectives are defined to answer the main research question.

1. Design a 3D numerical model in WaterLily that accurately describes the kinematics of a prolate jellyfish bell.
2. Develop and apply an active kinematics control mechanism to generate motion.
3. Combine the developed numerical model and control algorithm and benchmark the results through a kinematic variation study.

1.5. Outline

This report presents and discusses the methods used to develop the 3D numerical jellyfish model and the kinematic control algorithm, and the results obtained by combining them. All written and used code, data, and comparison materials are included in a reproducibility repository, available at https://github.com/evanvanderweide/WaterLily-Sarsia-tubulosa-Jellyfish-Modelling. Chapter 2 presents a literature review that assesses the current state of the art in jellyfish models and research. It includes an overview of the jellyfish biomechanics, numerical modelling methods, active control methods and validation data. Chapter 3 describes the methods used in this model to develop the geometry, kinematics and simulation environment. It also discusses the design of the parameter study. Chapter 4 presents the results of this research, including numerical convergence and model validation results. A base case, identical to that described by Sahin et al. (2009), is used in the following studies to assess convergence, validation, and locomotive efficiency. In Chapter 5, the results are discussed and related to the available literature. Finally, a conclusion for this study is presented, along with recommendations for future research.

2

Literature Review

2.1. Biomechanics of Jellyfish Locomotion

Before presenting the state of the art through a literature review, a theoretical framework is given to establish a basic understanding of jellyfish characteristics. Key anatomical, kinematic, and hydrodynamic concepts are introduced. Anatomy refers to the physical structures involved in movement. The kinematics describe how jellyfish move their physical structures during swimming cycles. The hydrodynamics explain how these movements generate thrust for jellyfish locomotion.

2.1.1. Jellyfish Anatomy

Medusae belong to the animal phylum Cnidaria, part of the Animalia kingdom. Medusae are part of the Medusozoa subphylum, which exhibits a biphasic life cycle consisting of a polyp stage and a free-swimming medusa stage. Medusae in the free-swimming stage are commonly referred to as jellyfish (Costello et al., 2021; Leclère & Röttinger, 2017). The diversity of the Medusozoa subphylum, in terms of size, shape, body design and propulsive mode, leads to another subdivision into classes, presented in Figure 2.1. Frequently studied classes in the field of kinematics and hydrodynamics are the Scyphozoa and Hydrozoa. Aurelia aurita (moon jellyfish) is an example species within this genus that has been widely investigated from the point of view of propulsion, because of its high propulsive efficiency (Villanueva et al., 2014).

Medusozoa jellyfish swim through rhythmic contractions of a muscular bell (Baldwin & Battista, 2021), but are distinguished by the presence (Hydrozoa) or absence (Scyphozoa) of a velum, which affects the mode of propulsion. A velum is a muscular, flap-like structure connected to the bell margin. Jellyfish, having a velum, typically have a prolate bell shape, applying jet propulsion for locomotion. Jellyfish, which do not have a velum, are generally oblate and often use a rowing mode of propulsion (Costello et al., 2008, 2021; Daniel, 1995). These propulsion modes are further explained in Section 2.1.2. Oblate bell shapes are characterised as a curved plate, tending to have a smaller fineness ratio, which is the ratio between bell height and bell diameter. Prolate jellyfish are generally small with a greater fineness ratio, shaped like a rocket (Dabiri et al., 2007; Gemmell, Du Clos, et al., 2021).

Medusae exhibit coordinated locomotion and interaction with surrounding fluid, while not having a brain, heart or skeleton (Schaadt et al., 2017). Their bodies are radially symmetrical, similar to an umbrella and consist mostly of water and mesoglea. Mesoglea is responsible for structural support and buoyancy, without generating any metabolic losses (Miles & Battista, 2019).

Figure 2.2 presents the anatomy of a Scyphozoa. The mesoglea, which separates the exumbrellar and subumbrellar surfaces of the bell, is shown. It houses several specialised cell types, including cnidocytes (stinging cells), mucocytes (mucus secretion), sensory cells, and, most importantly for locomotion, epitheliomuscular cells. The gastrodermis, the inner layer of the bell, lines the gastrovascular cavity, where digestion and nutrient absorption occur. It contains nutritive-muscular cells and gland cells, as well as additional cnidocytes (Zachariah & Mitchell, 2006).

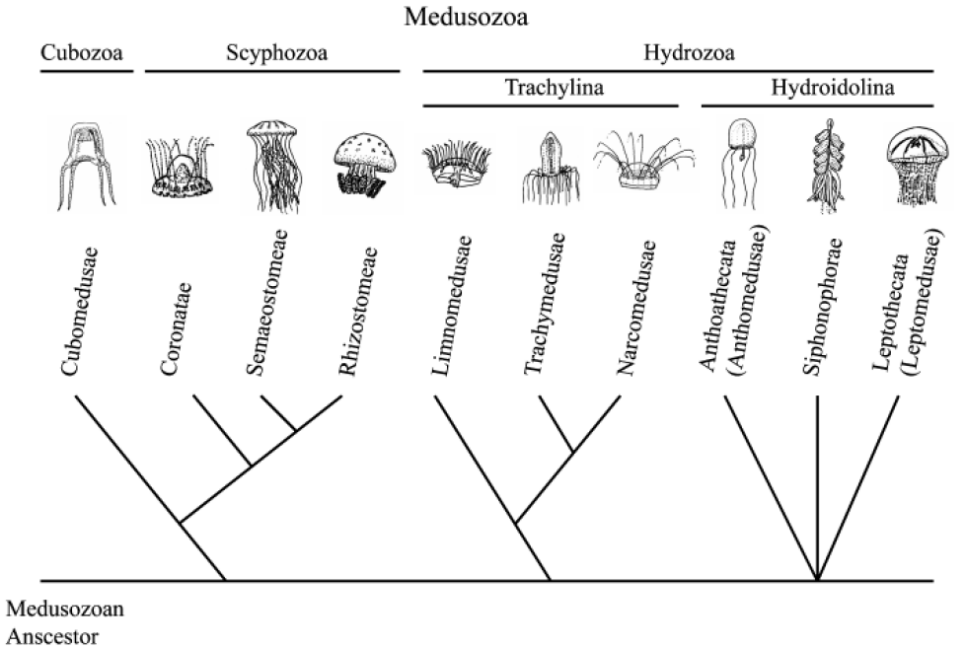

Figure 2.1: Medusan Diversity across the medusozoa subphylum. Figure reproduced from (Costello et al., 2008)

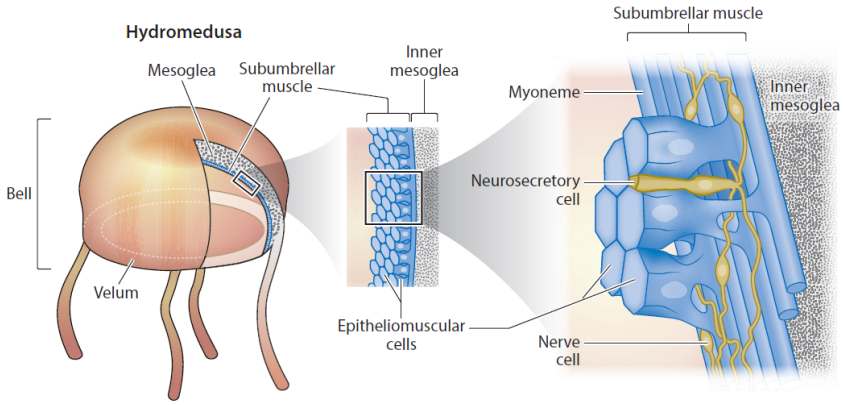

Figure 2.2: Hydromedusan swimming bell and muscle fiber structures. Figure reproduced from (Costello et al., 2021)

The subumbrellar surface at the inner underside of the bell is key to propulsion. It contains circular muscle fibres that can contract to reduce bell volume, leading to a flow of water (a jet), generating thrust. Radial fibres extend from the bell centre to its margin, the edges of the bell. At this location, sense organs are located for sensing light and orienting its swimming, contributing to finer control of bell deformation and directing flow (Gemmell, Troolin, et al., 2015; Zimmerman et al., 2019). Muscle groups consist of epitheliomuscular cells, unique to cnidarians. These groups combine epithelial and muscle functions within a single cell type. Though only one layer thick, they are sufficient to deform the bell due to its low mass. In addition to this low mass, jellyfish must move the mass of surrounding fluid water that is accelerated, representing the added mass (Daniel, 1983; Zachariah & Mitchell, 2006). Cnidarian muscles serve two purposes: (1) contractile functions to assist with locomotion, and (2) intracellular food digestion. The mesoglea contains elastic fibres that help the bell bounce back to its relaxed shape after contraction, enabling passive energy recapture. Neurosecretory cells are involved in transmitting signals for muscle contraction (Costello et al., 2008, 2021; Miles & Battista, 2019; von Montfort et al., 2023). Oral arms, often located near the centre underneath the bell, aid in feeding.

2.1.2. Jellyfish Kinematics

The anatomical constraints of jellyfish, such as minimal muscle mass, in combination with energetically efficient swimming, motivate research into their kinematics. Jellyfish propel themselves through rhythmic bell contractions (Baldwin & Battista, 2021). Regarding the mode of propulsion for locomotion, two groups can be distinguished. A rowing mode of propulsion, used by oblate jellyfish, and a jet propulsion mode, used by prolate jellyfish. Both modes are respectively given in Figure 2.3 as panels A and B, illustrating a contraction and relaxation phase within the swimming cycle. Jet propulsion is commonly observed in the classes Hydrozoa and Cubozoa (see Figure 2.1 for reference on these classes), while a rowing mode of propulsion is often found in Scyphozoa. However, there are exemptions as some Hydrozoa use a rowing mode of propulsion or a combination of both modes (Costello et al., 2008). The distinction between prolate and oblate jellyfish is generally applied to define kinematic properties (Colin & Costello, 2002; Costello et al., 2021; Dabiri et al., 2006). Figure 2.3 shows how prolate jellyfish possess a velum that shapes and accelerates a jet during contraction (B). In contrast, oblate jellyfish lack this structure and instead utilise vortex effects, a rowing mode of propulsion (A). The kinematics of both prolate and oblate jellyfish are further explained in this section.

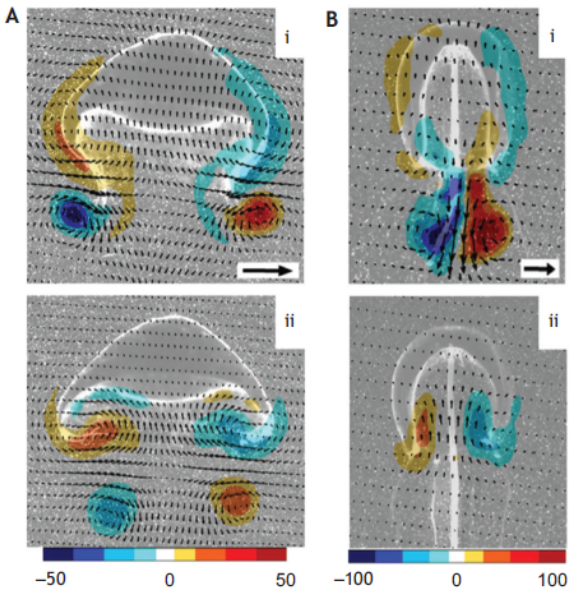

Figure 2.3: Wake structure vorticity and velocity vectors of (A) Rowing Medusae and (B) Jetting Medusae. Reproduced from (Gemmell, Dabiri, et al., 2021)

Rowing mode of propulsion

Extensive research has been conducted into how oblate jellyfish kinematics efficiently generate thrust (Bajcar et al., 2009; Costello et al., 2021; Dabiri et al., 2005; Gemmell, Du Clos, et al., 2021; Gemmell, Troolin, et al., 2015). Generally, oblate locomotion is described as a pulsation cycle, including a contraction stroke and a relaxation stroke, respectively for power and recovery (Dabiri et al., 2005). The initial state is a relaxed and fully expanded bell, after which the contraction phase starts, and a starting vortex is generated. This contraction phase is short in the context of a full motion cycle and leads to the starting vortex being expelled downstream. During a contraction, the mesoglea stores elastic energy, created by pushing the fluid to the centre and stretching the fibres. This stored energy leads to relaxation of the bell when the muscle tension drops (Pallasdies et al., 2019). During the relaxation phase, which takes longer, the stopping vortex is formed inside the subumbrellar cavity. This vortex generates a flow into the bell and enhances thrust through passive energy recapture. Interaction of this stopping vortex with the starting vortex induces a wall effect, further explained in Section 2.1.3 (Costello et al., 2021; Dabiri et al., 2005). The ratio of contraction time to full cycle time was defined as the kinematic duty cycle (γ) in Baldwin and Battista (2021). Oblate jellyfish exhibit low kinematic duty cycle, with contraction phases comprising only 10-20% of the pulsation cycle. Longer relaxation phases facilitate vortex interaction and passive energy recapture by spacing the starting and stopping vortex appropriately (Baldwin & Battista, 2021; Gemmell, Du Clos, et al., 2021).

The subumbrellar muscles drive contraction, primarily at the bell margin. In the relaxation phase, elastic recoil of the mesoglea restores the bell shape during relaxation (Bajcar et al., 2009; Chapman, 1999). The radial muscles are responsible for directing the flow. The bell margin does not follow the same deformation pattern as the rest of the bell. The differently moving bell margin, often acting semi-passively in response to fluid resistance, contributes to vortex ring geometry and feeding flows (Park et al., 2014; Villanueva et al., 2014).

Jet propulsion
The kinematic cycle of prolate jellyfish begins with a rapid contraction of the subumbrellar cavity, forcibly ejecting water through a narrow velar aperture, created through closing the velum 'flaps', as illustrated in Figure 2.3 B-I. This expulsion generates a high-speed jet and a starting vortex. Following contraction, the mesoglea recoils, and fluid passively refills the cavity during relaxation (Dabiri et al., 2006; Daniel, 1983). In contrast to oblate jellyfish, the duty cycle of prolate jellyfish is between 0.4 and 0.5, meaning that the contraction and relaxation phases are similar in length. This induces more frequent, high-velocity pulses, increasing energy costs (Dabiri et al., 2006). The velum plays an important role in reducing these energy costs. It controls aperture diameter during contraction and closes in the contraction phase, increasing pressure in the subumbrellar cavity to accelerate the jet (Daniel, 1983). The aperture expands during relaxation, letting the bell refill and shaping the stopping vortex ring.

2.1.3. Hydrodynamics of Jellyfish

Research has been conducted on both prolate (Baldwin & Battista, 2021; Daniel, 1983; Gemmell, Dabiri, et al., 2021) and oblate (Costello et al., 2021; Dabiri et al., 2005; Park et al., 2014) jellyfish. McHenry and Jed (2003) simulated the hydrodynamics of both paddle and jet mechanisms. Section 2.1.2 described the jellyfish kinematics responsible for certain hydrodynamic effects common in jellyfish locomotion. Most research agrees on three hydrodynamic processes underlying rowing and jet propulsion: suction thrust during bell contraction, passive energy recapture during bell relaxation, and a wall effect boost that occurs following an initial bell contraction (Costello et al., 2021).

Suction thrust is generated through bell contraction. Rearward acceleration of the bell margin, occurring during bell contraction, generates a high-pressure field in the subumbrellar region, while a low-pressure field is formed in the fluid surrounding the bell margin, illustrated in Figure 2.4. This low-pressure field moves from the bell apex to the margin, while a new high-pressure field arises at the apex (Daniel, 1983). Gemmell, Colin, Costello, and Dabiri (2015) identified that the net force forward results from the low-pressure field and not the high-pressure field in the subumbrellar region, thus implying suction thrust. The reason for this is that the jellyfish utilises the dominant low-pressure field to pull itself forward.

Passive Energy Recapture (PER) occurs during the relaxation cycle, when the subumbrellar cavity fills with fluid. This fluid is part of the stopping vortex generated during bell contraction, which moves into the subumbrellar cavity during expansion. This results in a volume increase in the subumbrellar cavity along with increased fluid velocities, pushing on the subumbrellar surface, creating a thrust force as depicted in Figure 2.4. Costello et al. (2021) and Gemmell et al. (2018) found that PER depends completely on the duty cycle of bell contraction, as a pause is required to build up this high pressure that can slowly push the bell forward and enable the medusa to ride the vortex-generated pressure gradient. In jetting jellyfish, pulsation cycles are shorter, allowing more rapid animal movement at the cost of being less energy-efficient, as it minimises PER contribution (Gemmell et al., 2018; Hoover et al., 2019). Hoover et al. (2019) added that the elastic properties of the jellyfish bell are impacting PER contribution, being able to increase or decrease it.

The virtual wall effect is another utility of jellyfish to increase thrust and efficiency. This results from opposing vortices that create a 'virtual wall'. A stopping vortex from the previous pulsation cycle serves in the same way as a virtual vortex during wall effect performance enhancement. The stopping vortex accumulates fluid at the propulsive surface, generating higher pressures at the underside of the bell margin. These high pressures increase the thrust force during the contraction phase (Costello et al., 2021; Gemmell, Du Clos, et al., 2021). This thrust contribution is shown in Figure 2.4.

A special note should be made on the effect of **added mass**, as this phenomenon can be used to reduce drag. This can be achieved through careful timing of the kinematic cycle to change the volume of a

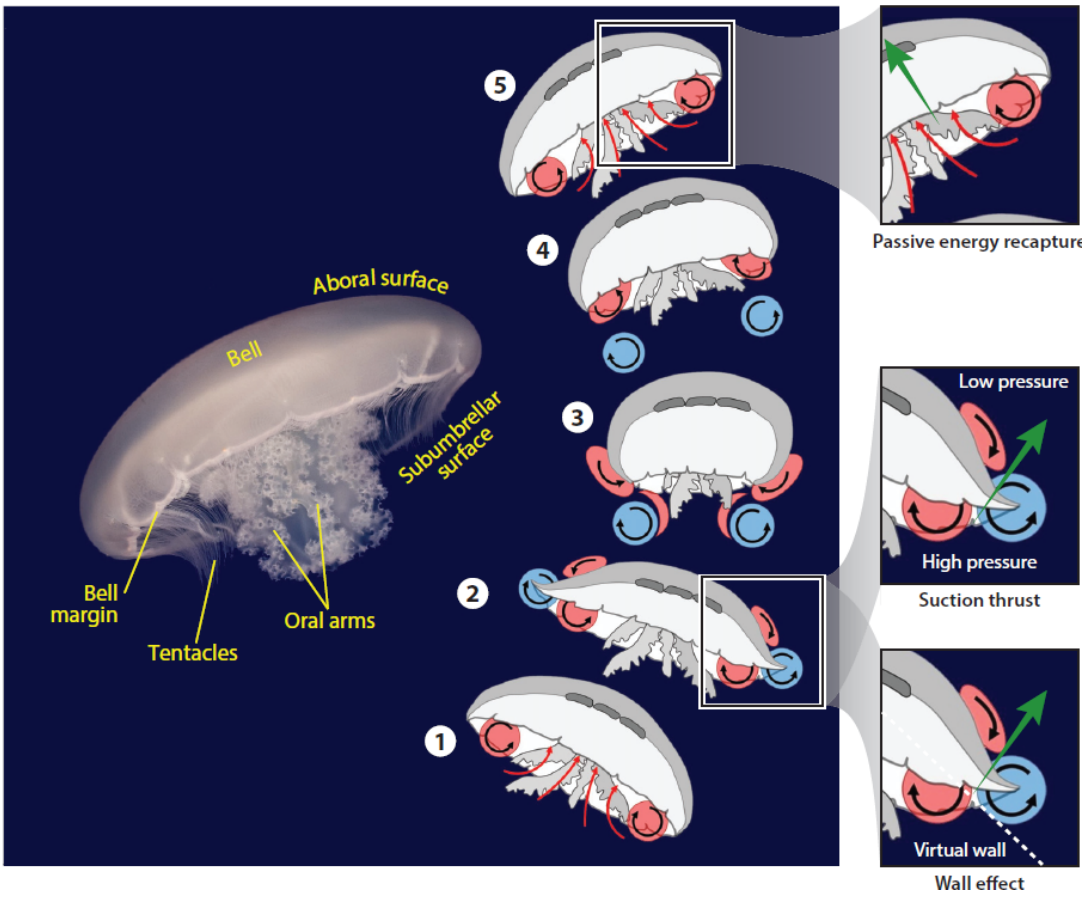

Figure 2.4: Oblate jellyfish vortex generation. Red areas represent stopping vortices, and blue areas represent starting vortices. Black arrows denote the direction of fluid circulation. Green arrows represent the direction of thrust contribution provided by the different vortex interactions. Figure reproduced from (Costello et al., 2021)

submerged body, recovering added-mass kinetic energy and therefore reducing drag. This phenomenon is further explained in the work of Giorgio-Serchi and Weymouth (2016) and could present itself during jellyfish research.

Rowers produce their forward momentum through the pulsation cycle as shown in Figure 2.4, implementing the described hydrodynamic effects. They produce thrust during both the contraction phase, through suction thrust and a virtual wall, and the expansion phase, through PER, making them highly efficient (Pallasdies et al., 2019).

Jet propulsion induces similar effects, although its main propulsive force comes from the hydrodynamic phenomenon '**jet expulsion**', a form of active thrust where pulses of fluid are periodically ejected. Closing the velum reduces the aperture diameter, increasing the pressure in the subumbrellar cavity, inducing a high-velocity flow (jet) through the aperture (Dabiri et al., 2005). A higher pressure arises at the subumbrellar surface, while momentum is sent downstream, and thrust forward is generated. Jet propulsion makes less use of energy recapture due to its '50-50' duty cycle, making jetting jellyfish locomotion less efficient (Costello et al., 2008; Dabiri et al., 2006; Gemmell, Dabiri, et al., 2021). Pulsed jetting is a solution that could increase this efficiency; however, it requires adjusting the duty cycle (Baldwin & Battista, 2021; Costello et al., 2021). However, oblate jellyfish are the more energetically efficient type, although they produce less velocity and induce higher fluid disturbances (Dabiri et al., 2006).

Reynolds number of jellyfish

The Reynolds number (Re) of jellyfish depends on the type, whether it is prolate or oblate. Herschlag and Miller (2011) applied Reynolds numbers between 1 and 320 for prolate jellyfish. Colin and Costello (2002) used Reynolds numbers between 1 and 500 and stated that the Reynolds number is closely related to the forward velocity of jellyfish and peaks at the end of bell contraction. Thus, Reynolds

numbers can vary during the kinematic duty cycle. Oblate jellyfish have a higher Reynolds number, as they are larger. Baldwin and Battista (2021) found Reynolds numbers between 3000 and 5000 for large oblate jellyfish, while Park et al. (2014) used a Reynolds number of 425 for the oblate jellyfish Aurelia aurita. A lower Reynolds number results in a laminar flow instead of a turbulent flow, which simplifies the fluid dynamics. This could make a flow solver more efficient and accurate.

2.2. Validation of the Numerical Jellyfish Model

2.2.1. Overview of Modelling Approaches

Jellyfish propulsion has been extensively studied across various disciplines using a range of analytical, experimental, and computational approaches. Costello et al. (2021) stated that jellyfish mechanics are not easily modelled, and incorporating detailed biological information is key for successful computational fluid dynamics, instead of relying on assumed kinematic or material traits.

Jellyfish Morphology Modelling

Current jellyfish modelling commonly simplifies bell morphology through applying hemi- or semielliptical profiles. For example, Baldwin and Battista (2021) and Hoover and Miller (2015) adopted a semi-elliptical profile parameterisation as in Equation 2.1, where (x_c, y_c) is the centre of the ellipse, a is the length of the halfwidth of the bell, and $b + d$ is the height of the bell. Daniel (1983) and Park et al. (2014) added the third dimension through the use of a hemi-elliptical profile parameterisation as in Equation 2.2. The parameterisations presented here all assume a constant fineness ratio through the contraction cycle, as a and b are not time-dependent. An ellipsoidal parameterisation, although easily applicable in numerical simulation, imposes limitations. A prolate jellyfish may resemble a hemi-elliptical bell in its relaxed phase (Dabiri & Gharib, 2003); however, it is significantly different in shape during the contraction phase. According to Bajcar et al. (2009) and Dabiri and Gharib (2003), an oblate jellyfish differs even more in shape, confirmed by Figure 2.3. A prolate jellyfish undergoes smaller deformations during actuation and is therefore better modelled through a hemi-ellipsoid than an oblate jellyfish (Villanueva et al., 2014).

$$\frac{(x - x_c)^2}{a^2} + \frac{(y - y_c)^2}{b^2} = 1 \quad \text{for } y \geq y_c - d \tag{2.1}$$

$$\frac{(x - x_c)^2 + (y - y_c)^2}{a^2} + \frac{(z - z_c)^2}{b^2} = 1 \quad \text{for } z \geq 0, \tag{2.2}$$

Alben et al. (2013) parametrised the bell shape as a tangent angle function depending on the arc length s of the bell and the time t, as given in Equation 2.3. This determines the geometry with a single control parameter, β, which governs the kinematics of the bell through adjusting the bell shape. Alben et al. (2013) also designed an analytical model assuming the bell to be a cylinder with time-dependent radius.

$$\theta(s, t) = -1.55(1 - e^{-\frac{s}{\beta(t)}}) \tag{2.3}$$

Hoover and Miller (2015) and Hoover et al. (2017, 2019) implemented a method where prolate jellyfish are modelled as a hemi-ellipsoid in its initial state, but it deforms under mechanical forces, through stiffness and energy transfer. Bell kinematics can now be quantified through material stiffness, mesh deformation, or oscillation frequency, and not only through a time-dependent fineness ratio, thereby increasing the biological accuracy of the model. In the work of Hoover and Miller (2015) and Hoover et al. (2017, 2019), the bell margin could passively deform under fluid forces; it was modelled as a ring of uniform thickness. Villanueva et al. (2014) modelled jellyfish by gathering points from image tracking. A separate, flexible material was used for the bell margin to induce passive margin motion. To quantify this deformation, it applied the curvature of the exumbrellar surface. However, similar to Hoover and Miller (2015) and Hoover et al. (2017, 2019), this can still only capture passive movements. Bajcar et al. (2009) and Dular et al. (2009) fitted 6th-order polynomials to captured video imaging of the bell margin deformation, to use as input into computational fluid dynamics (CFD) simulations. This enables implicit flap motion. Feitl et al. (2009) and Miles and Battista (2019) included tentacles through Lagrangian points (representing the structure) tethered together by a virtual spring (a similar approach was adopted by Baldwin and Battista (2021)) and lappets at the bell margin. In all three papers, it was concluded that adding these particles induced vortex and boundary layer interactions, impacting hydrodynamics and

propulsion. Wilson and Eldredge (2011) used an approach significantly different from others, modelling the jellyfish as a 2-dimensional articulated system of linked rigid bodies connected by hinges. It consists of seven buoyant, rigid elliptical bodies connected by six torsional hinges. Wilson and Eldredge (2011) states it as not biologically realistic, but loosely inspired by jellyfish mechanics, and it is specifically applied to investigate passive-active mechanical trade-offs in jellyfish swimming.

In general, the fineness ratio, the ratio between bell height and diameter as in Equation 2.4, is utilised as a quantification of the bell shape (Bajcar et al., 2009; Baldwin & Battista, 2021; Hoover et al., 2019; Park et al., 2014). Dabiri and Gharib (2003) suggested that relying on the fineness ratio alone is insufficient to describe bell kinematics and that incorporating the location of maximum diameter may improve kinematics description. Colin and Costello (2002) added a second morphological variable, the velar aperture area ratio. They assumed a circular cross-section and defined the quantification as the ratio between the velar aperture diameter squared and the bell diameter squared.

$$FR = \frac{h}{D_{bell}} \tag{2.4}$$

A limitation across the literature is the implementation of a non-simplified three-dimensional bell model, with a separately moving bell margin. All research applies simplification in some way, either through shape simplification or reducing dimensionality. Detailed morphological accuracy, in terms of having a flap and tentacles, is nonexistent, although several simplified options have been presented and discussed.

Jellyfish Kinematics Modelling

Numerical jellyfish models commonly imitate jellyfish kinematics from experimental findings gathered through image tracking. Coordinated muscle contraction and mesogleal recoil resulted as key kinematics for the thrust generation process and therefore serve as a foundation in kinematics models. These kinematics are governed by the material properties of the mesoglea and the radial muscle fibres. Megill et al. (2005) stated that the fibres alone can account for the energy required to passively refill the subumbrellar cavity during relaxation, which was confirmed through video tracking in Bajcar et al. (2009). Some numerical models incorporate material properties, such as elasticity and stiffness, as well as deformation dynamics, including contraction and recoil, to replicate the kinematics.

Each kinematic model requires a method that can make the jellyfish move. Sahin et al. (2009) modelled swimming hydromedusae by digitising the outline of the medusan bells with 2D non-uniform rational B-spline curves (NURBS). By directing a laser sheet through the central axis of the medusae and recording its movements in the laser sheet, the hydromedusa locomotion in 2D was derived. The resulting digitised bell kinematics for free-swimming hydromedusae are given in Figure 2.5, with the parameter T as the period of one cycle and the small t representing which point of the cycle each line corresponds with. Sahin and Mohseni (2009) presents their developed two-dimensional axisymmetric computational model to simulate the propulsion of *Sarsia tubulosa*. The flow field was resolved using a finite-volume CFD approach under the assumption of incompressible, laminar flow at a moderate Reynolds number. Axisymmetry reduced the three-dimensional problem to a meridional plane while retaining the essential jet dynamics. Hydrodynamic forces were obtained from the computed pressure and viscous stresses on the bell surface. The translational motion of the medusa was determined by coupling these forces to the jellyfish's dynamics with Newton's second law. Bajcar et al. (2009) used 6th-order polynomials to copy experimentally observed jellyfish kinematics. Data-driven simulations that replicate experimentally observed kinematics highlight the problem of insufficient modelling of the bell margin motion (Villanueva et al., 2014). Wilson and Eldredge (2011) found that these flaps significantly enhance thrust production. Therefore, having a standardised kinematic model lacking this flap could underestimate the propulsive properties of jellyfish. To account for this, Wilson and Eldredge (2011) described kinematics as sinusoidal changes in hinge angles, based on biological data, thus actively applying motion to the model. Some hinges could be made passively responsive using torsion springs, enabling passive motions. Hoover and Miller (2015) and Villanueva et al. (2014) also described it as passive motion. Other research models the bell margin motion actively. For example, McHenry and Jed (2003) used a sawtooth function to define kinematic equations for the motion of the margin angle, bell height and bell diameter. The margin angle can then be actively adjusted during contraction cycles.

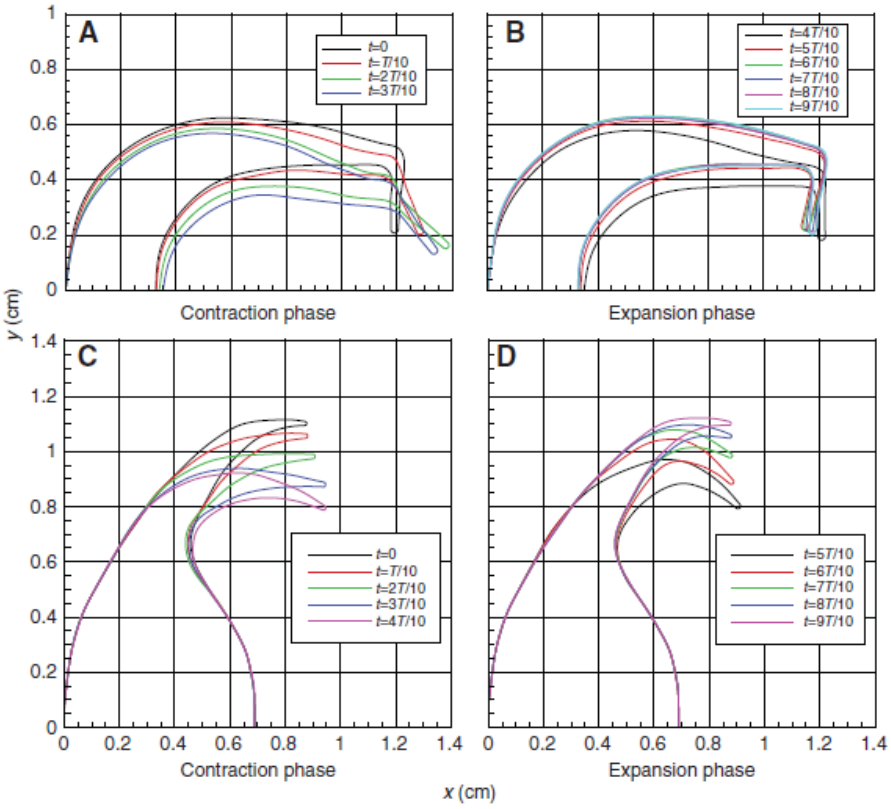

Figure 2.5: The time variation of the bell morphology for the free-swimming hydromedusae S. tubulosa (upper) and A. victoria (lower) as reported by Sahin et al. (2009)

Other models also implement the elastic properties of jellyfish. Hoover et al. (2017, 2019) developed a spatially varying model, implementing an elastic modulus gradient in the vertical direction. Hoover and Miller (2015) and Hoover et al. (2017, 2019) initiated the bell's contraction by applying a time-varying tension to the bell margin, while the expansion phase is initiated by removing the applied tension such that the stored elastic energy drives the expansion of the bell. Other reduced-order models (ROM), used by Demont and Gosline (1988) and Megill et al. (2005), approached elasticity using spring-mass-damper analogies, creating a system with uniform parameters at specific points. Likewise, Baldwin and Battista (2021) and Miles and Battista (2019) discretised the hemi-ellipsoid and connected the points through virtual springs and beams with individual elastic properties. Baldwin and Battista (2021) applied varying spring stiffness across points of the discretised hemi-ellipsoid, relative to the preferred geometric configuration (the initial hemi-ellipsoid state), to account for varying elastic properties. It can deform by dynamically changing the spring resting lengths and then initiate contraction. Park et al. (2014) assessed the influence of elastic moduli and found that the bell deformations were affected by the tension modulus but not the bending modulus. The swimming performance was shown to be dependent on the bell elasticity, and an optimal elasticity value was identified that maximised the propulsive efficiency. This illustrates that using a prescribed kinematics model could underestimate the propulsive efficiency of jellyfish. However, applying a passively responsive model requires a fluid-structure interaction (FSI) approach, significantly increasing simulation complexity and time.

While current models increasingly capture the coupling between active muscular contraction, passive elasticity, and fluid dynamics, many are constrained in some way. Some models remain two-dimensional or exclude passive elastic motion, while others assume uniform elasticity and stiffness. A biologically accurate representation of bell margin motion within a fully three-dimensional bell model is not available, although both components have been explored independently. Applying a method where the bell kinematics are digitised into numerical points and connected through NURBS offers an accurate replication of bell motion, including separate bell margin motion. This method does not require an FSI approach, as the kinematics are predefined. The consequence of this is that passive motions are not simulated,

so the bell does not move as a result of the flow around it. This complicates capturing the effects of passive energy recapture during simulations.

Dabiri and Gharib (2003) stated that each kinematic assumption is associated with a quantifiable error, which should be accounted for during research. Dabiri et al. (2005) quantitatively evaluated the thrust production mechanisms. They applied the wake vortex ring volume relative to the ejected fluid volume as a quantification of the vortex generation. These volumes were derived from measuring the subumbrellar surface from video analysis. Together with Daniel (1983), the anticipation is made that volume is the most useful index of swimming thrust in field measurements. A recently identified phenomenon involves a reduction in flow velocity caused by vorticity cancellation between starting and stopping vortices, which arises from suboptimal stroke timing (Hoover et al., 2019). This suggests that some form of stroke timing quantification is required in the kinematics model.

Herschlag and Miller (2011) and Wilson and Eldredge (2011) used a 'kinematic Reynolds number' as given in Equation 2.5, providing a measure of inertial versus viscous effects arising from the motion of the bell. McHenry and Jed (2003) quantified bell kinematics in terms of fineness ratio, margin angle and swimming speed. Dabiri et al. (2006) quantified kinematics through cavity volume and velar diameter as a function of time.

$$Re_k = \frac{\rho U_{body} D}{\mu} \tag{2.5}$$

Hydrodynamic and Fluid-Structure Interaction Modelling

The swimming kinematics of jellyfish generate thrust through interaction with the surrounding fluid dynamics. These interactions have been modelled in various ways. Daniel (1983) and McHenry and Jed (2003) modelled the sum of thrust, drag, added-mass (acceleration) force, and reaction forces arising from body motion as in Equation 2.6. McHenry and Jed (2003) calculated these forces through mathematical equations of the bell shape and kinematics. The resulting swimming velocity is computed numerically using a variable-order Adams–Bashforth–Moulton solver. Compared to experimental results, this method results in quite accurate predictions for prolate jellyfish. However, it applies prescribed motions and does not solve for the fluid equations, making it a reduced-order method. It was also noted by Colin and Costello (2002), Daniel (1983), and McHenry and Jed (2003) that this method may overestimate the jellyfish dynamics.

$$T + D + A + F = 0 \tag{2.6}$$

Other models do include the step of numerically solving simplified Navier-Stokes equations that govern hydrodynamics. Simplifications through assuming an incompressible, viscous flow of a Newtonian fluid are generally used (Bajcar et al., 2009; Hoover et al., 2017; Miles & Battista, 2019; Park et al., 2014). These assumptions are generally acceptable for lower Mach numbers, which is the case for jellyfish (≤ 0.5), as its velocity is significantly lower than the speed of sound through water. The Navier-Stokes equations for an incompressible viscous flow are shown in Equation 2.7 and 2.8, respectively representing the conservation of mass and momentum. The mass conservation equation ensures that fluid density remains constant (incompressibility), while the momentum equation describes how fluid motion evolves in response to pressure, viscous, and inertial forces.

$$\nabla \cdot \mathbf{u} = 0 \tag{2.7}$$

$$\rho_0 \left(\frac{\partial \mathbf{u}}{\partial t} + \mathbf{u} \cdot \nabla \mathbf{u} \right) = -\nabla p + \mu \nabla^2 \mathbf{u} + \mathbf{f} \tag{2.8}$$

Numerical solvers are available to compute the Navier-Stokes equations, which will be addressed below. In addition to the fluid model, the structure also requires modelling, depending on the applied approach. In structure modelling, two main approaches are used: kinematic and dynamic. Kinematic models, used in Bajcar et al. (2009), prescribe motion directly and apply it to the fluid without solving structural equations. Thus, only the Navier-Stokes equations need to be solved. Dynamic models, used in Hoover et al. (2017) and Park et al. (2014), solve structural force equations to determine body deformation and response, and couple the results to the fluid equations.

Methods using prescribed motion only require a solver for the Navier-Stokes equations. Alben et al. (2013) utilised a 2D vortex-sheet model to simulate the fluid flow around the jellyfish bell during swimming. This model accurately captures vortex dynamics. They assumed an inviscid flow and used a bound axisymmetric vortex sheet as a boundary condition for the bell surface, representing a discontinuity in fluid velocity. For the analytical assumption-based bell model, they applied a potential-flow model, thus assuming no vorticity. Bajcar et al. (2009) applied a 2D semi-implicit method for pressure-linked equations (SIMPLE) algorithm, described by Baliga and Patankar (1980) as a convection-diffusion problem solver. This method divides the domain of interest into three-node triangular elements. Control volumes are generated between triangle centroids and used in conservation equations. Baliga and Patankar (1980) stated that this method is mainly applicable for 2D problems. Sahin and Mohseni (2009) applied an axisymmetric geometrically conservative arbitrary Lagrangian-Eulerian (ALE) formulation, obeying the geometry conservation law. In this method, the mesh follows the interface between the fluid and solid boundary and the governing equations are discretised on an unstructured moving and deforming mesh. Gemmell, Dabiri, et al. (2021) stated that this method enables control of parameters of the numerically simulated organisms, and isolating specific effects becomes possible. Oppositely, Sotiropoulos and Yang (2014) stated it is cumbersome for problems with large deformations. Wilson and Eldredge (2011) used a 2D viscous vortex particle method to solve the fluid flow for its prescribed motions model. According to Eldredge (2007), this method solves the Navier-Stokes equations using a fractional step procedure. Vorticity is carried by particles that interact with one another, exchanging

strength to simulate convection and diffusion. Slip along the body is corrected by introducing a vortex sheet and diffusing it into nearby particles. Particles are regularly remeshed to a Cartesian grid to maintain consistency. The Kelvin's circulation theorem is enforced by recovering circulation lost to the body. The method is validated with insect-inspired flapping and fish-like swimming cases (Eldredge, 2007).

The methods that assume passive bell motion generally apply FSI methods, where the structural equations should be solved in addition to the Navier-Stokes equations. The Immersed Boundary Method (IBM) is a fluid solver framework. An example of the method is described by Sotiropoulos and Yang (2014) and used in Hoover et al. (2017) and Park et al. (2015), which solves the Navier-Stokes equations on a fixed background grid. The method represents structural interactions through independent surface meshes that are accounted for in the governing equations of the grid. This method couples the two by applying forces from the structure to the fluid. The fluid and structure equations can be solved through different solvers within this framework. Hoover et al. (2017) applied an IBM where FSI is described in an Eulerian frame and structural deformations and stresses in a Lagrangian frame. A finite difference formulation is used for fluid modelling and a finite element formulation for structural modelling in 3D, allowing for passive structural deformation. Park et al. (2015) solved the fluid governing equations using the fully implicit decoupling method as described by Kim et al. (2002). Velocity and pressure are decoupled and solved separately, allowing for a more efficient solution to the problem. The solid motion equation is derived by the energy method and solved using an iterative method. Again, the fluid is solved in an Eulerian domain and the structure in a Lagrangian domain. Park et al. (2015) applied the no-slip condition at the boundaries of the computational domain. The domain was scaled with the diameter of the jellyfish. They conduct convergence studies by assessing the fineness ratio and velocities for different domains and grid sizes. A 3D penalty IBM is used in Park et al. (2014). This method separates a massless and a massive part of the immersed boundary and links them through a virtual (stiff) spring with damping. This spring is given a 'penalty' force to enforce that the massive and massless parts have the same location and velocity. Park et al. (2014) used a fractional step method to solve the fluid motion equation, which decouples coupled terms and divides time steps into fractional time steps to improve computation. It uses the subdivision finite element method, described in Cirak et al. (2000), to solve the solid motion equation. The equations are coupled by adding a momentum force term.

Baldwin and Battista (2021) and Herschlag and Miller (2011) used the IBM developed by Peskin (2002) in 2D. Implication of the IBM, as described by Peskin (2002), applies an Eulerian frame for the fluid and a Lagrangian frame for the structure. These frames are coupled through implicitly enforcing the dynamic and kinematic boundary conditions on the immersed structure through Equation 2.9 and 2.10. Equation 2.9 enforces the no-slip condition by making the structure velocity, $\frac{\partial \mathbf{X}}{\partial t}(s,t)$, match the local fluid velocity on the structure location. Equation 2.10 describes the force of the structure on the fluid through the force per unit length $\mathbf{f}(r,t)$, implicitly representing the dynamic boundary condition through a force sum. In both equations, a 2D Dirac delta function is used to translate quantities between the frameworks, and s is a state function representing the kinematic state.

$$\frac{\partial \mathbf{X}}{\partial t}(r,t) = \int \mathbf{u}(\mathbf{x},t)\,\delta(\mathbf{x}-\mathbf{X}(r,t))\,d\mathbf{x} \tag{2.9}$$

$$\mathbf{F}(\mathbf{x},t) = \int \mathbf{f}(r,t)\,\delta(\mathbf{x}-\mathbf{X}(r,t))\,dr \tag{2.10}$$

WaterLily.jl, an incompressible viscous flow solver, uses the Boundary Data Immersion Method. It is implemented as described by Weymouth and Font (2025) and can be applied to 2D and 3D problems. It is an incompressible viscous flow solver that implements the finite volume method. The solver does not apply a structure solver that can account for the passive elastic behaviour of the structure. Instead, it uses prescribed motion by applying signed distance functions and mapping of the solid boundary to a new location every time step. Thus, motions are defined through functions instead of being a result of a structural equation. The fluid velocities at the solid boundary are equalised to the solid velocities, creating a single equation that is valid over the entire space. The benefit of this method is the possibility of 3D simulations. A limitation of this method is that elasticity cannot be modelled as the solid equations are not implemented in the method. It would require prescribed kinematics to work. This simplifies the problem significantly, as no FSI has to be computed, while accuracy may be preserved by digitising actual jellyfish kinematics from experimental work.

A typical quantification of flows is the Reynolds number. It can be used to determine the flow regime of a fluid and represents the balance between inertial and viscous forces. Park et al. (2014) stated that Reynolds numbers of 50 to 500, a state in which both inertial and viscous forces are present, are representative of natural jellyfish swimming. Herschlag and Miller (2011) agreed with this and stated that organisms do not use reciprocal methods of locomotion below a Reynolds number of $\mathcal{O}(1)$. They define the Reynolds number as a function of the average forward velocity, given in Equation 2.11.

$$Re_m = \frac{\rho U_{avg} D}{\mu} \tag{2.11}$$

Dabiri et al. (2005), Park et al. (2015), and Sahin et al. (2009) presented a formulation for the vortex formation time as in Equation 2.12. This indicates the vortex formation process by the ejected fluid. It is the fraction between jet velocity and diameter integrated over time.

$$t^* = \int_0^t \frac{U_e(\tau)}{D_e(\tau)} \, \mathrm{d}\tau \tag{2.12}$$

Dabiri et al. (2006) applied vortex formation time/number as defined, but expresses it in measured terms. It also presents a governing equation to derive a locomotive force estimation, which is later used for quantification. This equation is given in its most general form in 2.13, where $\mathbf{I}$ is the identity matrix, C_{AM} is the added mass coefficient, U_V is the velocity of the vortex wake, and V_v is the volume which can be calculated from the ejected fluid.

$$\mathbf{F}_L = -\rho \frac{d}{dt} \left[\left(\mathbf{I} + \mathbf{C}_{\mathsf{AM}} \right) \mathbf{U}_{\mathbf{V}}(t) V_V(t) \right] \tag{2.13}$$

Modelling Assumptions and Limitations

To create a numerical model for which the structure and fluid dynamics can be solved, several assumptions and simplifications have to be made, both in kinematic and hydrodynamic modelling. This limits the accuracy and reliability of the results. Dabiri and Gharib (2003) assessed the influence of kinematic approximations on the accuracy of swimming dynamics in jellyfish modelling. It states that the approximation of the aperture area is significantly less influential than the approximation of the bell volume. It also states that the hemi-ellipsoid assumption is only valid in the relaxed state. Dabiri et al. (2006) found that a constant velar aperture would result in significant backwards motion of the animal during the refilling phase, and is therefore not a valid assumption.

A key limitation in studies such as Bajcar et al. (2009) is the implementation of prescribed motion, which prevents the model from capturing structural feedback resulting from fluid forces. Passive elements such as tentacles and oral arms are omitted in most models to avoid their negative influence on vortex generation (Feitl et al., 2009; Miles & Battista, 2019). Two-dimensionality is a limitation of models such as Baldwin and Battista (2021), Miles and Battista (2019), and Wilson and Eldredge (2011). Herschlag and Miller (2011) stated that vortex dynamics differ between a 2D model and the organism (for oblate jellyfish).

Bajcar et al. (2009), Hoover et al. (2017), Miles and Battista (2019), and Park et al. (2014) all assumed an incompressible, viscous flow of a Newtonian fluid. Bajcar et al. (2009) also assumed a laminar flow so that no averaging or filtering of the Navier-Stokes equations is required. Herschlag and Miller (2011) stated that the IB method by Peskin (2002) is limited in resolving the shedding of vortex structures for Re$>$1000. Alternative methods that better handle sharp boundaries at higher Re would be valuable for exploring larger-scale dynamics. Sahin et al. (2009) assumed swirl-free axisymmetric Navier-Stokes equations. Dabiri et al. (2006) do not include resistive fluid dynamic forces in their model, as the required measurements of the oral cavity and velar kinematics could not be obtained from a view that contained the full exumbrellar surface. The outer surface profile is necessary to estimate both viscous drag and the acceleration reaction (added mass) of the animal body. An assumption that has been experimentally supported is that vortex ring formation does not affect the refilling phase in hydromedusae; therefore, the refilling flow may be treated as a uniform inflow (Dabiri et al., 2006; Daniel, 1983).

2.2.2. Model Validation

Multiple studies validate their numerical jellyfish model using experimental data of shape, kinematics and hydrodynamics. This data is often extracted from video analysis, direct mechanical testing or flow visualisation techniques. The data serves as benchmarks for assessing the accuracy of model geometry, input motion, and fluid response.

Bajcar et al. (2009) applied image processing techniques on video recordings to capture the bell contour and movements of scyphomedusae. The authors analysed the velocities of selected points along the bell contour and presented these results. Similarly, Dabiri and Gharib (2003) developed a pixel-based search algorithm to reconstruct scyphomedusan shape and motion from video frames. Gemmell et al. (2013) used video recordings of scyphomedusae to determine swimming kinematics. McHenry and Jed (2003) measured bell diameter, height, margin angle, and swimming speed from recordings of live jellyfish. Park et al. (2014) used these data to validate a 3D numerical model. In addition, Park et al. (2014) selected material parameters such as tension and bending moduli, based on the mechanical measurements reported by Demont and Gosline (1988) and Megill et al. (2005). Demont and Gosline (1988) presented static mechanical properties of the bell structure of hydromedusae through non-destructive testing of the mesoglea. Megill et al. (2005) applied experimental sample testing to gather mesoglean fibre properties of a hydromedusan jellyfish.

Hydrodynamic validation involves comparing vortex patterns and swimming forces/velocities. Gemmell, Troolin, et al. (2015) used 3D particle image velocimetry to visualise 'footprints' of the organism, enabling wake dynamics to be captured in high spatio-temporal resolution. It states that 2D particle image velocimetry has the problem that thrust and drag cannot be separated, while the body experiences both thrust and drag. Separation would require a 3D visualisation. So one can see flow accelerations around the bell, but it cannot be said how much is thrust and how much is drag. Flow visualisation data from Dabiri et al. (2005) and Dabiri et al. (2006) provided detailed field and lab measurements of scypho- and hydromedusae. These include dye visualisations of vortex ring structures, bell shape evolution, and flow separation. Wilson and Eldredge (2011) used this experimental data to recreate kinematics to simulate and compare vortex formation and thrust in a bioinspired model. Alben et al. (2013) used the experimental data of Dabiri et al. (2006) (bell diameter) to compare the simulation results of its vortex-sheet model. Additionally, they compared the results with other numerical simulation results, using the immersed boundary method. Park et al. (2014) validated the bell fineness ratio and velocity with experimental data presented by Colin and Costello (2002). This validation is given in Figure 2.6. Colin and Costello (2002) used video recordings of several hydromedusae to determine morphological and kinematic parameters. The study also presents hydrodynamic data in the form of particle velocities relative to the bell.

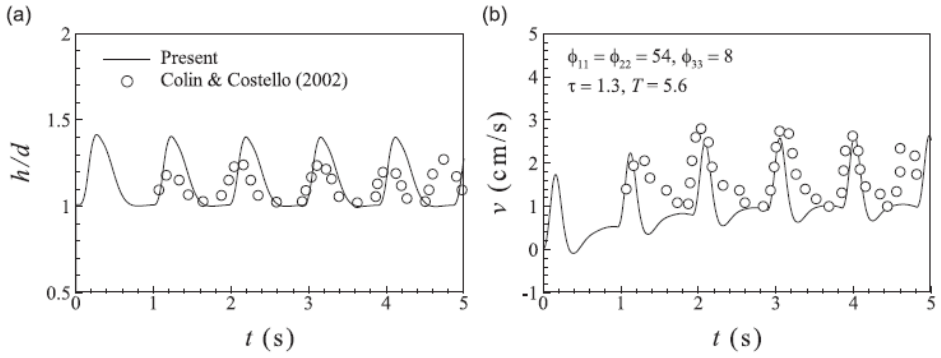

Figure 2.6: Time histories of (a) the fineness ratio and (b) velocity, as determined by simulation in Park et al. (2015) or measured experimentally and reported by Colin and Costello (2002)

Hoover et al. (2017) validated their numerical model against biological measurements of a scyphomedusa and a hydromedusa, using data from Demont and Gosline (1988) and Gemmell et al. (2013). The latter provided quantitative data on swimming speed, distance travelled, circulation, bell diameter, and axial forces. Likewise, Baldwin and Battista (2021) compiled a dataset of jellyfish species, reporting parameters such as bell diameter, fineness ratio, frequency, Reynolds number, and duty cycle, alongside

numerical simulation outputs including vorticity maps and swimming velocities.

Other studies, such as Gemmell, Dabiri, et al. (2021) and Gemmell et al. (2018), provided vorticity and velocity field data across jellyfish types, useful for validating hydrodynamic results. Gemmell et al. (2013) quantified fluid motions through 2D digital particle image velocimetry and conducted a sensitivity study of mesh and time step refinement. Sahin and Mohseni (2009) validated their numerical model for the steady and oscillatory flow around a sphere in a cylindrical tube, as experimental data of the specific jellyfish type considered was missing. They validated their wake structures with the dye visualisation results of Dabiri et al. (2005, 2006), showing consistency. Swimming kinematics were validated with data from Colin and Costello (1996) and Colin and Costello (2002). Finally, Herschlag and Miller (2011) cautioned that while flow profiles and swimming speeds in 2D numerical models agree well with experimental data for prolate bells, such models fail to capture the dynamics of oblate geometries. This is attributed to the likely discrepancies between a 2D model and the 3D reality, as well as an idealised motion. This highlights the importance of selecting appropriate validation targets that match the dimensionality and morphology of the numerical model.

Generally, research is validated through experimental results or field data of specific jellyfish types. Data is available for various jellyfish types, both prolate and oblate. Papers often present validation visually with a graph of the assessed parameter. Validation data for shape, kinematics and hydrodynamics is available, making biological-accurate modelling a viable option. To validate the kinematic model in this research, the data given in Sahin et al. (2009) can be used. This data is presented in Figure 2.5, showing the contraction and expansion phase kinematics for both a prolate and oblate jellyfish type. In this report, results are shown regarding the vorticity fields, velocity components and force coefficients, which can be used to validate the results from the numerical jellyfish model. However, the aim is to validate the jellyfish model with experimental data, presented in Figure 2.6 and given in Colin and Costello (2002).

2.3. Control Problem of the Numerical Jellyfish Model

In the preceding sections, the control problem of the jellyfish bell margin was discussed. It is questioned whether jellyfish control the bell margin actively or passively. It is also questioned which control mode would result in the most efficient propulsion (Wilson & Eldredge, 2011). Passive control is computationally more intensive, as the problem requires FSI solvers. With active control, solid motions can be directly assigned to the fluid motion equations. Considering that bell margin motion may involve (semi-) passive behaviour, it may be hard to employ active control in a biologically accurate way. Exploring the field of flow control and its currently used applications can be beneficial for designing a representative numerical model that controls the flow.

2.3.1. Flow Control Options

Passive Flow Control, as described by Joshi and Gujarathi (2016), involves no external energy input, and active flow control (AFC) requires energy and involves a control system. An example of a passive method is the Gurney FLAP, which is perpendicular to the fluid flow direction, resulting in the formation of two counter-rotating vortices that help delay flow separation, therefore reducing drag. Passive techniques modify the base flow, making it more stable, suppressing and delaying disturbance/instability growth mechanisms. Dobrinsky and Collis (2000) stated that typically, the more stable a flow, the more receptive it is to disturbances. Active flow can target small disturbances directly. Collis et al. (2004) added that the ability of a passive device to control unsteady motions is limited, due to instabilities and turbulence.

All passive controls are effectively open-loop. In open-loop control, either steady (passive) or unsteady (active) actuator parameters are set at the design stage and remain fixed. Closed-loop control requires a controller that can withstand unexpected environmental disturbances or uncertainties in the models used to design the controller. The disturbances in flow systems, accompanied by the approximations made to predict fluid flows, make accurate control design difficult (Collis et al., 2004).

Active Flow Control is described by Collis et al. (2004) as a method of altering a natural flow state or development path into a more desired state (or path). Joshi and Gujarathi (2016) classified AFC into two categories: open- and closed-loop. Open-loop methods involve the introduction of steady or unsteady energy inputs without considering the state of the flow field. Closed-loop methods continuously adjust

the input to actuators based on sensors. Open-loop is generally used in computational and experimental studies, while closed-loop is less commonly used, due to its complexity. Open-loop systems use a predefined actuator input that does not adapt to the flow state. Closed-loop systems use sensors and a control algorithm to adapt actuator input in real time (Collis et al., 2004).

Every active flow control problem starts with a linear or non-linear dynamical system. Generally, linear systems are an idealisation of non-linear real-world systems, especially in terms of fluid systems. In practice, linear control is often successfully applied to non-linear problems (Collis et al., 2004). Collis et al. (2004) stated that optimal control can be used to construct local-optimal open-loop control distributions for the full non-linear equations of motion. Optimal control, however, requires a full mathematical model of the system. To acquire such a model, 'simplifications' are required to make the state equations solvable. Reduced-order models that capture the essential physics of the flow while reducing the expense associated with solving the model offer a solution.

2.3.2. Applications of Flow Control

Joshi and Gujarathi (2016) provided applications of active flow control, including optimising flow field distribution, increasing lift, and reducing drag. Considering the previously discussed jellyfish models, an example of active flow control is the application of a prescribed bell motion (Bajcar et al., 2009). The kinematics are prescribed through 6th-order polynomials with coefficients updated at each simulation time step. Similarly, Alben et al. (2013) used prescribed parametric equations in the form of power-law functions of time, and Herschlag and Miller (2011) prescribed contraction and expansion kinematics by describing the force that the boundary applies to the fluid.

Across the jellyfish models, claims regarding non-linear vortex interactions (vortex (rings) generation and shedding) (Gemmell, Dabiri, et al., 2021), time-dependent parameterisations and contraction cycles (Alben et al., 2013; Hoover et al., 2019; Park et al., 2014) characterise an unsteady non-linear system. The applicable fluid state equations to the assessed jellyfish problems are the unsteady Navier-Stokes equations (Park et al., 2014). These are non-linear partial differential equations. In several discussed papers, physical reduced-order modelling is applied, accomplished by neglecting certain physical processes that can potentially occur; these are the assumptions described in subsection 2.2.2. Collis et al. (2004) presented another example of ROM, data fitting, which is also used in previously discussed papers. Jellyfish shape and kinematics were fitted to data available from experimental research (Alben et al., 2013; Bajcar et al., 2009; Herschlag & Miller, 2011; Sahin et al., 2009). Collis et al. (2001) presented an example of numerically solving optimal control problems governed by the compressible Navier-Stokes equations. In this study, the control mechanism is suction and blowing in the wall normal direction, and it is applied as a function in the boundary condition equations.

Deep reinforcement learning (DRL) can offer a solution to the flow control problem and as a shape optimisation option. DRL has previously been used for high-level control of large systems, such as the swimming of a school of fish (Wang et al., 2023), and for detailed active flow control at the small scale of flow instabilities and separation (Rabault et al., 2020). It is stated that reinforcement learning is significantly more applicable to closed-loop flow control systems. Mecanna et al. (2025) researched the performance of various DRL algorithms in fluid dynamics problems and showed that Proximal Policy Optimisation has established dominance over other algorithms across a wide range of benchmarks. Rabault et al. (2019) studied a circular cylinder with $Re = 100$, in the laminar flow regime, which is later compared to a case with $Re = 1000$, in the low-turbulence flow regime in Ren et al. (2021). For the first case, successful implementation of DRL was already achieved, whereas for the last case, it was newly achieved in Ren et al. (2021). As this is the order of magnitude of the Reynolds number characteristic of the jellyfish case, the application of DRL may be possible for shape optimisation or active flow control. The application possibilities of reinforcement learning are assessed for the jellyfish control problem, but implications will not be an objective in this research.

2.3.3. Efficiency Definitions for a Swimming Jellyfish

Quantifying the swimming efficiency of jellyfish is difficult as a result of unsteady behaviour, entanglement of thrust and drag, the large range of bell shapes and sizes (Gemmell, Dabiri, et al., 2021). Entanglement of thrust and drag results from the same propulsive surfaces contributing to either thrust or drag, depending on the phase of the swimming stroke. As a result, various definitions of performance met-

rics have been proposed across the literature. Generally, efficiency is described through the swimming velocity and cost of transport (COT).

$$\text{COT} = \frac{\text{Energy}}{\text{Mass} \times \text{Velocity}_{avg}} \tag{2.14}$$

Gemmell et al. (2013) used COT as the performance metric for efficiency, defined as a function of energy, mass and average velocity in Equation 2.14. Gemmell, Dabiri, et al. (2021) stated that this COT reflects energy consumption for its locomotion. However, because this measure has dimensional units, it may not scale isometrically and thus is of more limited utility in comparing across ontogeny or in animals with significantly different sizes or physiology. The observation that one animal group has a lower COT than another might be attributable to differences in their hydrodynamics, physiology, relative size or all three.

In Baldwin and Battista (2021), the performance metrics used are dimensionless. It uses a power-based COT and a swimming speed represented by the inverse Strouhal number, respectively defined as in Equation 2.15 and 2.16. The Strouhal number consists of V_{dim} f and D, respectively the dimensional swimming speed, bell actuation frequency and the maximum diameter during an actuation cycle. In the COT, F_j and U_{rj} were the bell's applied contraction force and contraction velocity at the j^{th} time step, and V_{dim} was the temporally-averaged dimensional forward swimming speed during the N time points considered. The term $\frac{1}{\rho f^2 D^3}$ non-dimensionalises the data, providing a COT metric normalised by the bell's driving frequency and size, and the fluid density. According to Gemmell, Dabiri, et al. (2021), a dimensionless COT is a suitable metric for interspecific comparisons of swimming efficiency. Hoover et al. (2019) also used COT and the Strouhal number to quantify the swimming efficiency of jellyfish.

$$\text{COT} = \frac{1}{N} \cdot \frac{1}{\rho f^2 D^3} \cdot \frac{1}{V_{\text{dim}}} \sum_{j=1}^{N} |F_j||U_j| \tag{2.15}$$

$$St = \frac{fD}{V_{\text{dim}}} \tag{2.16}$$

Park et al. (2014) stated that the Froude efficiency is widely adopted as an efficiency metric. It is defined by Wilson and Eldredge (2011) as in Equation 2.17, the ratio between thrust multiplied by velocity and the input power. However, Gemmell et al. (2013) and Sahin et al. (2009) stated that this quantification overlooks passive energy recapture phenomena and ignores viscous effects, as the relaxation phase is not included in this protocol.

$$\eta_{Froude} = \frac{TU}{P_{in}} \tag{2.17}$$

Sahin et al. (2009) stated a power coefficient as a quantification for swimming performance, as given in Equation 2.18. This is a non-dimensionalisation of the power required by the hydromedusae assessed in this paper. It is non-dimensionalised by dividing it by the fluid density, average jellyfish velocity and the maximum bell diameter.

$$C_p = \frac{2P}{\rho U^3 \pi (\frac{D}{2})^2} \tag{2.18}$$

2.4. Research on Sarsia tubulosa

A set of literature was gathered regarding the type of jellyfish that will be modelled in this research. A few papers describe the behaviour of the *Sarsia tubulosa*. Firstly, Lipinski and Mohseni (2009), Sahin and Mohseni (2009), and Sahin et al. (2009) describe the construction and implementation of an axisymmetric approach of this type of jellyfish and evaluate its general swimming behaviour. Sahin et al. (2009) evaluates jellyfish propulsion based on its velocity, Froude efficiency and vortex formation, whereas Lipinski and Mohseni (2009) focuses mainly on the influence of the velum on vortex formation and trailing

jet. Experimentally derived velocities, accelerations and positions of several jellyfish types, including *Sarsia Tubulosa*, are presented in Colin and Costello (2002). Baldwin and Battista (2021) uses a 2D numerical model to explore how adjusting the jellyfish's duty cycle influences its propulsive efficiency, measured in terms of cost of transport and velocity. This paper uses the *Sarsia tubulosa* species more as a guideline for setting up its model. The actual model used in the numerical simulations regards a jellyfish of 1 [m] that behaves in between the prolate and oblate jellyfish range.

An analytical method to model *Sarsia tubulosa* was constructed by Daniel (1983) and implemented in Colin and Costello (1996), Colin and Costello (2002), and McHenry and Jed (2003). These studies apply the hemi-ellipsoid shape assumption and describe analytical methods to compute force contributions such as thrust, drag and added mass. These methods can be used to verify the order of magnitude of the results in this report. Baldwin and Battista (2021) and Daniel (1983) also introduce methods to compute efficiency metrics such as cost of transport and Froude efficiency for *Sarsia tubulosa*.

The determined duty cycle of *Sarsia tubulosa* tends to differ in the literature. Sahin et al. (2009) applies a duty cycle of 0.4. Peng and Alben (2012) found that *Sarsia tubulosa* shows optimal performance for a duty cycle of 0.5, compared to a value ranging between $0.1 < \gamma < 0.2$ found by Baldwin and Battista (2021) and Colin and Costello (2002). Baldwin and Battista (2021) finds a duty cycle most fit for optimising the propulsive efficiency, to be $0.4 < \gamma < 0.5$. This range of duty cycles shows improvement possibilities when applying different duty cycles in successive cycles. A recommendation is made that future work should vary the motion cycle period in successive cycles and investigate the influence of gliding time. Gliding time is the additional period between cycles during which the jellyfish remains stationary. Its kinematics are paused for a moment before the next cycle begins. Comparing these recommendations to the experimental data presented in Colin and Costello (2002), which showed that the duty cycle and motion period may vary per motion cycle, forms a good foundation for a study on duty cycle and period variation. It raises the question of whether it is an application to improve locomotive efficiency.

3

Methodology

This chapter gives an overview of the methodologies applied in this study. The methods and software used to design the model are addressed, and the validation and benchmarking approaches are discussed. The first section clarifies the CFD software WaterLily. The second section presents the applied methods used to generate a biologically accurate jellyfish shape and motion, suitable for CFD simulations. The third section describes the methods and assumptions used to construct the jellyfish geometry. The fourth section discusses the applied simulation framework and the implementation of motion equations to compute the velocity of the numerical jellyfish model. Model and simulation simplifications are validated against non-simplified cases to evaluate their effects. The final section describes the methodology of the kinematic variation study and the computation of propulsive metrics. The numerical model and all supporting analysis scripts used in this study are publicly available in an open-source repository. The full implementation, including simulation scripts and post-processing routines, can be accessed at https://github.com/evanvanderweide/WaterLily-Sarsia-tubulosa-Jellyfish-Modelling.

3.1. The CFD Solver WaterLily

WaterLily is an open-source CFD solver written in the Julia programming language. The solver is backend-agnostic and can run on both CPUs and GPUs, enabling efficient simulations on a wide range of hardware platforms (Weymouth & Font, 2025). WaterLily is designed to simulate unsteady incompressible viscous flows around moving and deforming bodies. The solver computes the incompressible Navier–Stokes equations on a uniform Cartesian grid. The governing equations are given in Equation 3.1 and Equation 3.2, where $\mathbf{u}$ represents the velocity field and p the pressure field.

$$\nabla \cdot \mathbf{u} = 0 \tag{3.1}$$

$$\frac{\partial \mathbf{u}}{\partial t} + \mathbf{u} \cdot \nabla \mathbf{u} = -\nabla p + \nu \nabla^2 \mathbf{u} \tag{3.2}$$

WaterLily applies a finite-volume discretisation on a structured Cartesian mesh with a staggered grid arrangement, in which velocities are stored at cell faces and pressure at cell centres. This formulation improves numerical stability and avoids pressure–velocity decoupling (Weymouth & Font, 2025). Time integration is performed using a fractional-step projection method. An intermediate velocity field is first computed from the momentum equation (Equation 3.2), after which a pressure Poisson equation is solved to enforce the incompressibility constraint (Equation 3.1). The Poisson equation is solved using a geometric multigrid method to accelerate convergence. WaterLily is a non-dimensional CFD solver. All geometric inputs, velocities, and time scales must be appropriately scaled before simulation. The kinematic viscosity of the fluid is adjusted numerically to match the length and velocity scales to the Reynolds number that characterises the flow.

A key feature of WaterLily is its implementation of the Boundary Data Immersion Method (BDIM) (Weymouth & Yue, 2011). Instead of conforming the computational mesh to the body geometry, BDIM embeds

solid bodies within the fixed Cartesian grid. The fluid and solid governing equations are smoothly blended across a thin interface region of thickness ϵ. Within this transition layer, the equations vary from solid-body motion to fluid Navier–Stokes behaviour. The body geometry is defined through a signed distance function (SDF), which is negative inside the solid and positive in the fluid domain. This representation enables the construction of complex, time-dependent geometries without remeshing. By incorporating pressure within the blended formulation, BDIM enforces the correct no-slip and no-penetration boundary conditions at the fluid–solid interface. This approach avoids the numerical complexity associated with body-fitted meshes while maintaining second-order spatial accuracy.

There are several ways to model a body in WaterLily. Depending on the geometry and motion problem, an optimal method can be applied. A WaterLily extension, the ParametricBodies.jl package, is available and can be used to construct parametric bodies within WaterLily (Weymouth, 2025). The extension supports the definition and transformation of embedded bodies in flows. The package includes the functionality to define a body using non-uniform rational B-splines (NURBS), which has previously been used to model *Sarsia tubulosa*, including its velar properties, by Sahin and Mohseni (2009). This geometric definition requires a set of control points in matrix form, a weights array, and a knots array.

The simulation of *Sarsia tubulosa* propulsion requires modelling of the complex deforming bell with prescribed kinematics. Generating a body-fitted mesh for each time step would be computationally expensive and complex. The Cartesian grid, combined with BDIM, avoids remeshing and enables implementation of time-dependent kinematics by updating the signed distance function. The ParametricBodies extension simplifies geometry and motion implementation by providing a geometry definition method and the ability to map it from 2D to 3D. In the present work, time-dependent sets of control points are used to reproduce the bell deformation of *Sarsia tubulosa*. GPU compatibility can accelerate simulations of jellyfish motion in 3D. Finally, the open-source accessibility and online support benefit this study and simplify future research.

3.2. The Numerical Jellyfish Model

The axisymmetrical jellyfish model and methods described in Lipinski and Mohseni (2009), Sahin and Mohseni (2009), and Sahin et al. (2009) served as a reference for constructing this jellyfish shape and kinematics. Sahin et al. (2009) modelled *Sarsia tubulosa* and presented its kinematic profile as in Figure 2.5, which was digitised from recordings of swimming jellyfish. Figure 2.5 presents the kinematic settings at certain time steps in the motion cycle $\{0, 1, 2, 3, 4, 5, 6, 7, 8, 9\}\frac{T}{10}$. Along with these time variations, some characteristic parameters defining the geometry and kinematics of *Sarsia tubulosa* were stated. Table 3.1 shows these characteristic parameters, where Reynolds and Strouhal numbers were computed with the given equations. These characteristic parameters were used to construct the geometry and simulation environment accordingly. These numbers were used to define the length, velocity and time scaling.

Maximum Diameter	D_{max}	1.25	cm
Average Translational Velocity	U_{avg}	2.42	$\frac{cm}{s}$
Motion Cycle Period	T	1.00	s
Reynolds Number	$Re = \frac{U_{avg} D_{max}}{\nu}$	302	$-$
Strouhal Number	$St = \frac{D_{max}}{U_{avg} T}$	0.52	$-$

Table 3.1: Characteristic parameters of the *Sarsia tubulosa* model, reproduced from Sahin et al. (2009)

The kinematic profiles in Figure 2.5 were copied by transforming the curves into separate sets of control points. Each control point moves according to the kinematic profiles over time. The result was a matrix of control points defining the jellyfish shape at each time step in the motion cycle. This set of control points was not smooth in time and space due to discretisation discrepancies. However, WaterLily requires smoothness and continuity in its simulation geometries; therefore, adjustments and optimisations were required. To obtain a functional time-varying bell shape suitable for the WaterLily CFD solver, the following steps were taken:

1. Accurate scaling and discretisation. Since WaterLily is a non-dimensional solver, the input was scaled accordingly. The geometry was discretised into a larger set of control points to improve the

definition of the signed distance function.

2. Enforcing the conservation of mass. In the two-dimensional case, this was achieved by maintaining a constant geometric area. In the three-dimensional case, a constant geometric volume was maintained. Both were enforced with a correction algorithm.
3. Upsampling of control point sets. The control point sets were upsampled to prevent excessive geometric change between time steps.
4. Geometry change continuity. Each control point was constrained to move with a continuous position, velocity and acceleration. A smoothing algorithm was applied.

3.2.1. Rescaling and Discretisation

As described in section 3.1, non-dimensionalisation of the simulation parameters is required to define the simulation appropriately. The maximum bell diameter of 1.25 [cm] was used as the characteristic length. The maximum bell diameter in WaterLily units was defined as a function of the grid size $D = 2^p$. This resulted in the length scale given in Equation 3.3.

$$l^* = L\frac{D}{D_{max}} = \frac{2^p}{1.25}L \tag{3.3}$$

Similarly, the average velocity was used to scale the numerical velocity in WaterLily. It was noted that the average velocity is a post-processing parameter in Sahin et al. (2009) and not the velocity scale used to define their simulation environment. However, in the absence of this scale, the average velocity was applied. By defining the WaterLily velocity scale as $U = 1$, the resulting velocities in WaterLily were on the same velocity scale as Sahin et al. (2009). To transform velocity data into WaterLily units, the scaling in Equation 3.4 was applied.

$$u^* = u\frac{U}{U_{avg}} \tag{3.4}$$

The time scale was defined as the fraction of the characteristic velocity scale and the characteristic length scale. To non-dimensionalise the period given in Sahin et al. (2009), it was multiplied by this time scale, as presented in Equation 3.5. The result is a period in convective time units, which can then be translated to the actual numerical time of the solver by multiplying it by the WaterLily time scale $\frac{2^p}{U}$.

$$t_i = T\frac{U_{avg}}{D_{max}} = \frac{2.42}{1.25}T \tag{3.5}$$

The control points were non-dimensionalised by multiplying the coordinates by the length scale. The rescaled control point sets were assigned to the contraction and expansion phases according to the definition in Sahin et al. (2009). The first four sets represent the contraction phase, and the last six sets the expansion phase. The geometry was discretised into a larger set of control points to reduce the motion per time step by implementing a piecewise-linear arc-length parametrisation. This parametrisation added additional control points without altering geometric properties, such as the velar kinematics.

The initial set consisted of M_{cps} control points, which were increased to N_{cps} while preserving the original control points, thereby retaining the full geometry of the velum. Each segment length l_i between two control points was derived along with the total arc length $L = \sum l_i$. Each segment received $n_i = (N_{cps} - M_{cps})\frac{l_i}{L}$ new points, meaning that longer segments received more points. The algorithm ensured that the initial control points remained by retaining the first control point of each polyline. Additional control points were then added at uniform fractional positions along each segment, parametrised for $s \in (0, 1)$ through Equation 3.6.

$$\mathbf{cp_{new}} = (1 - s)\mathbf{p_0} + s\mathbf{p_1} \tag{3.6}$$

Additionally, the order of the control points was reversed to obtain a WaterLily-appropriate geometry definition. The ordering was required to be counter-clockwise so that the flow was defined outside the geometry rather than inside.

3.2.2. Mass Conservation

To enforce mass conservation, an area- and volume-correction algorithm was applied. In the two-dimensional case, area was conserved; in the three-dimensional case, volume was conserved. Since the simulation assumes incompressible flow with constant density, mass conservation reduces to the preservation of geometric area (2D) or volume (3D). The area or volume of the first control point set was used as the reference value. In the two-dimensional case, the area was computed using the shoelace formula (Gauss's area formula), given in Equation 3.7. This formula, derived from the trapezoidal rule, is suitable for complex polygonal geometries, such as the jellyfish bell.

$$A = \frac{1}{2} \left| x_1 y_2 + x_2 y_3 + \cdots + x_n y_1 - (y_1 x_2 + y_2 x_3 + \cdots + y_n x_1) \right| \tag{3.7}$$

For the three-dimensional case, the volume was computed as the solid of revolution of the instantaneous area about the axis of symmetry. The geometry was defined by linear NURBS between control points. The enclosed volume could therefore be calculated using the method of disks for solids of revolution, enclosed by these linear splines, as given in Equation 3.8.

$$V = \frac{\pi}{3} \sum_{i=1}^{N-1} (x_{i+1} - x_i)(y_i^2 + y_i y_{i+1} + y_{i+1}^2) \tag{3.8}$$

A geometric correction algorithm was then applied to minimise the deviation in area or volume relative to the reference frame. The first frame of the control point set served as the reference geometry. For each subsequent frame, two characteristic quantities were evaluated. A scaling factor defined as in Equation 3.9, where V_0 denotes the reference volume (or area in 2D) and V the instantaneous value. The centroid of the control point set in longitudinal and transversal directions is computed, as defined in Equation 3.10. A new control point set was then generated by scaling the previous control points about the centroid using the factor ϵ_V, as given in Equation 3.11.

$$\epsilon_V = \sqrt{\frac{V_0}{V}} \tag{3.9}$$

$$\mathbf{c} = \frac{1}{N_{cps}} \sum_{n=1}^{N_{cps}} \mathbf{i}_n, \quad \mathbf{i}_n \in (x, y) \tag{3.10}$$

$$\mathbf{cp_{new}} = \mathbf{c} + \epsilon_V (\mathbf{cp_{old}} - \mathbf{c}) \tag{3.11}$$

Equation 3.8 and Equation 3.11 were implemented to enforce mass conservation. Figure 3.1 shows the evolution of the jellyfish geometry volume divided by the initial volume, over 2 motion cycles. The value on the y-axis represents the conservation error, which is the fraction $\frac{V}{V_0}$. This means that the maximum volume error equals 0.0020 [-]. Note that these volumes were computed after application of the smoothing and upsample algorithms and are therefore an appropriate measure for the conservation of volume.

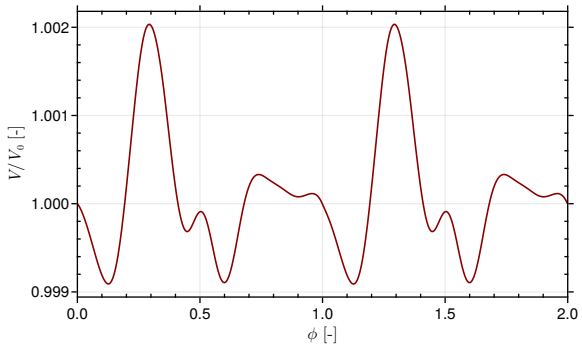

Figure 3.1: The realised enforcement of mass conservation. The fraction between the instantaneous volume V and the reference volume V_0, computed at $t = 0$, over a time range of 2 motion cycles, expressed as the phase ϕ.

3.2.3. Upsample Control Point Sets

The number of control point sets was upsampled to smooth the motion cycle. The number of upsamples was also varied to control the prescribed kinematics, such as the duty cycle, periodic variation and gliding time. The duty cycle is defined as in Equation 3.12 for the present study. It drives the number of upsamples added per motion phase. Additional upsampling frames were added to the contraction or expansion phase, depending on the duty cycle, while the time range remained constant. The additional frames were added by interpolating between the control point positions in the original frames. A third-order spline interpolation was applied to obtain continuous position, velocity, and acceleration between the control points. Each control point was handled individually for translational and radial position. Periodic variation and gliding time were also implemented through frame up-sampling, which will be explained in subsection 3.2.6. The result of this upsampling algorithm is an extensive set of geometry-defining control points for the jellyfish motion cycle.

$$\gamma = \frac{T_{contr}}{T_{contr} + T_{exp}} \tag{3.12}$$

3.2.4. Smoothing of Control Point Paths

An exponential smoothing algorithm was used to acquire the continuous motion of each control point (Oppenheim & Schafer, 2010). An array $\mathbf{x_0}$ and a smoothing parameter $\alpha = 0.25$ (higher α means less smoothing, and smaller values mean greater smoothing) are passed into the function, and the first value is saved. The following values in the array are smoothened using Equation 3.13. In this problem, the input array represents the path of a single control point in one direction. s_{t-1} is substituted into s_t continuously so that the formula of s_t is fully expressed in terms of x_t. s_t is a weighted average of the input array $\mathbf{x_t}$ and the previous smoothed statistic s_{t-1}. Each data point x_t reveals an exponentially decreasing weight on observations further in the past (forward smoothing). Exponential smoothing applies a weighted moving average in which more recent observations carry greater weight. The phase lag resulting from forward smoothing was reduced by adding a backward pass to the forward-smoothened values, as in Equation 3.14. The result is a forward-backwards smoothened control point path, with reduced phase lag compared to one-sided smoothing.

$$s_0(t) = \alpha x(t) + (1-\alpha)s_0(t-1)\ ,\ t > 0 \tag{3.13}$$

$$s_1(t) = \alpha s_0(t) + (1-\alpha)s_1(t+1) \tag{3.14}$$

The resulting control point paths were turned into a function of time by interpolating them over the non-dimensional time range. The time scale was applied by dividing the non-dimensional period of the motion cycle T, multiplied by the number of cycles n_{cycle}, by the number of frames n_{fr}. The result is a set of control point position functions, both for x- and y-coordinates, that are all dependent on the non-dimensional time t_i. These functions were put together into an array to define the full jellyfish geometry at a certain time t. The matrix is given as in Equation 3.15.

$$\mathbf{CP_{set}}(t) = \begin{bmatrix} cp_{1,x}(t) & cp_{2,x}(t) & - - - & cp_{n-1,x}(t) & cp_{n,x}(t) \\ cp_{1,y}(t) & cp_{2,y}(t) & - - - & cp_{n-1,y}(t) & cp_{n,y}(t) \end{bmatrix} \tag{3.15}$$

To create the actual geometry, a non-uniform rational B-spline (NURBS) curve was used to connect the control points. In addition to the control point array, a NURBS curve requires a knots and weights array. As the control points were digitised so that they are located exactly on the jellyfish boundary, the weights array is simply a ones vector of length $2 \times N_{cps}$.

$$\mathbf{W} = \begin{bmatrix} 1 & 1 & - - - & 1 & 1 \\ 1 & 1 & - - - & 1 & 1 \end{bmatrix} \tag{3.16}$$

The knot array was defined as an open uniform B-spline knot vector, combining evenly spaced internal knots with clamped start and end knots. In the present case, a spline degree of $p = 1$ was employed, resulting in a linear piecewise curve that is $C^{p-1} = C^0$-continuous. Consequently, the curve is continuous in position but not in slope, meaning that sharp geometric corners (high curvature areas) may occur at the control points. The complete knot vector $\mathbf{K}$ is given in Equation 3.17 (Peterson, 1990). It consists of $p + 1$ repeated knots at the start and end of the parameter domain, corresponding to the clamped boundaries, and uniformly distributed interior knots. The multiplicity $p + 1$ at the boundaries clamps the first and last control points. The clamped knot configuration ensures that the curve starts at the first control point and ends at the last, instead of approaching them.

$$\mathbf{K} = \left(\underbrace{0, \ldots, 0}_{p+1},\ k_2, \ldots, k_{N_{cps}-1}, \underbrace{1, \ldots, 1}_{p+1} \right) \tag{3.17}$$

The interior knots are defined uniformly over the parameter interval $[0, 1]$, as given in Equation 3.18. This uniform spacing ensures consistent parameterisation along the control polygon. Generally, higher-order splines improve accuracy and reduce the number of control points required. However, for computational reasons, discussed in subsection 3.3.3, this was not applied in this model.

$$k_i = \frac{i - p}{N_{cps} - p}, \qquad i = 2, \ldots, N_{cps} - 1. \tag{3.18}$$

3.2.5. Mapping to 3D

The mapping functionality in WaterLily was used to turn the NURBS curve into a three-dimensional body, fit for the WaterLily CFD simulation (Weymouth, 2025). Using the mapping function in Equation 3.19, the parametric NURBS curve was rotated around an axis of symmetry, and a 3D Parametric Body resulted. This mapping function transforms the curve from the 3D x-space to the 2D ξ-space, which is appropriate for WaterLily simulations. The code block below was applied to generate the knots and weights array, the NURBS curve and the 3D body. A visualisation of the resulting geometry is presented in Figure 3.2. The mapping function in Equation 3.19 was used to generate the quarter geometry, whereas the full 3D geometry requires an offset (D) for x_2 and x_3. This offset is required to avoid the domain boundaries from cutting the geometry.

$$\text{rev\_map}: \ (x_1, x_2, x_3) \mapsto \left(x_1, \sqrt{x_2^2 + x_3^2} \right) \tag{3.19}$$

```
knots_vector(p::Int, Ncp::Int) = vcat(zeros(p+1), (Ncp-p-1 > 0 ? collect(range(0.0, 1.0,
↪  length=Ncp-p+1))[2:end-1] : Float64[]), ones(p+1))

weights          =   ones(T, size(cps, 2))
knots            =   Float64.(knots_vector(deg, size(cps, 2)))
curve            =   NurbsCurve(cps, knots, weights)
rev_map(x,t)     =   SA[(x[1]), hypot(x[2], x[3]) ]
body             =   ParametricBody(curve; map=rev_map, ndims=3)
```

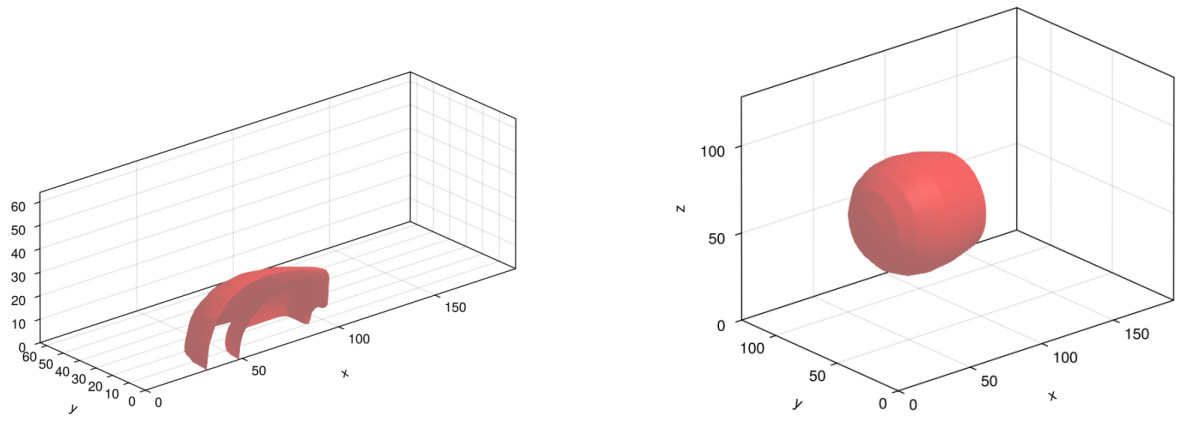

(a) Quarter Geometry.

(b) Full Geometry.

Figure 3.2: The constructed three-dimensional geometries of *Sarsia tubulosa* in the present model. The red area represents the location where the signed distance function equals 0.

3.2.6. Prescribing Kinematics

The jellyfish motion was prescribed through a kinematic control algorithm, in which a sequence of geometry frames is transformed into a continuous, time-dependent motion. The adjustable kinematic parameters $\{\gamma, T_1, T_2, T_g\}$ are introduced by modifying the distribution of these frames, instead of changing the geometry. This approach enables systematic variation of duty cycle, cycle period, and gliding behaviour.

Base frame construction: The initial motion is defined by the set of 10 refined frames from Sahin et al. (2009), consisting of 4 contraction frames and 6 expansion frames, corresponding to a baseline duty cycle of $\gamma = 0.4$. To obtain a smooth representation of the motion, each interval between frames is refined by a third-order interpolation. The number of upsamples between each frame is n_{up}.

Duty cycle modification: The duty cycle γ, defined as the ratio of contraction time to total cycle time, is applied by adjusting the number of contraction upsamples according to

$$n_{contr} = \frac{10\gamma \cdot n_{exp}}{4}, \tag{3.20}$$

where n_{exp} remains equal to n_{up}. Note that, as the initial contraction to expansion setting is not 50-50, the fraction of $\frac{10}{4}$ was required. The contraction and expansion phases now consist of $4n_{contr}$ and $6n_{exp}$ frames, respectively. This is defined on the uniform time range $0 \rightarrow T_1$.

Consecutive period modification: The reference period T_1 defines the base period of the motion cycle. To apply a varying consecutive period, the variable T_2 was introduced. To acquire the correct kinematics for this consecutive cycle, the number of upsampling frames was scaled with T_1:

$$(n_{up})_{T_2} = \frac{T_2 (n_{up})_{T_1}}{T_1}. \tag{3.21}$$

This ensures that both cycles remain kinematically consistent while differing in duration. The combined motion is therefore defined over the interval $0 \rightarrow (T_1 + T_2)$.

Gliding interval: A gliding interval of duration T_g is incorporated by repeating the first frame in Figure 2.5

$$n_{g,fr} = \frac{T_g}{T_1} n_{fr} \tag{3.22}$$

times, where n_{fr} is the number of total (interpolated) frames defining T_1. This generates a period with no deformation between consecutive cycles. The total time array is extended accordingly, to a full cycle duration of $0 \rightarrow (T_1 + T_g)$. This can also be combined with a varying consecutive period, which requires the time array to be $0 \rightarrow (T_1 + T_g + T_2 + T_g)$.

Final control-point representation: The complete sequence of frames is concatenated over multiple cycles and smoothed to ensure continuity of motion. A uniform time vector is then constructed over

the full duration, and the interpolated control-point trajectories are evaluated to obtain the matrix of interpolation functions $\mathbf{CP}_{\text{set}}(t)$, as defined in Equation 3.15.

This formulation enables independent and combined variation of duty cycle, consecutive cycle periods and gliding intervals, while maintaining a consistent geometric description of the jellyfish motion. The full code is available in the reproducibility repository [1].

This algorithm was validated for five cases in which the instantaneous volume enclosed by the bell and velum, referred to as the oral cavity volume, was observed. For each case, a different kinematic setting was varied, with the initial period fixed at $T_1 = 1$. The first case represents the baseline simulation with a duty cycle of $\gamma = 0.4$. In the second case, the duty cycle was set to $\gamma = 0.2$. For the third and fourth cases, kinematics were modified for a shorter period $T_2 = 0.5$ and a gliding interval $T_g = 0.5$, respectively. In the final case, the variations in T_2 and T_g were combined. Figure 3.3 presents the resulting volumes over the phase normalised by the first period T_1. The cases with the same duty cycles exhibit similar behaviour during the first period, whereas the duty cycle variation of $\gamma = 0.2$ is observed. During the second period, kinematic variations are visible. The case with a gliding interval of $T_g = 0.5$ shows a constant volume for $1 < \phi < 1.5$. The T_2 variation is also visible in this range, as indicated by the dashed brown line. Case 5 is the combined case, including gliding time and periodic variation, which is visible in the range of $1 < \phi < 2$, where the first half is the gliding interval and the second half is a short T_2 period. These results confirm that the implemented kinematic algorithm correctly reproduces the prescribed variations in periodic variation and gliding phases.

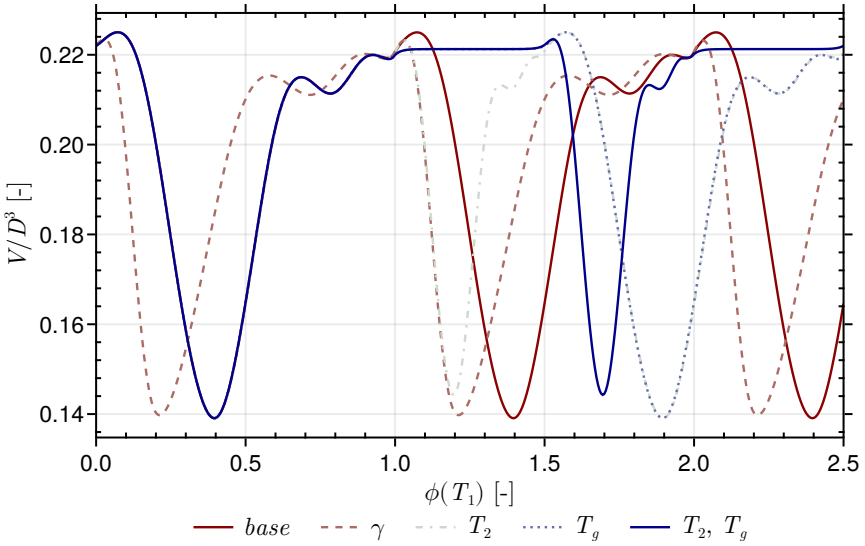

Figure 3.3: Evolution of the non-dimensionalised oral cavity volume for five kinematic configurations with a base case $T_1 = 1\,[s], \gamma = 0.4$, $\gamma = 0.2$ variation, $T_2 = 0.5\,[s], \gamma = 0.4$ variation, $T_g = 0.5\,[s], \gamma = 0.4$, variation and combined $T_2 = 0.5\,[s], T_g = 0.5\,[s], \gamma = 0.4$ variation.

3.3. Simulation Framework

To construct the simulation framework, considerations regarding computational efficiency and physical accuracy were required. To avoid full fluid-structure interaction modelling, simplified force equations were applied. The simulation setup uses a stationary quarter of the jellyfish shape to reduce computational time, combined with a moving grid. The governing equations, simulation settings, assumptions and restrictions of the framework are discussed and validated in the following sections.

3.3.1. Governing Equations

Navier-Stokes Equations with a Moving Grid

An actual forward-moving jellyfish would require a large computational domain as it can move multiple body lengths per stroke (Baldwin & Battista, 2021). A moving grid was used to address this problem,

[1] See reproducibility repository: Kinematic control algorithm

as the domain remains small around the jellyfish and thus does not translate. Instead, the grid motion opposes the direction in which the jellyfish would move to replicate the actual physical situation with a non-moving jellyfish. The jellyfish velocity and acceleration, computed from the hydrodynamic force through the equations of motion, are applied to the moving grid. The WaterLily time-step updater was adjusted as shown in the code below, passing the kinematics (acceleration a_0 and velocity v_0) to the fluid solver. The velocity is passed to the solver as the new far-field boundary and used for the velocity boundary condition in the next time step. A fluid moving with velocity v_0 past the stationary jellyfish, in the opposite direction of its swimming motion, results. The acceleration is also required input, as it is used to update the flow solver equation by adding this acceleration on the right-hand side, as given in Equation 3.23. This model solves the Navier-Stokes equations in a frame translating with velocity v_0 and acceleration a_0.

```
biot_mom_step(sim.flow,sim.pois,sim. ,sim.x ,sim.tar,sim.ftar;
fmm=sim.fmm,udf=fall!,acceleration=SA[-a0,0.f0],U=SA[-v0,0.0])
```

$$\frac{\partial \mathbf{u}}{\partial t} + (\mathbf{u} \cdot \nabla)\mathbf{u} = -\nabla p + \nabla^2 \mathbf{u} - \mathbf{a}_{\text{frame}} \tag{3.23}$$

The force and velocity of a simulation with a non-moving grid and a moving grid were compared in Figure 3.4a and Figure 3.4b, respectively. This shows that the case with a non-moving grid continuously accelerates, whereas the case with a moving grid reaches a steady-state. Unfortunately, translation using a mapping function was not achieved because it induced large control-point displacements per time step. For this reason, no comparison to an actual forward-moving jellyfish was conducted. The moving grid is therefore the only viable option for the present model to acquire a translating jellyfish case. With a fully moving background grid, differences from the actual flow occur, as all fluid moves away from the jellyfish with the same velocity. In the actual problem, this is constrained to the jet emitted from the oral cavity.

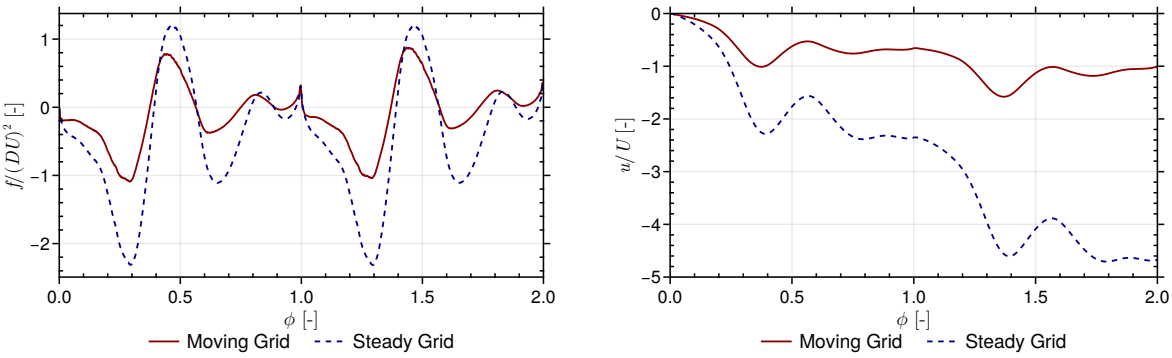

(a) Instantaneous force

(b) Instantaneous velocity

Figure 3.4: The instantaneous force and velocity over 2 motion cycles for a case where the velocity is applied to the moving grid, and one where the grid does not move. The jellyfish does not translate in both cases. For the steady grid, there is only motion of the jellyfish in place.

Equations of Motion for a Rigid Body

The equations of motion for a rigid body were used to model the swimming jellyfish (Weymouth & Font, 2025). The instantaneous hydrodynamic force that the fluid exerts on the jellyfish body is computed as the sum of the pressure and viscous force on the body, as in Equation 3.26. Pressure force is computed as the integral of all local pressures on the body, and the viscous force is computed as the integral of the local rate of strain tensors on the body. Only the x-component is used for the translational motion of the jellyfish. The acceleration is computed by dividing this force F_x by the jellyfish volume (Equation 3.28). The acceleration is then used to calculate the position and velocity.

$$\mathbf{F}_p(t) = \int_{\partial\mathcal{B}(t)} p(\mathbf{x},t)\,\mathbf{n}(\mathbf{x},t)\,\mathrm{d}S, \tag{3.24}$$

$$\mathbf{F}_\nu(t) = \int_{\partial\mathcal{B}(t)} \boldsymbol{\tau}(\mathbf{x},t)\,\mathbf{n}(\mathbf{x},t)\,\mathrm{d}S \tag{3.25}$$

$$\mathbf{F}_{\text{tot}}(t) = \mathbf{F}_p(t) + \mathbf{F}_\nu(t), \tag{3.26}$$

The corresponding acceleration is computed by dividing this force component, F_x, by the jellyfish volume, according to Equation 3.28. Added mass was modelled implicitly by dividing the translational force by an added mass coefficient α times the volume V, in addition to the actual volume. Hence the $(1+\alpha)V$-term in Equation 3.28. The added mass coefficient was derived similarly to Daniel (1983), who assumed that the jellyfish shape is similar to a hemisphere. In the present model, however, added mass was implemented by assuming that the fluid in the cavity translates with the jellyfish. The resulting coefficient, given in Equation 3.27, varied between 0.4 and 0.6 with V_{cav} being the oral cavity volume and V_{body} the geometry volume. Given the general uncertainty surrounding this coefficient, a sensitivity study was conducted and is discussed in subsection 4.8.1. The computed acceleration is subsequently used to update the velocity and position of the jellyfish in time through Equation 3.29 and Equation 3.30, respectively. To ensure compatibility with Sahin et al. (2009), the acceleration computation was adjusted to the version given in

$$\alpha_{am} = \frac{V_{cav}}{V_{cav} + V_{body}} \tag{3.27}$$

$$a_x(t) = \frac{F_x + \alpha_{am} V a_{x,t-1}}{(1+\alpha_{am})V} \tag{3.28}$$

$$u_x = \int a_x dt \tag{3.29}$$

$$p_x = \int (u_0 + \frac{\Delta t a_x}{2}) dt \tag{3.30}$$

Force Filtering

Due to the geometry setup in this simulation, where control points move freely to maintain mass conservation and continuity, the resulting hydrodynamic force was noisy. This is especially true for two-dimensional simulations, which are more constrained as there is one dimension less to compensate for noise. A filter was applied to the CFD force to obtain a smoother signal, suitable for computing acceleration and velocity. An exponential smoothing filter was applied, using a fraction of the motion cycle period for smoothing. This algorithm was already introduced in Equation 3.13. The smoothing factor for this force is given in Equation 3.31, where the time step is used as a fraction of the period to define the factor. This filter induces a phase lag.

$$\alpha = 1 - e^{\frac{-\Delta t}{0.03\frac{TD}{U}}} \tag{3.31}$$

To show the influence of this force filtering, the directly computed force from a 3D simulation is presented against the filtered force in Figure 3.5. It shows the instantaneous force signal over 2 motion cycles. The introduced phase lag $\Delta\phi = 0.045$ is shown as the coloured bar. The difference between filtered and non-filtered force shows the necessity of this construction to acquire reasonable dynamics.

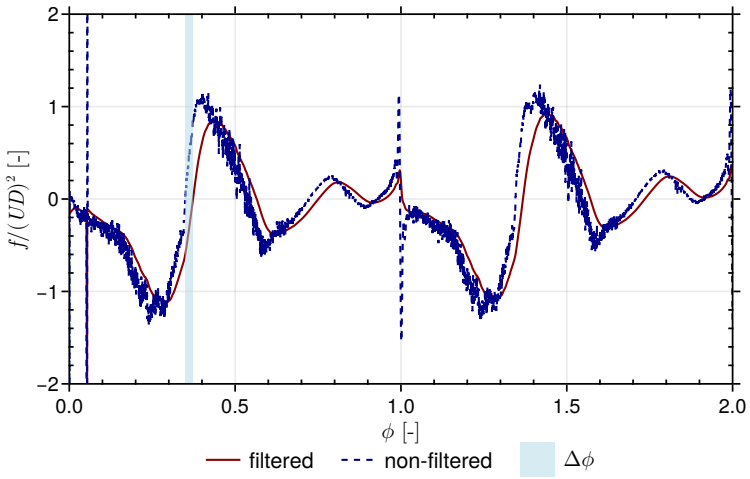

Figure 3.5: The non-dimensional filtered and non-filtered hydrodynamic force signals over 2 motion cycles. A smoothing coefficient of $\alpha = 1 - e^{\frac{-\Delta t}{0.03\frac{TD}{U}}}$ was implemented for the smoothed signal.

3.3.2. Domain Size and Boundary Conditions

The simulation framework in WaterLily was defined by a set of parameters: domain, characteristic parameter values, time-dependent geometry, boundary conditions, governing equations, and interactive grid updating. The simulation framework was defined as in the code block below. The input parameter that defines geometry and domain size and length scaling is the grid size / characteristic length $D = 2^p$. As discussed in section 3.2, the maximum jellyfish diameter equals 2^p grid cells. The domain size is a multiple of the characteristic length and was determined and justified with a convergence study in subsection 4.1.2. The domain length is three times larger in the translational direction than in the radial directions, as the flow develops mostly in the translational direction. The resulting domain size $(3D, D, D)$ is small, given that the quarter jellyfish geometry has a radial length of $\frac{D}{2}$ and the vortices develop beyond the translational length of $3D$. Applying this small domain size was viable for using the Biot-Savart boundary conditions (Weymouth & Lauber, 2024). The actual simulation was generated in the BiotSimulation command, which implements the Biot-Savart boundary conditions.

```
Domain      =   (3D, D, D)
Uff         =   (0,0,0)
sim         =   BiotSimulation(Domain, Uff, D; U,  =U*D/Re, body, T, mem=Array,  )
```

The Biot-Savart boundary conditions as documented by Weymouth and Lauber (2024) were implemented. The equation, given in Equation 3.32, updates the velocity on the domain boundaries with the vorticity inside the domain. In the equation, ω is the vorticity strength and $\mathbf{r}$ is the distance between the vortex and the velocity at location $\mathbf{x}$. The equation originates from an analogy between the vortex axis and the electric current in magnetism. It assumes that the velocity field around a vortex axis behaves similarly to a magnetic field around a current-carrying wire. The Biot-Savart boundary conditions were applied to the non-symmetrical planes of the domain.

$$\mathbf{u}(\mathbf{x}) = \mathbf{U}_\infty + \int_\Omega K(\mathbf{r}) \times \omega(\mathbf{y}) d\mathbf{y} \tag{3.32}$$

$$K(\mathbf{r}) = -\frac{\mathbf{r}}{4\pi|\mathbf{r}|^3} \tag{3.33}$$

As the jellyfish starts moving from rest, the initial flow conditions U_{ff} were set to 0 for each direction. This means that the simulation starts with a stationary background flow, which is updated with the computed jellyfish acceleration and velocity in subsequent time steps. The grid resolution $D = 2^p$ was defined with the convergence study in subsection 4.1.1. The kernel width was set to $\epsilon = 2$, which is addressed in subsection 3.3.3.

A symmetry boundary condition was applied to the 'cut-off boundaries' of the body to reduce computational costs. With these symmetry planes, only a quarter or half of *Sarsia tubulosa* needs to be simulated for the 3D and 2D cases, respectively. The symmetry around the x-axis implies that a symmetry condition should be applied on the $y = 0$ boundary as in Figure 3.2. This condition should also be applied on the $z = 0$ boundary. The symmetry condition replaced the BiotSavart boundary condition on these symmetry planes. The code block below states how the symmetry boundary condition can be applied in WaterLily simulations. This condition enforces no flow/vortices through the boundaries, and the normal velocity at the boundary equals zero. In this code block, T_i and sgn_i represent reflections of the vortex across the boundary. The combined T_{12} ensures that the boundary is also enforced where $y = z = 0$. To validate the accuracy of this symmetry condition, simulation frameworks with a full modelled geometry and with the symmetry assumptions were compared. Figure 3.6a presents the forces on a half 2D jellyfish with symmetry boundary conditions compared to those on a full 2D jellyfish, Figure 3.6b does so for 3D. Figure 3.6 confirms the accuracy of this method for 2D and 3D. It should be noted that certain vortex dynamics may be missing when applying the symmetry conditions. Implementing symmetry boundary conditions halved the domain size in 2D and quartered it in 3D, thereby reducing computational costs.

```
import BiotSavartBCs: interaction,image,symmetry
@inline function symmetry( ,T,args...)
    T ,sgn  = image(T,size( ),-2)
    T ,sgn  = image(T,size( ),-3)
    T ,_    = image(T ,size( ),-3)
    return interaction( ,T,args...)+sgn *interaction( ,T ,args...)+
        sgn *(interaction( ,T ,args...)+sgn *interaction( ,T  ,args...))
end
```

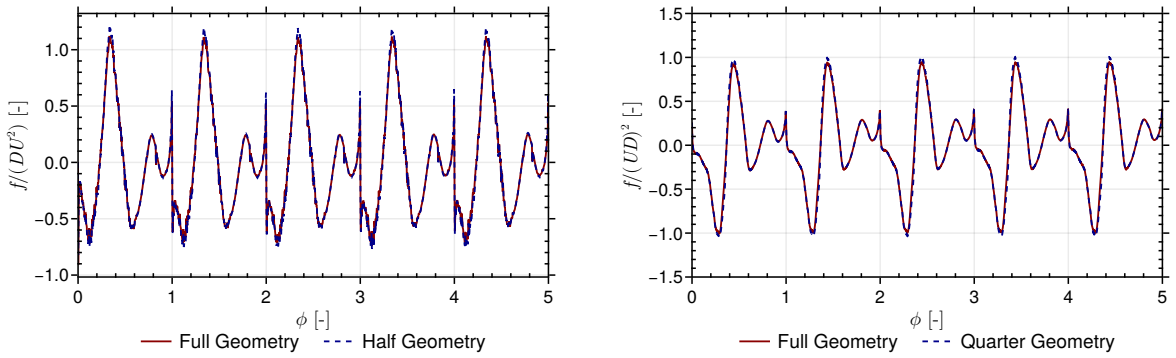

(a) Two-dimensional

(b) Three-dimensional

Figure 3.6: Comparison of non-dimensional forces between a full jellyfish model and a half/quarter geometry with a symmetry boundary condition replacing the other half/quarter. Comparisons are given for both the two-dimensional and three-dimensional cases.

The scale of the simulation is defined by the characteristic velocity U, Reynolds number Re, and numerical viscosity ν. As stated, the length scale is defined by $D = 2^p$ according to Equation 3.3. The characteristic velocity is set to $U = 1$, meaning that 1 velocity unit in WaterLily equals 1 velocity unit of 2.42 [$\frac{cm}{s}$]. To scale resulting velocities, the scaling in Equation 3.4 was applied, where U_{avg} is the characteristic velocity given in Sahin et al. (2009). The numerical viscosity in WaterLily is computed to match the input Reynolds number $Re = 302$ [-], through solving Equation 3.34.

$$\nu = \frac{UD}{Re} \tag{3.34}$$

WaterLily uses a non-dimensional input time, which was introduced in Equation 3.5. Simulation duration was defined as a multiple of cycles, so the non-dimensional time t_i is now defined in $[0, n_{cycle}]$. Within the solver, this is converted to a numerical time t, which is also the unit of the time step Δt. Convective time units were converted into numerical time with the scaling in Equation 3.35. The appropriate time step was determined with a convergence study given in subsection 4.1.3.

$$t = t_i \frac{D}{U} = t_i \frac{2^p}{1} \tag{3.35}$$

To check the accuracy of the scaling parameters, a comparison is made between the dimensionless parameter St used in this simulation and given in Sahin et al. (2009). The resulting Strouhal number in this simulation setup was 0.52, equal to the provided value.

$$St = \frac{D}{UT} = \frac{D}{U(TD)} = \frac{1}{1.936} = 0.52[-] \tag{3.36}$$

3.3.3. Signed Distance Function and Kernel Width

A numerically appropriate geometry requires a well-defined signed distance function that is sensitive to numerical settings. The signed distance function (SDF) represents the body within WaterLily by appending a signed value to each domain cell. The kernel width ϵ is a measure of the area where fluid and solid equations overlap. The polyline degree is the degree of the curve describing the jellyfish shape. The influence of these parameters on the geometry is discussed, as issues occurred during the construction of this model that required the earlier described simplifications.

Signed distance function (SDF). In WaterLily, solid bodies are represented by a signed distance function $d(\mathbf{x}, t)$, which returns the shortest distance from a grid location $\mathbf{x}$ to the body surface, with the sign indicating whether $\mathbf{x}$ lies inside or outside the body. A value of $d < 0$ lies inside the body, $d > 0$ in the fluid, and $d = 0$ on the body boundary. Sampling $d(\mathbf{x}, t)$ on the grid therefore defines the moving boundary as the set of $\mathbf{x}$ where $d = 0$ and can describe complex, time-dependent geometries. The ParametricBodies extension is appropriate for this approach because a parametrised shape enables efficient evaluation of $d(\mathbf{x}, t)$ from a small set of geometric parameters. This jellyfish model uses a body surface constructed from spline curves through prescribed control points. So modifying the control-point locations (and the spline definition used to connect them) alters the surface geometry and the resulting distance field $d(\mathbf{x}, t)$. Hence, moving the control points results in a body that moves within the fluid domain. The 2D signed distance function for this jellyfish geometry is shown in Figure 3.7 at the initial time step of the simulation. Negative red values in the body and positive blue values in the fluid are observed. The observed white line shows the body boundary.

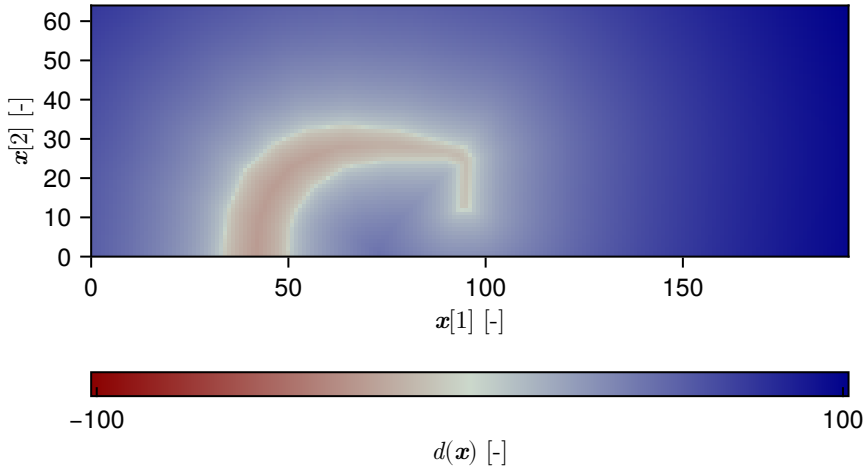

Figure 3.7: Two-dimensional slice of the three-dimensional domain with signed distance values of the geometry, at $t_i = 0$.

The kernel width is a measure of the region where fluid and solid collide, thus near the location where the signed distance function equals 0. This is shown in Figure 3.8 as the smooth region (ϵ), with the solid Ω_b and fluid Ω_f at the respective inside and outside of the region. The kernel width is required to match the fluid and solid equations. Increasing the kernel width results in a larger region where pressure

differences between solid and fluid can be 'smeared' and works as a filter for pressure peaks. A small kernel width is generally more accurate for rapid geometry changes, but it also increases local pressure peaks because the solver has a smaller region to compensate for them. It is therefore best to choose a relatively small kernel width, with reduced pressure peaks while maintaining accuracy. For these simulations, a kernel width of 2 grid cells was deemed acceptable for accurate geometry description.

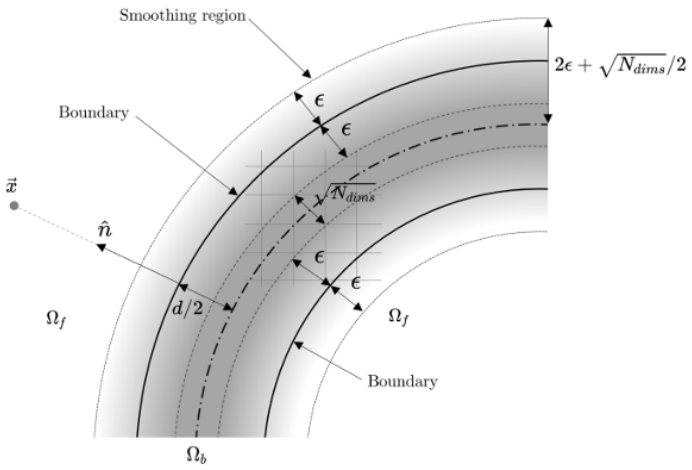

Figure 3.8: Schematic overview of the region between the solid and fluid boundaries, reproduced from Lauber et al. (2022). The kernel width ϵ and the boundary smoothing region are shown.

During the construction of this numerical model, several problems occurred in the signed distance function that defined the geometry. Problems that occurred were ghost geometry cells and inside-out geometry parts, especially around the flap. This led to adjustments in the geometry definition to solve these problems. A degree-1 polynomial was used to connect the control points, resulting in a linear connection. Higher-order polynomials resulted in errors in the signed distance function, a problem that is solved in the newer version of the ParametricBodies extension [2]. In addition, the flap size was slightly increased to avoid inside-out regions in this thin region of the geometry. This problem of thin geometries has been addressed in Lauber et al. (2022).

3.4. Research Methodology

The developed model requires numerical benchmarking and physical validation, conducted through a series of convergence and validation studies. In addition, the performance of the model and the implemented kinematic algorithm was evaluated through simulations in which kinematics were varied to identify optimal actuation modes.

3.4.1. Convergence and Validation

In CFD studies, numerical convergence is an important indicator of the reliability of the results obtained. Convergence was assessed by systematically varying a set of numerical parameters until solution behaviour did not significantly change with further refinement. Physical validation of the model was assessed by comparing simulation results with numerical and experimental data reported in the literature for *Sarsia tubulosa*, as discussed in section 2.4. The present model adopts the shape, kinematics, and characteristic parameters defined by Sahin et al. (2009). Their axisymmetric model provides reference data that enable direct comparison for validation.

A base case configuration was defined and used for the convergence and validation studies. The base case consists of a 3D quarter-domain jellyfish simulation, with the kinematic settings given in Table 3.2. This base case does not include any kinematic variation to the model of Sahin et al. (2009) and is therefore identical, ensuring the comparability.

To confirm the numerical convergence, the grid size D, domain size (as a function of D), and the time step

[2] See GitHub issue: ParametricBodies.jl Issue #31

velocity scale	U	1.00
initial velocity	[-]	$(0, 0, 0)$
duty cycle	γ	0.40
first period	T_1	1.00
second period	T_2	1.00
gliding interval	T_g	0.00

Table 3.2: Kinematic settings of the base case. These are the same kinematic settings as in Sahin et al. (2009).

Δt were varied. To verify the appropriate values, the base case was simulated, with a grid size ranging from $2^4 \rightarrow 2^7$, domain size from $(6, 2, 2) \rightarrow (3, 1, 1) \cdot D$ and maximum time step from $0.25 \rightarrow 0.05$. The time step in WaterLily simulations is generally determined internally by enforcing the Courant-Friedrichs-Lewy (CFL) stability condition. In WaterLily, this is implemented as $\Delta t = min(\Delta t_{max}, \frac{\Delta x}{\Delta u})$, where Δu is the maximum advecting velocity in a single grid cell. The maximum time step, Δt_{max}, provides an upper bound on the time step size and can be varied. The filtered force was computed in each simulation and used for the convergence check, as it serves as the basis for calculating the acceleration, velocity, and position of the centre of mass. The root-mean-square error (RMSE) was calculated according to Equation 3.37, where f_j is the instantaneous force of the simulation and f_{Tj} is the reference value, which is the instantaneous force of the simulation with the finest parameter value. The results are presented in section 4.1.

$$rmse(f) = \sqrt{\frac{\sum_{j=1}^{N}(f_j - f_{Tj})^2}{N}} \tag{3.37}$$

The base case, with converged numerical settings, was used to validate the physical results. In a set of studies, the input kinematics and resulting dynamics were compared to the experimental data of swimming hydromedusae in Colin and Costello (2002), and the CFD results in Lipinski and Mohseni (2009), Sahin and Mohseni (2009), and Sahin et al. (2009). The prescribed kinematics were validated through comparing geometry frames during one motion cycle to those presented by Sahin et al. (2009). The geometry and motion accuracy after applying the smoothing and optimisation algorithms to the control points was observed and quantified. For quantification purposes, the normalised root-mean-square error (NRMSE) was applied, which is the RMSE normalised by the signal amplitude, as in Equation 3.38. This quantifies amplitude and phase differences. However, it can be sensitive to peak values.

$$NRMSE(y) = \frac{\sqrt{\frac{\sum_{t=1}^{T}(y_{1,t} - y_{2,t})^2}{T}}}{y_{1,max} - y_{1,min}} \tag{3.38}$$

The instantaneous oral cavity volume and the velar opening diameter over 2 motion cycles were compared to the values given in Lipinski and Mohseni (2009). The oral cavity volume is the volume of water inside the jellyfish's cavity. The velar opening diameter is the distance between the outer edges of the jellyfish velum. These parameters can be computed from the geometry control points. The cavity volume can be computed by evaluating the volume enclosed by the inner control points, using Equation 3.8. The velar opening diameter is twice the distance from the y-axis to the outermost control point on the velum. The final validation consisted of comparing the resulting base case dynamics to those presented in Colin and Costello (2002) and Sahin et al. (2009).

3.4.2. Parametric Study Design

An objective of this research was to apply the developed numerical model in a parametric study, in which selected kinematic parameters are varied to identify efficient actuation settings for *Sarsia tubulosa*. section 2.4 discussed a set of similar studies, regarding swimming performance (computation) of *Sarsia tubulosa*. Based on the identified limitations and recommendations in these studies, a benchmark study was defined to assess a new set of kinematic parameters. This research investigates the influence of duty cycle variation, successive motion period variation and gliding intervals on the propulsive perfor-

mance of *Sarsia tubulosa*. A set of simulation matrices is defined to present the simulations conducted for these studies.

A set of 12 duty cycle variation cases ($1 \rightarrow 12$) was defined as in Figure 3.9, with no periodic variation and gliding time included in the kinematics. The Figure shows which duty cycle is simulated in each simulation case. Case 1 is identical to the base case with a duty cycle of 0.40 [-]. Cases $2 \rightarrow 8$ have a higher duty cycle, whereas cases $9 \rightarrow 12$ have a lower duty cycle. Baldwin and Battista (2021) stated that duty cycles of $0.4 \rightarrow 0.5$ offer good possibilities for increased propulsive efficiency, which will be assessed with these simulation cases.

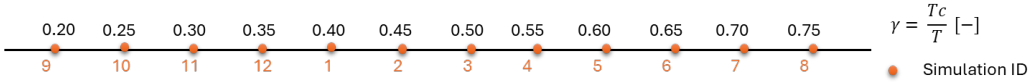

Figure 3.9: Seven base cases with $\gamma = 1 \rightarrow 12$ simulated to determine an optimal duty cycle of *Sarsia tubulosa*.

The simulation matrices in Figure 3.10 show the variations of the period (Figure 3.10a) and gliding time (Figure 3.10b) that were simulated. Simulations were conducted on the range of duty cycles deemed optimal (for propulsive improvements) by Baldwin and Battista (2021). Another matrix, in Figure 3.11, represents the simulation setup for gliding interval and period variation.

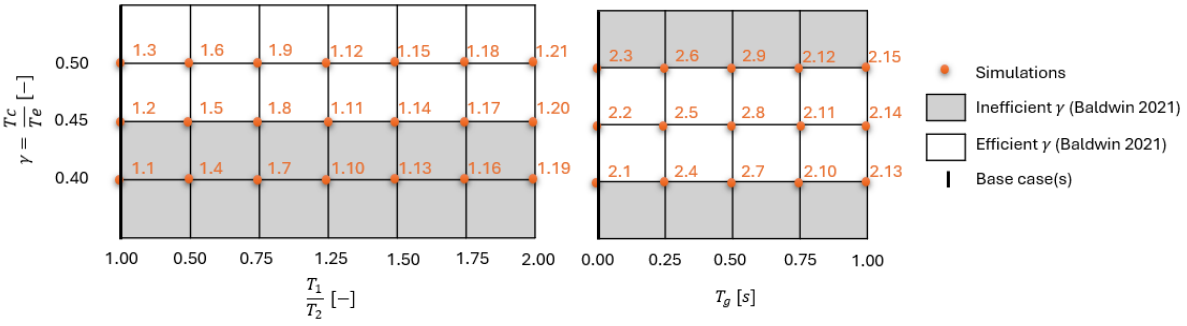

(a) Variation of successive periods

(b) Variation of gliding time

Figure 3.10: Simulation matrices presenting the conducted simulations with the applied kinematic variations, studied with the present model.

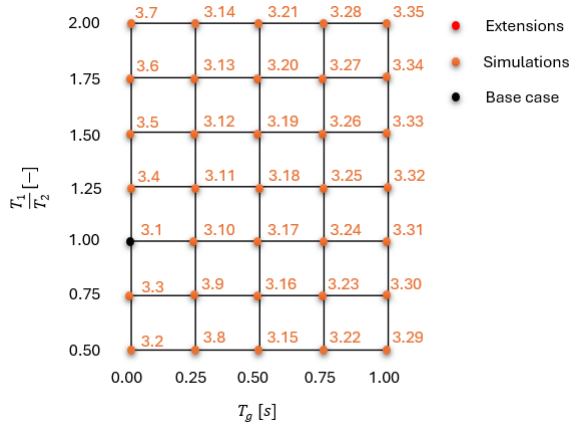

Figure 3.11: Simulation matrix presenting the simulations conducted where varying successive periods and gliding time are combined.

To assess the propulsive efficiency of the jellyfish in each case, an appropriate parameter was defined. Although the non-dimensional velocity of the jellyfish centre of mass was an appropriate measure for propulsion, it does not include the cost of this propulsion. The cost of transport, as defined by Baldwin and Battista (2021) and Bale et al. (2014), was used as a reference to define a similar cost of transport

in WaterLily. The cost of transport was given as the fraction of input (contraction) power and generated velocity, or similarly, the work divided by position change. Baldwin and Battista (2021) defined the cost of transport COT as in Equation 3.39, using the contraction power and non-dimensionalising it with a set of characteristic parameters. Only the steady-state swimming performance was evaluated, excluding start-up effects.

$$COT = \frac{\sum_{j=1}^{N} |F_j||U_j|}{N(\frac{1}{T})^2 V \bar{u}} \tag{3.39}$$

To acquire a similar COT in WaterLily, Equation 3.42 was used. This scaling uses the tip velocity and hydrodynamic contraction force to calculate the input power. This assumes that the force exerted by the jellyfish on the surrounding fluid equals the force exerted by the fluid on the body. The tip velocity is computed as the position change of the control point on the velum edge, divided by the time step. The power equals a multiplication of force by tip velocity, which is then divided by the mean forward velocity of the centre of mass to obtain the cost of transport. Tip velocity was calculated as the change in position of the outer velum control point per time step, as in Equation 3.40. The instantaneous power is computed by multiplying the tip velocity by the translational force, as in Equation 3.41. The fraction $\frac{1}{(UD)^2}$ can be applied to non-dimensionalise this cost of transport. The non-dimensionalisation is the same as used for the force, as the two velocities cancel out. The cost of transport is therefore measured as a non-dimensionalised fraction between mean input power and mean forward velocity. Case-specific adjustments to this approach may be required when evaluating the effects of gliding intervals and longer periods.

$$u_{tip} = \| \frac{\mathbf{cp}_{tip}(t + \Delta t) - \mathbf{cp}_{tip}(t)}{\Delta t} \| \tag{3.40}$$

$$P_{inst} = u_{tip} |F_x| \tag{3.41}$$

$$COT = \frac{\bar{P_{inst}}}{\bar{u}} \tag{3.42}$$

Similar to Baldwin and Battista (2021), the steady-state swimming was used for the evaluation of the COT. This steady-state is marked by the blue area in Figure 4.11a. To identify the first cycle with statistically 'converged' signals, the algorithm in Appendix A was used. This algorithm identifies the time step at which a signal is statistically stationary, based on periodic mean and standard deviation. The mean velocity $\bar{u}$ of the blue area was used for COT computations. Similarly, the fully evolved instantaneous force was used for P_{inst} computation. Therefore, the COT does not include start-up effects, and the efficiency metric was applied to the steady-state motion of *Sarsia tubulosa*.

4

Results

This chapter presents the results acquired with the developed model. The defined base case and applied methods were introduced in section 3.4. Sections 4.1 and 4.2 demonstrate the numerical and physical agreement of this model and the research it supports. The base case results are discussed in Section 4.3, including the force decomposition and wake behaviour in this model. Section 4.4 presents the results for duty cycle variation. In Section 4.5, the results of the kinematic variation studies are presented, including periodic variation, gliding interval addition and a combination. In this work, these studies were used to benchmark the model capabilities. This work should expose modelling problems and uncertainties, which are presented in Section 4.6. The observed results and problems will be discussed and compared to the literature in chapter 5.

4.1. Numerical Verification

The convergence studies regarding the numerical settings are given below. Convergence studies regarding grid size, time step and domain size were conducted.

4.1.1. Grid Size

A grid convergence study with grid sizes $D \in \{16, 32, 40, 48, 56, 64, 128\}$ was conducted, where the instantaneous hydrodynamic force signal was collected during steady-state swimming. The resulting RMSE of the non-dimensional force relative to the finest grid solution $D = 2^7$, which was used as the reference solution, is shown in Figure 4.1a. The results indicate a trend of decreasing RMSE with increasing grid size. However, grid independence is not achieved within the tested range. The instantaneous force signal over 1 motion cycle is presented in Figure 4.1b for varying grid size, to illustrate the error-inducing differences. The coarsest grid sizes of $16 \rightarrow 32$ exhibit deviations in force magnitude, phase and noise. The intermediate grid sizes $48 \rightarrow 64$ capture the main force characteristics and cycle structure. A RMSE of 0.08 was observed between $D = 2^6$ and 2^7. This is attributed to differences in peak regions between these grid sizes, where the force signal for $D = 2^6$ slightly overshoots. Considering the computational costs and purpose of the present study, the grid size of $D = 2^6$ was selected. The RMSE of 0.08 was considered acceptable for the present validation and benchmarking study, although it must be accounted for when interpreting the results. The choice represents a compromise between numerical accuracy and computational feasibility. Differences in (peak) force magnitude influence derived dynamics and efficiency metrics. Therefore, the presented results regarding validation and efficiency evaluation include an error resulting from the numerical settings.

4.1.2. Domain Size

The domain size was examined by comparing the hydrodynamic force for a case with domain size $(3D, D, D)$ and $(6D, D, D)$. In Figure 4.2, the instantaneous force signals for both domain sizes are given. It was observed that differences in force are small. As a result, the RMSE of the domain size $(3D, D, D)$, relative to the solution for the domain size $(6D, 2D, 2D)$ equals 0.04. To compute accurate dynamic parameters from the model, the smallest domain size is appropriate. The accuracy of this

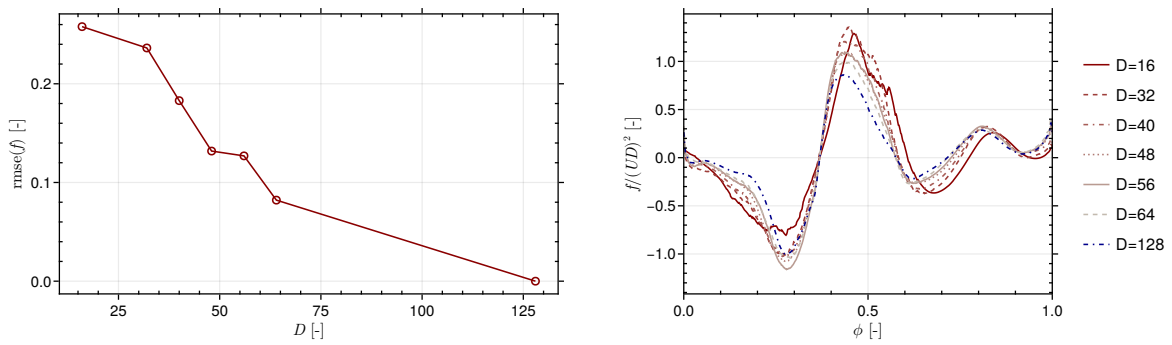

(a) Root mean square error

(b) Instantaneous hydrodynamic force over 1 motion cycle

Figure 4.1: Convergence statistics of the grid size D. The root mean square error (**a**) of the hydrodynamic force over 1 motion cycle (**b**), with respect to the finest grid size.

small domain size was attributed to the use of the Biot-Savart boundary conditions. It was observed that for both domain sizes, the expelled jet/vortex rings developed outside the translational direction of the domain, shown in Figure 4.12. A larger domain size in the translational direction is more appropriate for vorticity and wake studies. To compute the propulsive metrics and efficiencies, the domain size $(3D, D, D)$ was used. For vorticity and wake studies, the domain size $(6D, D, D)$ was applied.

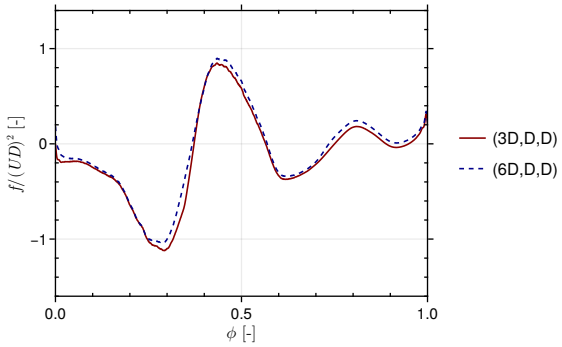

Figure 4.2: The instantaneous hydrodynamic force signal for varying domain size over 1 motion cycle.

4.1.3. Time Step

A convergence study to determine an appropriate Δt for simulations was conducted with the values $\Delta t = 0.05, 0.10, 0.15, 0.20, 0.25$. The CFL restriction built into WaterLily, in combination with this control point and the NURBS modelling approach, requires finer grids to be simulated with a time step of $\Delta t = 0.05$. For finer grids, the spatial scale decreases and the CFL restriction is violated for larger time steps. Therefore, it was only possible to conduct a time step convergence study for a grid size of 32. The resulting RMS errors are presented in Figure 4.3 and the instantaneous force signal in Figure 4.3b. The RMSE values become up to 0.3 relative to the finest time step. This difference is also observed in the filtered force signals, where the force of $\Delta t = 0.05$ is larger during contraction and expansion. The same errors are computed for the unfiltered forces, given in Appendix B. The unfiltered force shows higher noise levels for smaller time steps, while the underlying force balance also changes. This indicates that time-step convergence of the hydrodynamic force could not be established, as temporal refinement consistently adjusts force peaks. It is difficult to attribute this behaviour to a specific part of the model. It may be that the pressure peaks resulting from the unsteady control point motions are better resolved for smaller Δt, inducing the observed high-frequency noise. The observed difference may also be related to the applied force filter, as the smoothing parameter α depends on the numerical time step. However, since the behaviour is observed for both filtered and unfiltered force, the filter is not considered the main cause. The filter may suppress high-frequency oscillations and induce a phase lag, but the difference in force balance is already present. To simulate on a grid size of $D = 2^6$, which was determined previously,

the time step is restricted to $\Delta t = 0.05$, and this was therefore used in the present model.

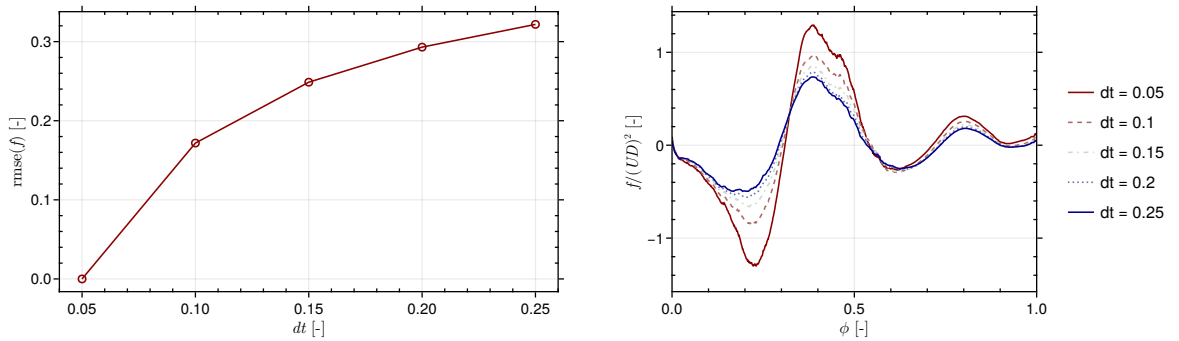

(a) Root mean square error

(b) Instantaneous hydrodynamic force

Figure 4.3: Convergence statistics of the numerical time step Δt. The root mean square error (**a**) of the hydrodynamic force over 1 motion cycle (**b**), for varying time step Δt, using the smallest time step as reference value.

4.2. Validation

The experimental and numerical results given in Colin and Costello (2002), Lipinski and Mohseni (2009), and Sahin et al. (2009) were used to validate this model. Their numerical results were computed using a different modelling approach from that employed in the present research. The method described by Sahin and Mohseni (2009) is an axisymmetric ALE solver, whereas this research uses a finite volume approach on a uniform Cartesian grid, as described in section 3.1. The experimental results of Colin and Costello (2002) regard a different-sized jellyfish with $D = 0.85$ [cm], and the validation results were therefore computed with a scaled version of the base case.

4.2.1. Geometry and Motion Validation

To confirm the accuracy of the jellyfish motion cycle, the jellyfish shape/motion frames were compared to Figure 2.5 by plotting the $d(\mathbf{x}, t) = 0$ contour of the signed distance function, the body boundary, at the same time steps as in the Figure. A two-dimensional slice of the three-dimensional model was used for this visualisation. The comparison of the kinematic settings is presented in Figure 4.4, at the times $t = \{1, 2, 3, 4, 5, 6, 7, 8, 9\}T/10$ and $t = \{4, 5, 6, 7, 8, 9\}T/10$. The dark red dashed lines represent the jellyfish outline of this model at the given time step, while the other lines are the shapes presented in the paper. The legend shows what colour corresponds to the given time step. It was observed that the geometry outlines at each time step are similar, although velum thickness deviates. This deviation was attributed to the thicker velum applied in the present model, compared to the digitised bell shape in Sahin et al. (2009).

The thicker velum adjusts oral cavity volume and velar opening diameter. Therefore, an additional kinematic validation concerned the oral cavity volume and velar opening diameter. The results of the present model were compared to those reported by Lipinski and Mohseni (2009). Figure 4.5a and Figure 4.5b present the comparison of the non-dimensional oral cavity volume and velar opening diameter, respectively. The solid red lines represent the WaterLily-computed parameters and the dashed blue lines the data from Lipinski and Mohseni (2009). In Figure 4.5b, D denotes the maximum bell diameter and D_v the velar opening diameter. The root-mean-square error between the present model and the validation data, normalised by the signal range, corresponds to 0.113 [-]. The velar opening diameter shows a similar deviation, also having an NRMSE of 0.113 [-]. This moderate NRMSE confirms the general agreement between the methods. However, deviations between the geometry of the present model and that in Lipinski and Mohseni (2009), which are attributable to simplifications and assumptions, affect the resulting kinematics.

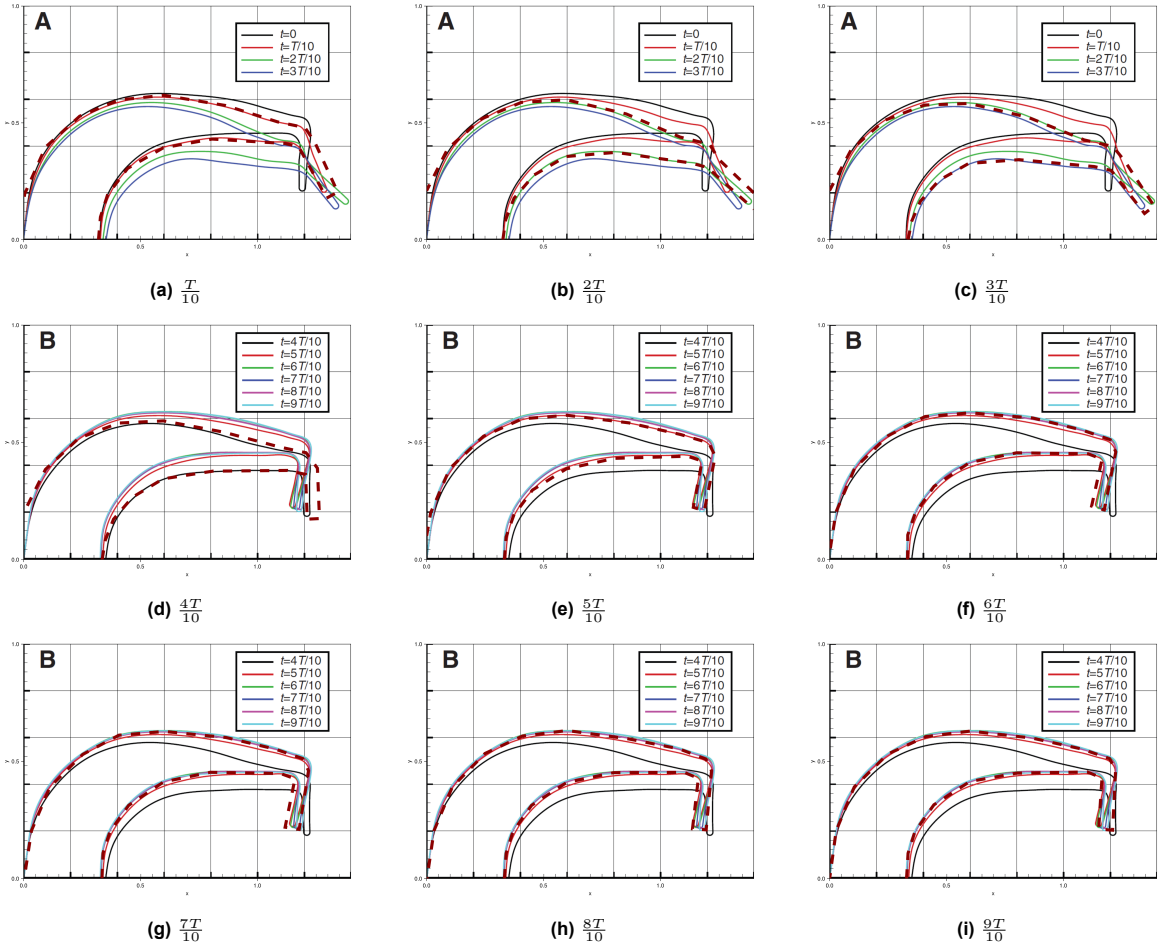

(a) $\frac{T}{10}$ **(b)** $\frac{2T}{10}$ **(c)** $\frac{3T}{10}$

(d) $\frac{4T}{10}$ **(e)** $\frac{5T}{10}$ **(f)** $\frac{6T}{10}$

(g) $\frac{7T}{10}$ **(h)** $\frac{8T}{10}$ **(i)** $\frac{9T}{10}$

Figure 4.4: Comparison of the geometry shape of the present model to the kinematic frames reproduced from Sahin et al. (2009) for 9 time steps in a single motion cycle.

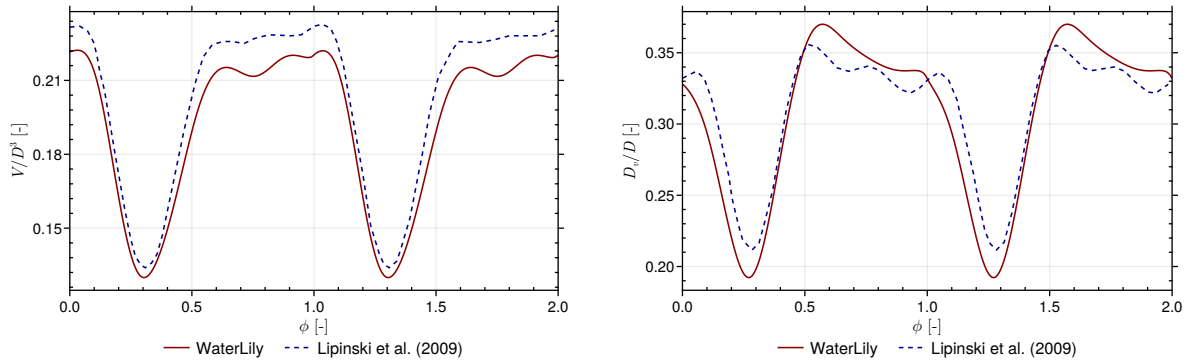

(a) Oral Cavity Volume **(b)** Velar Opening Diameter

Figure 4.5: Comparison of the oral cavity volume and velar opening diameter in the present model to the numerically computed volume reported by Lipinski and Mohseni (2009) over 2 motion cycles.

4.2.2. Dynamics Validation

With the simulation settings and prescribed kinematics confirmed, the base case can be simulated to compare dynamic results to those presented by Sahin et al. (2009). Figure 4.6a presents the non-dimensional velocity obtained in the present study and the results reported by Sahin et al. (2009), shown as the red and blue lines, respectively. The velocity data from Sahin et al. (2009) was non-dimensionalised using the average velocity U_{avg}, such that $\frac{u}{U_{avg}} = \frac{1}{2.42}u$. In the present simulations, the velocity was scaled by a factor of $\frac{u}{U} = u$. The general shape and magnitudes of the velocity curves show similar behaviour. An average phase difference of $\bar{\Delta\phi} = 0.04$ is observed in Figure 4.6a, and the RMS error normalised by the velocity range equals 0.203 [-]. The hydrodynamic force coefficient of this model was compared to the instantaneous force coefficient in Sahin et al. (2009) in Figure 4.6b. The instantaneous force coefficients also match well, although, similarly to the velocity, phase differences were observed. Additionally, force peaks occur at the beginning/end of each motion cycle for this model. This is a result of the transition between motion cycles, which was not smoothed, as it altered the kinematics excessively. The comparison may improve from smoothing this transition region. The NRMSE of the force signal of this model compared to that of Sahin et al. (2009) is 0.170 [-]. The observed phase differences were attributed to the force filter, which induces a phase lag of 0.045, as velocity is computed from the filtered force. The contribution of this phase lag to the NRMSE values is significant. Without this phase lag, the velocity NRMSE is 0.148 and the force NRMSE equals 0.106. The force filter therefore accounts for 37% of the error.

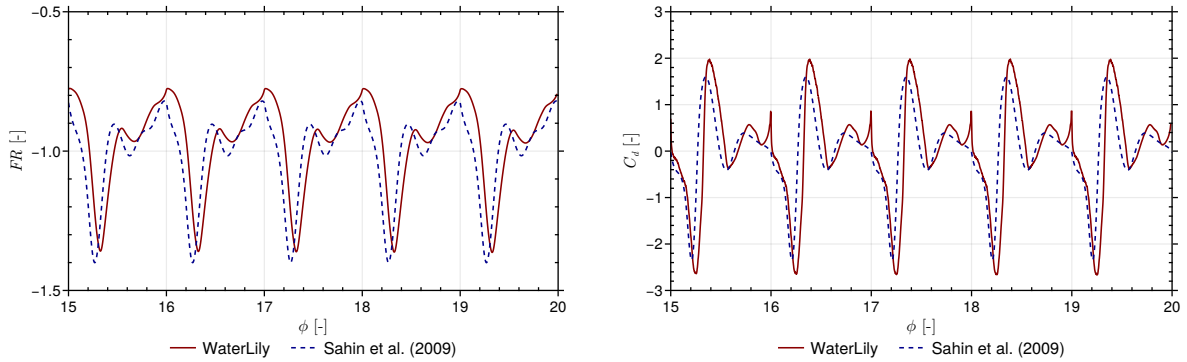

(a) Velocity

(b) Non-dimensionalised force

Figure 4.6: Comparison of the instantaneous non-dimensional velocity and drag coefficient to the numerically computed data in Sahin et al. (2009), respectively. The velocity of Sahin et al. (2009) was non-dimensionalised with the mean velocity U_{avg}. The WaterLily force coefficient was computed as $\frac{2Fx}{(UD)^2}$

A separate dynamical comparison was made to the experimental data in Colin and Costello (2002). These data concern a smaller jellyfish with $D_{max} = 0.85$ [cm], thus the input parameters were scaled accordingly. The velocity scale and Reynolds number were computed from the experimental data presented in Colin and Costello (2002) by computing the mean values. Figure 4.7a presents the instantaneous fineness ratio (h/D) over 4 motion cycles for this model in red and the experimental data of Colin and Costello (2002) in blue. The fineness ratio shows a similar trend, but the magnitude differs with overshoot in peaks, resulting in an NRMSE of 0.338 [-]. Figure 4.7b shows the instantaneous, non-dimensionalised velocity over 5 motion cycles. The velocity is generally higher than that found by Colin and Costello (2002) combined with a phase difference. The computed NRMSE was 0.584. In both figures, there is a phase mismatch, attributed to the varying periods and duty cycles in real-time swimming of *Sarsia tubulosa*.

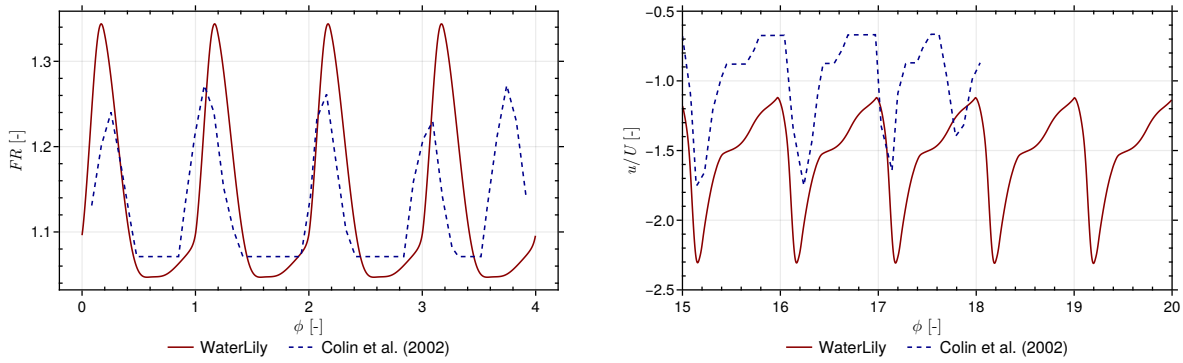

(a) Fineness Ratio

(b) Velocity

Figure 4.7: Comparison of the instantaneous fineness ratio and non-dimensionalised velocity to the experimental data reported by Colin and Costello (2002). The velocity of Colin and Costello (2002) was normalised with the mean velocity.

4.3. Base Case

A base case with kinematic settings identical to those in Sahin et al. (2009) was simulated to analyse model behaviour.

4.3.1. A Comparison of the 2D and 3D Model

To assess the influence of dimensionality, the base case was simulated using both a two-dimensional, a quarter and a full three-dimensional model. The simulations were conducted with the same kinematic settings. Minor differences in control point positions arise from the enforcement of mass conservation, which is based on area conservation in 2D and volume conservation in 3D. To verify the consistency of the prescribed kinematics in 2D and 3D, the evolution of the oral cavity volume is shown in Figure 4.8.

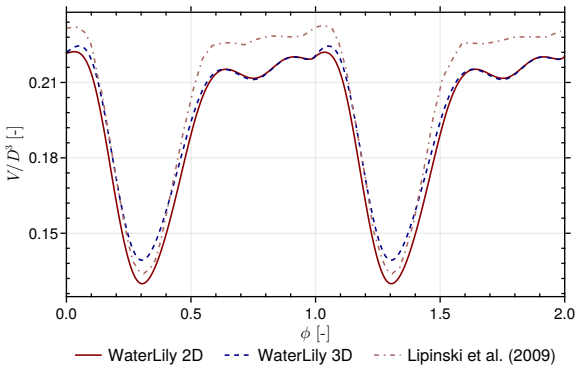

Figure 4.8: Comparison of the oral cavity volume in 2D, 3D and Lipinski and Mohseni (2009), over 2 motion cycles.

This confirms that the same kinematic cycles were applied to both simulations, enabling a direct comparison of their hydrodynamic responses. The quarter and full 3D simulation yielded identical dynamic results, which was expected from the symmetrical boundary condition check in chapter 3. However, significant differences are observed in the resulting dynamics of 2D and 3D simulations. As shown in Figure 4.9a, the force histories exhibit similar behaviour, but differ especially for the contraction phase. The contraction-phase thrust peak occurs at a different instant in the cycle and with a smaller magnitude. The net thrust generated over one cycle is lower in the 2D model, resulting in a significantly reduced swimming velocity, shown in Figure 4.9b. The 2D hydrodynamic force, even after smoothing, also exhibits a higher level of numerical noise compared to the 3D simulations. This is attributed to the reduced degrees of freedom available in two dimensions to redistribute pressure and vorticity, leading to stronger local fluctuations.

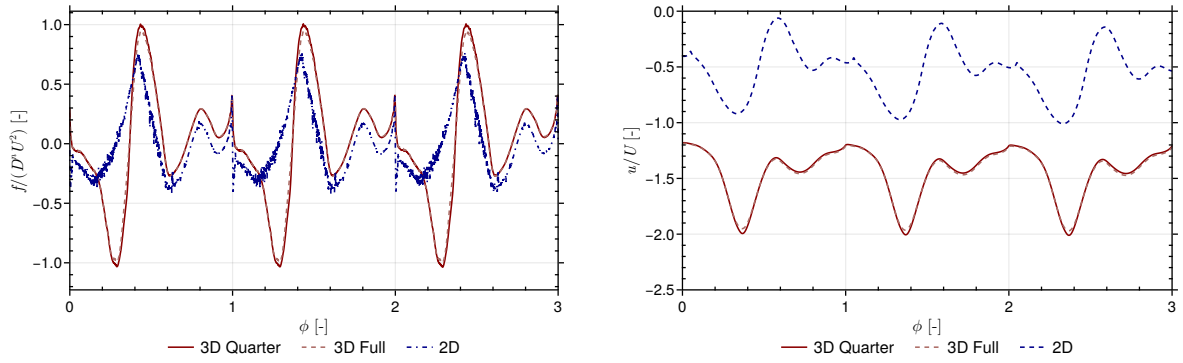

(a) Non-dimensional hydrodynamic force

(b) Non-dimensional translational velocity

Figure 4.9: Comparison of the dynamical results between the 2D and 3D models over 3 motion cycles.

The observed differences in force timing indicate that the hydrodynamic response to bell contraction is dimension-dependent. The development and transport of vortical structures differ fundamentally between the two models, which was observed by comparing the 3D vorticity contours in Figure 4.12 to the 2D contours in Appendix C. In the 3D case, the expelled shear layer rolls up into vortex rings, which move downstream and rapidly detach from the body. In the 2D model, planar vortices form and move slowly, remaining in the vicinity of the velar aperture for longer. This results in a longer interaction between body and wake, which appears to alter the instantaneous force balance and reduce the contraction-phase force peak. The full 3D simulation exhibits asymmetries in the vortex structures. These asymmetries are not present in the mirror-reflected quarter-domain wake field in Appendix D. The observed differences were attributed to symmetry assumptions in the quarter model that do not capture the full 3D vortex ring dynamics. The full 3D model does capture these dynamics.

4.3.2. Force Decomposition

Figure 4.10 shows the instantaneous force components over time. The pressure force, depicted as the solid red line, dominates over the viscous force, depicted as the dashed brown line. The added mass also exerts a significant influence, accounting for 35 % of the forces on average. The added mass accelerates motion during contraction, whereas it counteracts forward motion during the expansion phase. The viscous forces, which represent skin-friction drag, counteract the forward motion at all times. The pressure force is the sum of the pressure thrust and drag acting on the body. During contraction, the pressure force is the primary contributor to accelerating the body, whereas during expansion, it decelerates. This behaviour is connected to vortex development: the initial vortex ring generates forward thrust, whereas the stopping vortex ring generates negative thrust.

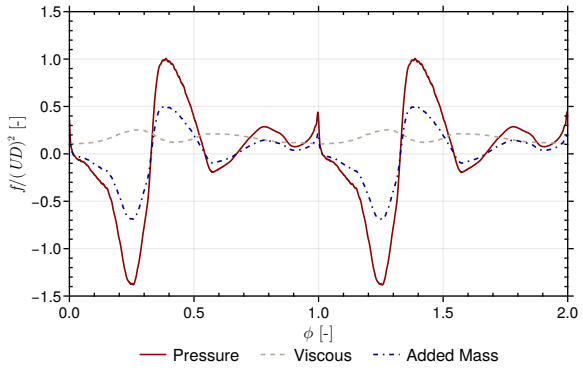

Figure 4.10: Force decomposition in the base case simulation. Presents pressure, viscous and added mass contributions over 2 fully evolved motion cycles.

Centre of mass velocities and displacements are presented in Figure 4.11a and Figure 4.11b, respectively. The jellyfish reaches a steady-state swimming velocity after a few cycles. The blue area in Fig-

ure 4.11a depicts the steady-state region of the base case. In this state, the position increases linearly, as shown in Figure 4.11b. It was observed that *Sarsia tubulosa* moves 51 times its maximum diameter over 20 cycles, including start-up. That averaged to 2.55 times its maximum diameter per motion cycle. Mean velocities (and additional efficiency parameters in the following sections) were computed for the steady-state swimming cycles. The mean velocity for this base case is presented as the dashed brown line in Figure 4.11a.

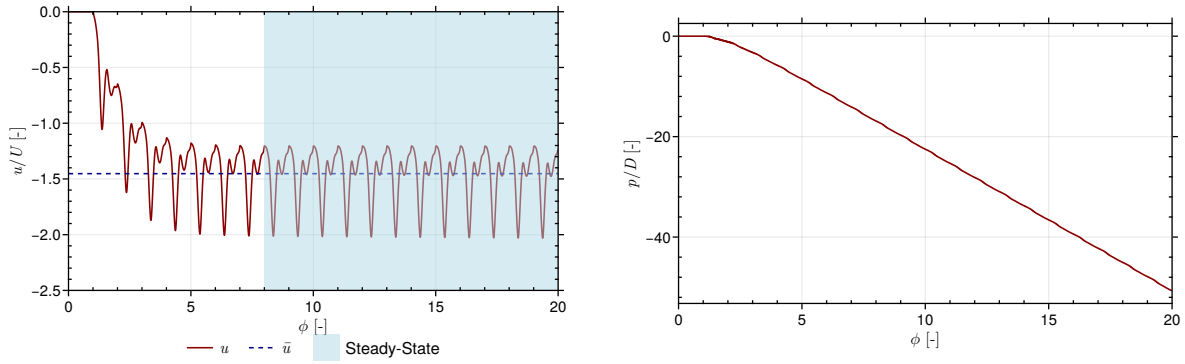

(a) Non-dimensional velocity and mean steady-state velocity

(b) Non-dimensional position

Figure 4.11: Base case non-dimensional velocity and position of the geometry centre of mass. The blue area depicts the region of steady swimming, where a steady-state velocity is reached. The mean velocity is computed from this region.

4.3.3. Vorticity and Wake Development

Figure 4.12 presents a set of vorticity contours over one motion cycle of *Sarsia tubulosa*, depicted for the fully three-dimensional model. The jellyfish is in an evolved state, having a forward velocity before this cycle is initiated. The contraction phase is initiated in Figure 4.12b. Around the velar opening, a vortex ring is formed, which moves away from the jellyfish as an expelled jet when the velum fully opens, causing the thrust peak in Figure 4.10. This is generally defined as the 'starting vortex ring'. The vortex ring moves away, and a long trailing wake was identified in Figure 4.12c and Figure 4.12d. A second vortex ring was identified that is pushed into the subumbrellar cavity as a result of the closing velum, causing the peak in negative thrust in Figure 4.10. This stopping vortex generates flow into the cavity, initiating the expansion phase and refill process to prepare for the next contraction.

A long trailing flow of the vortex ring that moves away from the jellyfish can be observed. It was also observed that the vortex ring moves away 4–5 jellyfish lengths during the motion cycle. Additionally, the trailing edge disconnects from the vortex ring during the expansion phase, and asymmetries in the vortex structure can be observed. This suggests that the vortex ring is not perfectly circular. For optimal vortex formation, the trailing flow behind the starting vortex ring must be insignificant and short, which is not the case in the present model. This will result in non-optimal vortex formation numbers. During expansion, a vortex ring is present inside the cavity. These stopping vortices do not appear in the wake and are therefore less influential in passive propulsion. This means that there is no 'wall effect' functioning as a passive propulsive effect.

(a) t_0

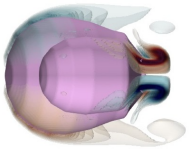

(b) $t_0 + \frac{2T}{10}$

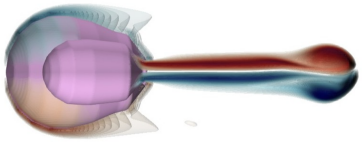

(c) $t_0 + \frac{4T}{10}$

(d) $t_0 + \frac{6T}{10}$

(e) $t_0 + \frac{8T}{10}$

Figure 4.12: Vorticity contours of the 3D model at several time steps in 1 fully evolved motion cycle.

4.4. Duty Cycle Variation

The first kinematic setting that was varied is the duty cycle γ, ranging from $0.2 \rightarrow 0.75$. The performance of each case was evaluated by computing the COT, defined in Equation 3.42. The resulting non-dimensionalised COT, for varying duty cycles, is presented in Figure 4.13a. The results indicate that the propulsive cost is minimal for $\gamma = 0.4$ during steady-state swimming. Shorter or longer contraction phase increased the cost of transport by up to 80 % relative to the optimal duty cycle. Figure 4.13b complements those results with the resulting mean velocity $\bar{u}$ and peak velocity u_{peak} acquired by each duty cycle setting. A forward steady-state velocity was observed for each variation of γ, meaning that in all cases, translational motion was achieved.

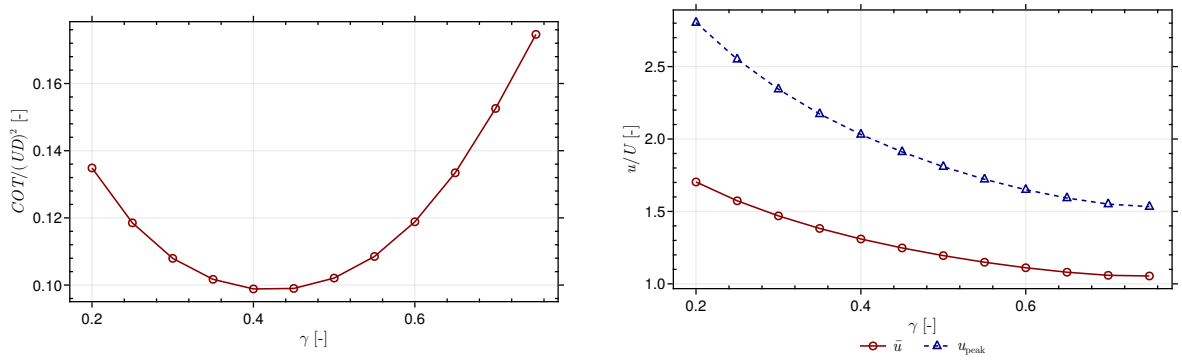

(a) Cost of Transport

(b) Mean and peak velocity

Figure 4.13: Propulsive and efficiency metrics for varying duty cycle.

4.5. Periodic Variation

The consecutive periods, as given in Figure 3.10a, for a duty cycle of $\gamma = 0.40, 0.45, 0.50$, were all simulated and evaluated based on their cost of transport. T_1 remains to be 1.0 [s], whereas T_2 is varied from 0.5 to 2.0 [s]. Computation of the COT was slightly adjusted, as using 1 motion cycle for power computations no longer sufficed. Hence, power was computed over a constant cycle range across all cases. The results are presented in Figure 4.14a, showing the COT for varying consecutive periods T_2. Figure 4.14b shows the variation of mean velocity $\bar{u}$ as the solid red curve and peak velocity u_{peak} as the dashed blue curve. The results indicated that although these velocities decrease with increasing consecutive periods, COT also decreases. This reduction in COT results from a larger reduction in power input compared to the reduction in velocity.

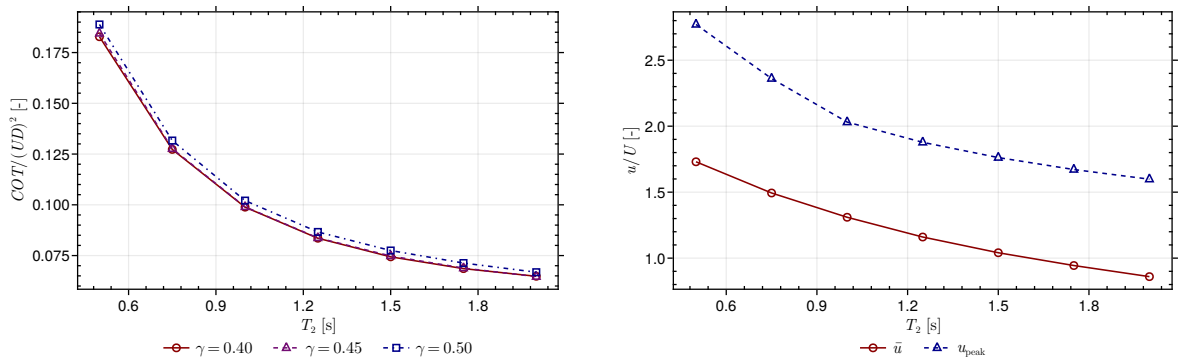

(a) Cost of Transport

(b) Mean and peak velocity

Figure 4.14: Propulsive and efficiency metrics for varying consecutive period T_2 with a duty cycle of $\gamma = 0.40, 0.45, 0.50$.

4.6. Gliding Intervals

The addition of gliding intervals between periods was the next kinematic variation applied to this model. The variations in Figure 3.10b, for a duty cycle of $\gamma = 0.40, 0.45, 0.50$, were simulated. The results are presented in Figure 4.15a, showing the COT for increasing gliding intervals. The observed behaviour is similar across all duty cycle variations. Figure 4.15b shows the variation of mean velocity $\bar{u}$ as the solid red curve and peak velocity u_{peak} as the dashed blue curve for a duty cycle of 0.4. Similar behaviour was observed for gliding intervals as for extended T_2 periods, where the jellyfish maintained a proper velocity for a long time, and the COT continuously reduced. A gliding interval of 2 [s] has an input power that is $\frac{1}{3}$ of the case with no gliding interval. The observed mean velocity reduced to a $\frac{1}{2}$ of the base velocity. Therefore, the COT is expected to continue reducing until these fractions meet or the power fraction exceeds the mean velocity fraction.

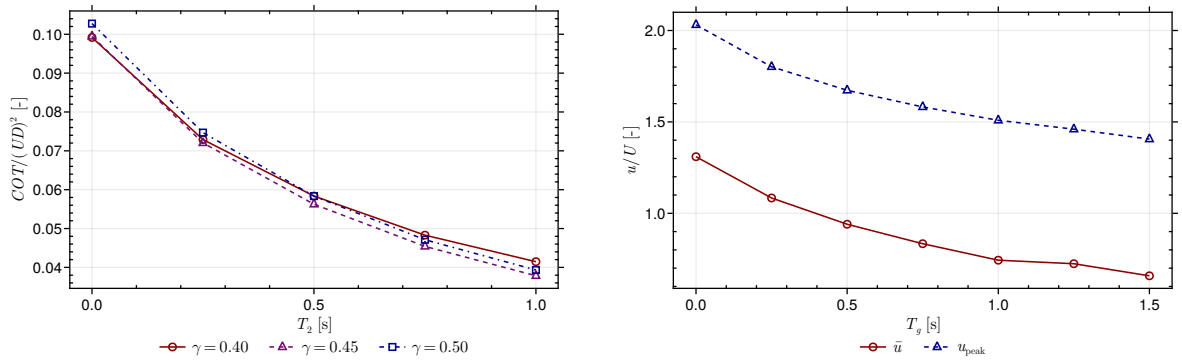

(a) Cost of Transport

(b) Mean and peak velocity

Figure 4.15: Propulsive and efficiency metrics for varying gliding interval T_g with a duty cycle of $\gamma = 0.40, 0.45, 0.50$.

4.7. Combining Kinematic Variations

The final kinematic variation combined gliding intervals with a variable period for a duty cycle of $\gamma = 0.4$. The additional duty cycles are not presented, as their behaviour was identical to that of the base case. Figure 4.16 presents the resulting COT values for varying both the period T_2 and the gliding interval T_g lengths. Again, the optimal behaviour of long periods and gliding interval was observed. A combination of long gliding time and elongated periods resulted in optimal cost of transport, indicated by the dark red area on the top-right in Figure 4.16. This indicates that, within the present model, lower COT occurs for extended periods and gliding intervals. Two optimal settings were observed, for (T_g, T_2) as $(0.75, 1.75)$ or $(0.00, 2.00)$.

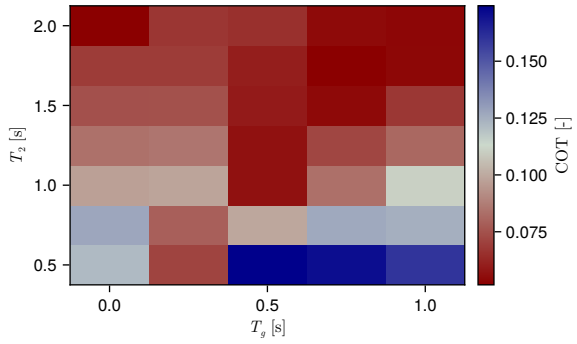

Figure 4.16: Cost of transport for varying T_g and T_2 values with $\gamma = 0.4$.

The COT served as a solid efficiency metric for duty-cycle variations with identical periods. However, the behaviour for gliding intervals and elongated periods suggests a bias in its computation, which rewards long coasting periods during swimming. To identify the cause of the biased COT measure across the

defined cases, the input parameters were studied. The velocity overshoot, already observed during experimental validation, suggests that the mean velocities, resulting from the hydrodynamic force, are continuously overestimated in the present model. Hence, the hydrodynamic forces are examined in section 4.8.

4.8. Sensitivity Analyses on Hydrodynamic Forces

The kinematic variation studies yielded questionable COT results, attributed to steady-state velocities arising from force equilibrium in this model. Therefore, the force equilibrium in the present model was studied. The added mass and drag force were studied separately.

4.8.1. Added Mass Coefficients

The added mass is a known limitation in jellyfish modelling, as no physical added mass coefficient has been defined. Some added mass coefficients have been introduced as approximations for *Sarsia tubulosa* (Daniel, 1983), although in most available models, the cavity volume was assumed to be the only fluid that induces acceleration reaction (Sahin et al., 2009). Initially, the present model applied this last assumption for the added mass coefficient. This model assumes that the added mass equals the fluid volume in the cavity, which moves rigidly with the body. To study the influence of added mass on the motion, the added mass coefficient α_{am} was varied to identify whether other shapes better represent the *Sarsia tubulosa*. A set of added mass coefficients was simulated, including the original case $\alpha_{am,0}$, the hemisphere assumption $\alpha_{am,hemi}$ and the sphere assumption $\alpha_{am,sphere}$. Daniel (1983) presented a regression equation for experimentally determined added-mass coefficients of hemiellipsoids, given as Equation 4.1. This is the fraction of the instantaneous bell height and bell radius, which were computed from the locations of the outermost control points. The sphere assumption applies a coefficient of $\alpha_{am,sphere} = \frac{1}{2}$.

$$\alpha_{am,hemi} = \frac{h(t)}{r(t)}^{1.4} \tag{4.1}$$

Figure 4.17 presents the evolution of the instantaneous jellyfish velocity over 10 motion cycles, for various added mass coefficients in the force equilibrium. For every added mass coefficient, a similar equilibrium state is reached, resulting in similar steady-state velocities. A higher added mass coefficient causes the model to take longer to reach this equilibrium. Eventually, the same velocities are still reached for all coefficients. It was observed that higher coefficients decrease the velocity oscillations in the steady state. This may adjust the peak velocity, but does not yield a difference in mean velocity and therefore COT.

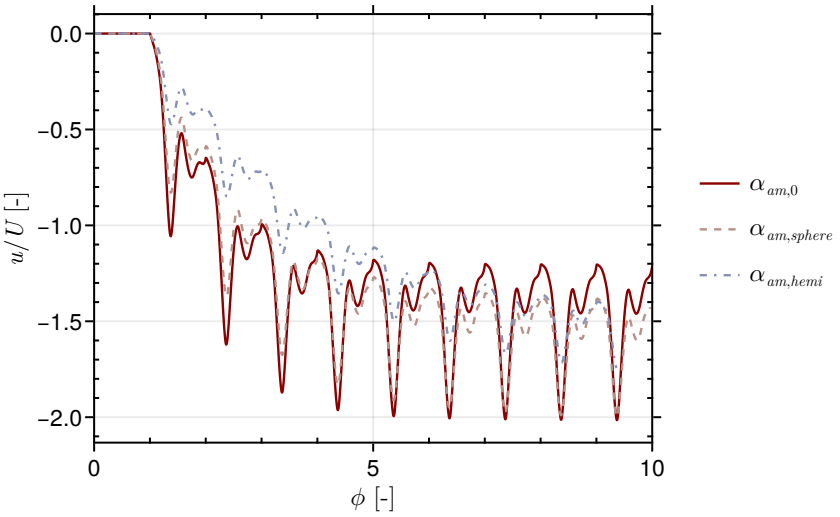

Figure 4.17: The instantaneous velocity for added mass coefficients of several shape assumptions.

4.8.2. Hydrodynamic Drag Force

An additional test concerned the viscous drag force, as this is directly related to deceleration in the model during the gliding interval. (skin friction) Drag is a force that continuously counteracts the velocity, as shown in Figure 4.10. To study how drag affects the simulation results and specifically the COT, the pressure and viscous forces were computed for a case with a long gliding interval. Figure 4.18a presents the non-dimensionalised pressure (solid red line) and viscous (dashed blue line) force over 6 periods. The jellyfish actuates during the first period, and the next 5 periods are an elongated gliding interval. The pressure force is dominant during the actuation period, while viscous drag is more influential during the gliding interval. The viscous force scale is almost indistinguishable from the x-axis, so Figure 4.18b presents the forces during the gliding interval.

To verify the drag force scale, a drag approximation from Hoerner (1965) was computed. This is an analytical drag force that was computed using the drag coefficient of a fully submerged sphere, as adopted by Daniel (1983). Equation 4.2 shows the adopted formula for the drag coefficient. This is added in Figure 4.18 as the brown line. This suggests that the drag forces in WaterLily are of the right order of magnitude. Note that, in this comparison, the Reynolds number was held constant at 302 [-], whereas it may vary. Due to velocity oscillations, the Reynolds number varies throughout the motion cycle, resulting in different drag forces acting on the jellyfish. A lower velocity results in a lower Reynolds number and therefore should increase the drag coefficient.

$$C_d = \frac{24}{Re^{0.7}} \tag{4.2}$$

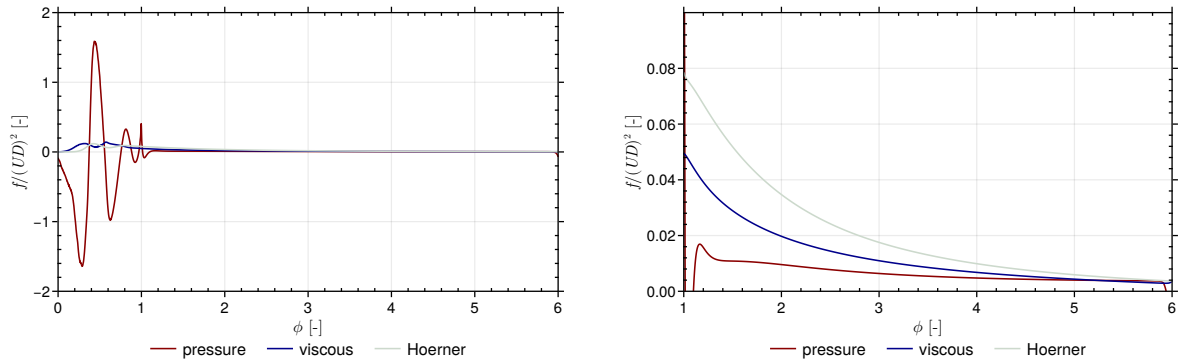

(a) Force decomposition

(b) Force decomposition during gliding

Figure 4.18: Decomposition of pressure and viscous forces during one actuation cycle and 5 periods of gliding. The Hoerner sphere drag is added as a reference value.

An additional simulation was conducted in which the force equilibrium equation was adjusted. The force computation in the model was adjusted to a hybrid method. The pressure force is still computed as in Equation 3.24, while the viscous force is computed as in Equation 4.3, applying the empirical drag formulation of Hoerner (1965). Both a version with a constant Reynolds number and a version with a varying Reynolds number were added. The varying Reynolds number was defined as $Re(t) = \frac{u(t)Re}{U}$ to ensure non-dimensionality. The computed force and velocity signals are shown in Figure 4.19a and Figure 4.19b, respectively, over the same period with a gliding interval of 5 periods. The resulting non-dimensional drag forces are of comparable magnitude, indicating that the hybrid approach does not significantly influence the results.

$$\mathbf{F}_\nu(t) = C_d \frac{1}{2} \pi r^2 \mathbf{u}^2 \tag{4.3}$$

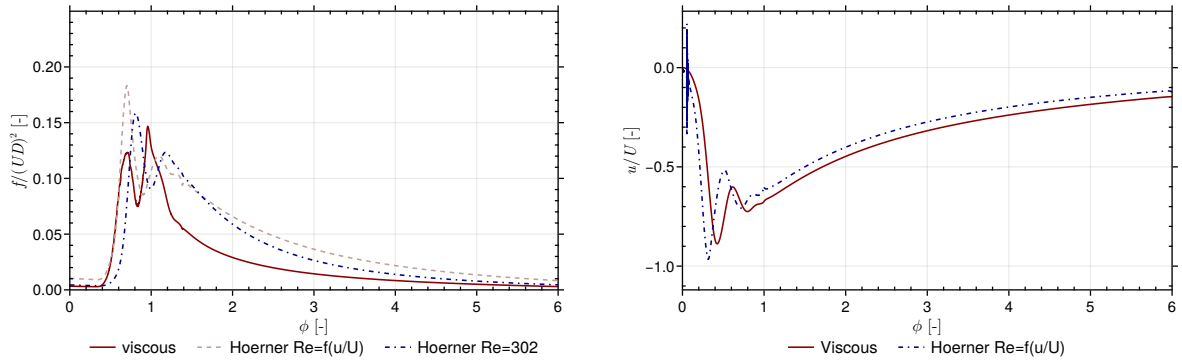

(a) Drag force

(b) Velocity

Figure 4.19: Comparison of the instantaneous drag force and velocity between the full WaterLily approach and a hybrid approach, implementing the Hoerner sphere drag as the viscous force on the model.

5

Discussion

This study demonstrated that a numerical model of *Sarsia tubulosa* with controlled kinematics, implemented in the WaterLily framework, can reproduce its physical behaviour. The model applies prescribed kinematics and neglects fluid-structure interaction and elastic deformation effects. The result is a computationally viable simulation framework that does not include all phenomena in the actual swimming jellyfish problem. A set of studies on the model was conducted to analyse the kinematic and dynamic agreement with reference data, propulsive efficiency and vorticity fields. The following sections discuss these results and place them within the context of existing literature on *Sarsia tubulosa* modelling.

5.1. Methods

The current literature on *Sarsia tubulosa* swimming employs different modelling approaches, including analytical methods, two-dimensional CFD, and axisymmetric CFD. Daniel (1983) and McHenry and Jed (2003) used analytical formulations for conservation of momentum in the jet, approximating force contributions and geometry characteristics. These analytical methods can not resolve vortex dynamics. Dabiri and Gharib (2003) concluded that kinematic approximations in these models influence the dynamical results (added mass and drag estimations). For jetting medusae, these models reasonably estimate propulsion and can be useful for scaling analyses. Baldwin and Battista (2021) applied a 2D CFD model to compute propulsive characteristics. The medusa is approximated as an infinite slice in the spanwise direction. Compared with analytical momentum-conservation models, this adds the option to model vorticity structures and to compute hydrodynamic forces. However, vortex rings can still not form. The axisymmetric ALE model of Sahin and Mohseni (2009), used in Lipinski and Mohseni (2009) and Sahin et al. (2009), solves the governing equations in swirl-free cylindrical coordinates. This assumes perfect rotational symmetry and can capture the formation of a vortex ring. Vortex ring formation will be idealised, as the model cannot capture azimuthal instabilities and 3D wake asymmetries. This is where this full 3D model can make a difference, as it captures the actual vortex dynamics. It solves the governing equations in 3D on a Cartesian grid using an immersed-boundary approach. Three-dimensional effects in the wake can be investigated, while (azimuthal) symmetry assumptions are avoided.

The geometry definition of Sahin et al. (2009), applying NURBS as a geometry contour, was adopted in the present model, in combination with moving control points. This method proved effective in representing the unsteady motion of the jellyfish. In the present model, the fluid force was resolved directly from the simulations, while body deformation was prescribed following documented kinematics, similar to Baldwin and Battista (2021) and Sahin et al. (2009). The resolved forces were applied in an equation of motion similar to Sahin et al. (2009) and Daniel (1983). This offered a good dynamics approximation, while avoiding full FSI modelling. Park et al. (2015) modelled the bell elasticity, solving the governing equations in cylindrical coordinates. Elastic jellyfish models differ from CFD force-balance formulations in that thrust results from the interaction between deformable structures and the surrounding fluid instead of prescribed bell and velum motion. The results in Park et al. (2015) closely resembled the experimental results of Colin and Costello (2002) (Figure 2.6), suggesting a better representation of the swimming *Sarsia tubulosa* than the present model. It also benefits COT computations as deformation costs can

be included. Daniel (1983) found that the absence of elasticity may lead to overestimation of efficiency, as the costs of deformation are not included. The present model is therefore not the most accurate representation, but a compromise between simplified analytical/axisymmetric modelling and complex FSI modelling.

The advantage of the present model is that the 3D vorticity field can be evaluated without using axisymmetric or 2D approximations. This was confirmed by comparing the resulting dynamics and flow field of 2D and 3D WaterLily simulations. The 2D model underestimated the peak thrust generated during contraction (Figure 4.9a), resulting in a smaller translational velocity (Figure 4.9b). The contraction force peak was almost not present, although the forces during the expansion phase matched particularly well. Comparing the resulting flow fields of 3D (Figure 4.12) to 2D (Figure C.1) shows a completely different result as well. 2D vorticity behaved differently from 3D, although this may also result from the different velocity, which reduces the motion of the background grid and therefore how far the vortices move away from the body. Differences between 2D and 3D models are consistent with the work of Dabiri and Gharib (2003) and McHenry and Jed (2003), stating that 2D models cannot reproduce the actual wake dynamics. A comparison between a quarter and full geometry simulation showed that although the dynamics are similar, the wake differs. The wake field of the full 3D model presented asymmetries that were not observed in the wake field of the quarter 3D model. This difference is consistent when compared to the axisymmetric flow fields of Sahin et al. (2009), where the axisymmetric results match well, while the full 3D model deviates. This indicates that the quarter model enforces the axisymmetry condition. In contrast, the full 3D model allows the development of non-axisymmetric wake structures. This shows the benefit of the present 3D approach, which captures the full wake dynamics and computes a representative flow behaviour. However, the flow fields presented in this study should be analysed more thoroughly to fully assess the differences, as the underlying causes and implications of the observed instabilities have not been studied.

5.2. Computational Feasibility

This model avoided large domain sizes and high computational costs by employing a moving grid, symmetry, and Biot-Savart boundary conditions, as developed by Weymouth and Lauber (2024). By applying a moving frame, the *Sarsia tubulosa* geometry remained in place, while the velocity was applied to the background frame. This avoids large domain requirements in the translational direction with a forward-moving jellyfish that is capable of swimming multiple body lengths per stroke (Baldwin & Battista, 2021). Applying symmetrical boundary conditions compressed the domain size by a factor of 4, as simulating a quarter jellyfish suffices (Weymouth, 2025). The similarity between the hydrodynamic force for a full jellyfish and a half or quarter jellyfish with symmetry conditions proved the validity of this implementation (Figure 3.6). The imposed symmetry conditions in the quarter 3D model suppress asymmetric wake development, which must be accounted for in future vortex and wake studies. The Biot-Savart boundary conditions were applied to the outer boundaries to compress the overall domain size (Weymouth & Lauber, 2024) (Figure 4.2). Combining these techniques decreases the computational cost of simulations with this model. Improved computational performance of the model benefits future studies that aim to simulate large sets of kinematic configurations.

Convergence studies were conducted to determine the appropriate numerical settings for simulation. The instantaneous hydrodynamic force was used as the reference signal, from which the additional dynamics were computed. The convergence studies implied that the implemented simulation settings induce an error. A grid size of $D = 2^6$ was applied in the present studies (Figure 4.1), where the capabilities of this model were explored. However, a finer grid size should be considered in future studies, as the current grid size induces an RMSE of 0.08 compared to $D = 2^8$. Further refinement could increase this relative RMSE, although this could not be confirmed as finer grid sizes were not tested in this study due to computational limitations. A grid size of $D = 2^7$ resulted in reduced force peaks and therefore a reduced steady-state velocity. The numerical time step convergence study determined that simulating a grid size of $D = 2^6$ requires a small time step Δt of 0.05. Shorter Δt values resulted in increased hydrodynamic forces compared to longer time steps. As this behaviour was observed for both filtered and non-filtered forces, it was not fully attributed to the smoothing algorithm. It was also attributed to local pressures and unsteady force peaks being better resolved at smaller time steps. This indicates that strict time-step convergence of the hydrodynamic force could not be established, as temporal refinement

consistently altered the force balance. The simulations are therefore numerically demanding due to the combined complexity of the geometry and kinematics. The control-point motions, particularly in the velar region, induce high local advective velocities, thereby requiring a small time step to satisfy the CFL criterion.

5.3. Mechanics

5.3.1. Kinematic and Dynamic Validation

Kinematic and geometric agreement between the present model and the digitised frames in Sahin et al. (2009) was evaluated by visually overlaying the geometries at each frame time (Figure 4.4). With respect to motion, the model behaves correctly. However, the velum is wider and using linear splines between control points may introduce some sharp angles that could be avoided with higher-degree polynomials. Thickening of the velum and linear splines induced differences in cavity volume and velar opening diameter, quantified by comparing the present model to the data in Lipinski and Mohseni (2009) (Figure 4.5). The cavity volume and the velar opening diameter showed moderately similar behaviour to those in Lipinski and Mohseni (2009), with an NRMSE of 0.113.

Dynamic validation was quantified with the NRMSE of a set of instantaneous signals available in the literature. It was found that the resulting velocities of this model are similar to those described in Sahin et al. (2009) (Figure 4.6). The NRMSE of 0.203 [-] for velocity and 0.170 [-] for the force coefficient indicates moderate similarity. However, it implies that there are differences between the results of this CFD model and of Sahin et al. (2009). These deviations were attributed to the average phase difference $\bar{\Delta\phi}$ of 0.04 [-], inducing 37% of the error, increased velum thickness, and full 3D modelling instead of axisymmetrical.

A comparison of the instantaneous fineness ratio and the translational velocity to the data in Colin and Costello (2002) resulted in NRMSE values of 0.338 and 0.584, respectively. General signal behaviour was similar, but a significant difference in magnitude (Figure 4.7) was observed. Kinematic and dynamic behaviour during the motion cycle was comparable, with signal peaks occurring at similar moments. However, after $2-3$ motion cycles, phase mismatches were observed. It was found that applying prescribed kinematics idealises the swimming mode of *Sarsia tubulosa*, as, according to the experimental results of Colin and Costello (2002) and Dabiri et al. (2006), the motion period and duty cycle vary from actuation cycle to actuation cycle. Another finding was that the present model's velocity consistently overshoots the experimentally found velocity of Colin and Costello (2002) (Figure 4.7b). This trend was found in several other studies that constructed jellyfish models with a similar equation of motion (Colin & Costello, 1996; Colin & Costello, 2002; Daniel, 1983; McHenry & Jed, 2003). These dynamic overestimations have been attributed to sensitivity to shape assumptions, idealised kinematics and the absence of appendix drag (Dabiri & Gharib, 2003; McHenry & Jed, 2003). Dabiri and Gharib (2003) determined that jellyfish dynamics are sensitive to inaccurate kinematics modelling. Specifically, the hemisphere assumption for added mass and the absence of drag-inducing tentacles have been determined by Dabiri and Gharib (2003) and McHenry and Jed (2003) to influence the swimming dynamics. All these models have in common that they do not include the FSI effects, which is therefore a likely cause of the described differences. Without resolving the coupled interaction between fluid and deforming structure, the prescribed kinematics control the flow, but are not influenced by it. This decoupling removes fluid resistance and passive deformation, causing a continuous velocity overshoot. In contrast, models that incorporate deformation and elasticity effects, such as Park et al. (2015), approach the experimental data of Colin and Costello (2002). As the present model does not incorporate fully-coupled FSI and relies on prescribed kinematics, the observed velocity overshoot is consistent with the known limitations of such approaches.

5.3.2. Kinematic Variation and Force Decomposition

A kinematic variation study was conducted to benchmark model performance and identify issues. Kinematic variations were evaluated based on their COT, defined as the ratio of input power and acquired velocity in Bale et al. (2014), explicitly applied to jellyfish in Baldwin and Battista (2021). Duty cycle variation indicated a clear optimum for $0.4 < \gamma < 0.5$, with a COT of 0.10 (Figure 4.13a). Baldwin and Battista (2021) agrees with this optimal duty cycle range for a jellyfish with a motion period close to 1 [s]. In Peng and Alben (2012), a duty cycle of 0.5 was found as optimal. This duty cycle range differs from the

experimentally found duty cycle given in Colin and Costello (2002), which is 0.2 for the *Sarsia tubulosa*. This suggests that *Sarsia tubulosa* applies a non-optimal duty cycle for actuation in terms of COT. However, jellyfish use different actuation modes for predation and for swimming, meaning that jellyfish do not optimise their settings purely to minimise COT (Baldwin & Battista, 2021). Because jellyfish employ multi-objective optimisation during swimming, where efficiency alone does not dictate their behaviour, differences relative to experimental findings will always be present. This is a limitation of quantifying propulsive performance with efficiency metrics, as these always assume an idealised swimming mode.

The variable period length described in Colin and Costello (2002) and Dabiri et al. (2006) prompted a study on periodic variation and gliding interval. Elongated periods and long gliding intervals continuously improved the COT variable, resulting in extremely low COT values of up to 0.04. This resulted from a decrease in input power, while translational velocity remained significant (Figure 4.14, Figure 4.15). Baldwin and Battista (2021) determined that for longer motion periods, the largest COT reductions can be accomplished with duty cycle variation. They also report that higher frequencies yield smaller performance gains. The continuously decreasing COT over increasing periods and gliding intervals is therefore questionable. To determine the cause of this low COT, velocity behaviour was investigated for longer gliding intervals (Figure 4.19b). For each kinematic setting, an equilibrium is reached where the net force over 1 period equals 0, which results in the 'steady state' velocity. Similar behaviour was observed in the literature, where similar equations of motion were implemented, such as Colin and Costello (2002), Daniel (1983), and McHenry and Jed (2003), which also overestimated accelerations and velocities. Colin and Costello (2002) and McHenry and Jed (2003) attributed these discrepancies to the force assumptions in their model, as either an overestimated thrust or an underestimated drag force. The equation of motion was investigated to determine the cause of the overestimated velocity.

The major force contributions were studied separately: The viscous and pressure forces on the geometry, and the added mass, computed from different assumptions (Figure 4.10). A first note is that skin-friction drag was documented by Sahin et al. (2009) to be relatively small yet present during actuation cycles, a finding confirmed in this study. The drag force acting on this model during actuation and gliding was compared to the sphere drag of Hoerner (1965) (Figure 4.19a), an analytical assumption applied in Daniel (1983) and McHenry and Jed (2003). The results suggest that the drag force computed by WaterLily is in the correct order of magnitude. It was found that the pressure force dominates the viscous force for the actuating model. The added mass also had a significant influence, accounting for 35 % of the total force. This influence depends on the added mass coefficient, which is an uncertain quantity in this model and in similar *Sarsia tubulosa* modelling (Daniel, 1983). This has led to the use of (hemi-)sphere assumptions for added mass coefficients.

Increasing the added mass coefficient results in a larger volume of the surrounding fluid accelerating with the body. The relationship between body and fluid mass is hard to define (Colin & Costello, 1996). Hemisphere and sphere assumptions, both with (increasing coefficient) and without rigidly moving cavity volume (decreasing coefficient), were applied to the present model. Increased coefficients produced damped signals that still reached similar steady-state velocities, although the required period to reach this state increased (Figure 4.17). This confirms the findings of Daniel (1983) and McHenry and Jed (2003) that acceleration reaction dominates during acceleration, whereas drag dominates once the steady state is reached. It remains difficult to define a physically correct added mass coefficient for *Sarsia tubulosa*. A reasonable assumption is that the fluid at the body location is accelerated. This means that added mass is at least the volume occupied by the jellyfish as assumed in Sahin et al. (2009), if not higher (Daniel, 1983; McHenry & Jed, 2003). Nonetheless, similar steady-state velocities were acquired with different added mass coefficients.

5.3.3. Vortex Dynamics

A vortex dynamics study demonstrated similar wake behaviour to that described in Lipinski and Mohseni (2009) and Sahin et al. (2009), although deviations are present. This full 3D model was expected to represent vortex (ring) dynamics more accurately than reduced-order methods. Compared to the axisymmetrical approach of Sahin et al. (2009), similar sets of vortex rings are generated. A 'starting vortex ring' is formed during the contraction phase. In the present model, the vortex ring exhibited a longer trailing flow that remained attached for a longer period, and asymmetries in the vortex structure were observed. The vortex dynamics in the cavity were very similar, with a vortex ring moving inside the

cavity with each stroke, resulting in a pair of vortices after refilling. Both vortex rings stored within the cavity were ejected in the next contraction phase, which is not the case in Sahin et al. (2009), where one vortex ring remains. The uniform-like flow around the geometry generated by the forward velocity is similar. Sahin et al. (2009) reported that velum shape strongly influences vortex ring formation and the possibility for cavity vortices to interact with starting vortices. Therefore, differences in vortex dynamics are likely due to adjustments to this model's velum and the absence of enforced symmetry in the fully three-dimensional simulation. The comparison of velar opening diameter proved that in this model, it is slightly smaller during contraction. A smaller aperture may produce a stronger shear layer at the velar edge and prolong the ejection process, resulting in a longer trailing jet because the fluid requires more time to exit the cavity. In jet-propelled jellyfish, however, vortex interaction is generally not considered part of the propulsion mechanism. Instead, thrust is primarily generated by the momentum of the expelled jet, whereas passive thrust from interacting vortices is less important than in oblate species. Dabiri et al. (2006) confirms that the velar kinematics primarily serve to optimise vortices formed in the jet rather than affect the speed of the ejected flow.

The present model also supports the statements by Dabiri et al. (2006) and Lipinski and Mohseni (2009) that the flow structures within the subumbrellar cavity are very complex. Their dye visualisations of *Sarsia tubulosa* show the same vortex-ring formation, with the ejection of a primary vortex and an oppositely directed secondary vortex within the cavity. This induces a thrust spike in the opposite direction during the motion cycle. The velum traps the stopping vortex within the subumbrellar cavity and does not interact with the starting vortex, consistent with the present model. A difference is the trailing jet in the present model, which is less visible in their visualisations and exhibits three-dimensional asymmetry. Lipinski and Mohseni (2009) states that this trailing jet reduces the efficiency of momentum and energy transfer to the wake. A stretching vortex may indicate either an overly long contraction phase or numerical diffusion. In addition, a comparison was made to the dye visualisation in Dabiri et al. (2006), available in the reproducibility repository, regarding the very similar jellyfish type *Nemopsis bachei*. Interestingly, their dye is visible in a trailing jet similar to this model, although the main part is expelled with the vortex ring similar to Lipinski and Mohseni (2009).

5.4. Model Limitations

The developed model was subject to several limitations. Most notably, the missing elasticity and deformation forces. The exclusion of these forces from the equation of motion overestimates velocity. In addition, computing a representative COT parameter should include these forces. A clear limitation of this model is the implementation of such forces and, therefore, an accurate COT computation.

Smoothing algorithms were introduced to ensure continuity of control point motion and to maintain mass conservation (Figure 3.1) throughout the actuation cycle. In addition, the velar aperture was thickened to mitigate SDF noise and solver instability, which were attributed to thin geometries and sharp angles in Lauber et al. (2022). Such adjustments, although unavoidable, introduced deviations between this model and reality.

Implementing linear splines to connect the control points induced differences in cavity volume, as general jellyfish shapes are better described by higher-order functions (Dular et al., 2009). Higher-order polynomials smooth the sharp angles. Additionally, using a higher-order polynomial could reduce the number of control points, as it better matches the geometry curve. This also reduces computational cost, as it scales with the number of control points (Weymouth, 2025).

Issues in convergence are not necessarily a model limitation, but do limit the results acquired with this model. The results of the current study were not independent of the numerical time step and grid size, something that should be taken into account when reproducing these results or using them in future studies. A thorough time step and grid size convergence study should be conducted to find the optimal settings for this model.

6

Conclusions and Recommendations

6.1. Conclusions

The objective of this project was to develop a biologically consistent 3D model and kinematic control algorithm, and combine them in an efficiency study. The model was required to be computationally feasible, biologically consistent and capable of resolving 3D physics, such as vortex ring formation. It was aimed at avoiding analytical thrust and drag approximations commonly used in reduced-order approaches by incorporating hydrodynamic forces into the model. The development, validation and evaluation of a three-dimensional numerical model of an actuating *Sarsia tubulosa* was described. It was implemented in the WaterLily CFD framework, using a control point and NURBS geometry representation. A newly developed kinematic control algorithm controlled the bell motion by repositioning control points.

The resulting model captured the kinematic and geometric characteristics of *Sarsia tubulosa*, although some adjustments were required for numerical feasibility. Smoothing, filtering, and optimisation algorithms, in combination with thickening of the thin velum and linear control-point connecting splines, introduced discrepancies relative to the physical problem. Validation against literature data demonstrated that the geometry and kinematics match moderately well, quantified with normalised root-mean-square errors of 0.113 for cavity volume and velar opening diameter. Comparison of the resulting dynamics with an axisymmetric ALE solver yielded similar deviations with NRMSE values of 0.203 for the force coefficient and 0.170 for velocity. These differences are attributed to differences in the applied solver, geometrical characteristics and phase misalignment. Phase differences were caused by force filtering, causing up to 37% of the dynamics error. Comparison to experimental data confirmed a continuous overestimation of translational velocity and idealisation of kinematics. This idealisation results from applying prescribed kinematics.

This velocity overshoot confirmed findings from earlier jellyfish models, which used similar approaches to compute velocity. The absence of drag-inducing tentacles, the use of prescribed kinematics, and the rigid-body equation of motion, without elastic tissue modelling, likely cause these dynamical overshoots. A sensitivity analysis of the added mass coefficient confirmed previous findings that steady-state swimming is controlled by drag, whereas acceleration reaction dominated start-up effects. Therefore, inaccurate thrust or drag is a likely cause for a velocity overshoot. A comparison to the drag force of a sphere proved that the drag in the present model is of the right order of magnitude.

Kinematic variation studies resulted in an optimal duty cycle in the range $0.4 < \gamma < 0.5$ for minimising the COT. The actual duty cycle of *Sarsia tubulosa* was approximated as 0.2, suggesting that natural swimming is not optimised solely for efficiency. In reality, there are differences in actuation modes among ecological, feeding, and manoeuvrability that are likely to influence the duty cycle and related kinematics, which are not accurately captured by the COT metric. For varying consecutive motion periods and the addition of gliding intervals, a continuous decrease in COT was determined. This indicates that the present model favours long periods of coasting, which are attributed to velocity overshoot and underestimated drag due to missing appendages. Using the hydrodynamic force to compute input power does not include (elastic) deformation costs and can underestimate the COT. A combination of kinematic vari-

ations resulted in two optimal swimming modes, ($T_g = 0.00, T_2 = 2.00$) and ($T_g = 0.75, T_2 = 1.75$) [s]. However, given the limitations of the COT computations, this result must be interpreted with care.

Applying a moving reference frame, symmetry conditions, and Biot-Savart boundary conditions enhanced the computational feasibility of this model by reducing simulation time. Nevertheless, the symmetry conditions can suppress vortex asymmetries and instabilities, and therefore, wake evaluation should be conducted with the full jellyfish geometry. Combined with the absence of elasticity and appendage modelling, the present model's physical accuracy is constrained. In addition, the obtained results were not independent of the numerical time step and grid size. Thus, further refinement of the numerical settings may reduce the computed errors.

Overall, the present model is a computationally efficient three-dimensional numerical version of *Sarsia tubulosa*, appropriate for studying propulsive properties. It improves purely analytical approaches by resolving hydrodynamic forces from the stress resulting from the Navier-Stokes equations. However, it includes quantified deviations from literature in geometry and kinematic settings, which are attributed to the modelling compromises required to develop this model. While it was capable of capturing trends similar to those in the literature, the extreme efficiency of long coasting behaviour prevented exploration of optimal propulsive efficiencies through variation in motion cycle and by adding gliding intervals.

6.2. Recommendations for Future Work

Given the findings and conclusions of the present study, several recommendations for future work are made, concerning further development of the model or applying it to other studies. Future research applying this model to kinematic and propulsive studies should consider the assumptions and issues raised in this report. It is advised to conduct a thorough convergence study on the time step and grid size before applying the model in other studies, ensuring that the results are independent of changes in these numerical settings.

6.2.1. Elaborate Sensitivity Analyses

Future research should focus on solving the stated problems of velocity overshoot and extremely low COT values for coasting behaviour. This study devotes a brief section to exploring this problem, which should be extended to determine the underlying causes of the identified problems. A possible extension of the model is to incorporate tentacle-induced drag with an iteratively defined drag coefficient. The drag coefficient of these appendages can be determined through a sensitivity study, using the experimental data as a reference value.

6.2.2. Elasticity Modelling

The extension of the rigid-body force equation with force contributions from deformation and elasticity should be explored. This improves force accuracy and facilitates accurate computation of the COT metric, including the energy cost of deformation. The lack of passive energy and elasticity modelling overestimates efficiency and warrants further study. A reproduction of the methods described in Park et al. (2015) is a good starting point.

6.2.3. Higher-order Geometric Representation

Exploring higher-order geometric representations to reduce the number of control points and the sharp angles resulting from linear splines could benefit the model. A reduced number of control points reduces the computational costs of simulation with this model, while a higher-order polynomial better represents the jellyfish geometry. A sensitivity study, in which different-order polynomials are compared, should yield an optimal configuration for these model aspects.

6.2.4. Velum and Vorticity Studies

A refined grid around the velum and a close look at the (numerical) dynamics at those locations may contribute to understanding the vorticity effects identified in this model. The effect of velar kinematics on the long trailing jet and large jet size can be explored. The possibility of velar kinematic variation in 3D is unique to the present model and contributes to jellyfish vortex formation studies. The influence of the velum on vortex formation requires further investigation.

A detailed analysis of vorticity dynamics would be a valuable extension of the present work and contribute to the field of jellyfish modelling. Given the current lack of fully developed three-dimensional models and the demonstrated differences between symmetry-based and full three-dimensional modelling in the resulting vorticity fields, such work would be beneficial.

6.2.5. Increasing Kinematic Datasets

Exploring the kinematics of the *Sarsia tubulosa* could benefit from larger datasets. The presented studies could be extended by using finer increments between the kinematic settings. Additional parameters can be varied and studied, such as the fineness ratio, velum size and kinematics, elasticity and drag coefficients.

6.2.6. Reinforcement Learning

Adding a reinforcement learning algorithm enables variation of kinematic parameters in small increments based on the instantaneous physics. To apply reinforcement learning efficiently in kinematic variation, it may be beneficial to redesign the kinematics algorithm as a closed-loop system. The system could then continuously feed back data to the RL algorithm, which applies a certain (efficient) kinematic setting for that situation.

References

Alben, S., Miller, L., & Peng, J. (2013). Efficient kinematics for jet-propelled swimming. *Journal of Fluid Mechanics*, *733*, 100–133. https://doi.org/https://doi.org/10.1017/jfm.2013.434

Bajcar, T., Malačič, V., Malej, A., & Širok, B. (2009). Kinematic properties of the jellyfish aurelia sp. *Jellyfish Blooms: Causes, Consequences, and Recent Advances: Proceedings of the Second International Jellyfish Blooms Symposium, held at the Gold Coast, Queensland, Australia, 24–27 June, 2007*, 279–289. https://doi.org/10.1007/s10750-008-9589-4

Baldwin, T., & Battista, N. A. (2021). Hopscotching jellyfish: Combining different duty cycle kinematics can lead to enhanced swimming performance. *Bioinspiration & Biomimetics*, *16*(6), 066021. https://doi.org/10.1088/1748-3190/ac2afe

Bale, R., Hao, M., Bhalla, A. P. S., & Patankar, N. A. (2014). Energy efficiency and allometry of movement of swimming and flying animals. *Proceedings of the National Academy of Sciences*, *111*(21), 7517–7521. https://doi.org/https://doi.org/10.1073/pnas.1310544111

Baliga, B., & Patankar, S. (1980). A new finite-element formulation for convection-diffusion problems. *Numerical Heat Transfer*, *3*(4), 393–409. https://doi.org/https://doi.org/10.1080/01495728008961767

Chapman, D. M. (1999). Microanatomy of the bell rim of aurelia aurita (cnidaria: Scyphozoa). *Canadian journal of zoology*, *77*(1), 34–46. https://doi.org/https://doi.org/10.1139/z98-193

Cirak, F., Ortiz, M., & Schröder, P. (2000). Subdivision surfaces: A new paradigm for thin-shell finite-element analysis. *International Journal for Numerical Methods in Engineering*, *47*(12), 2039–2072. https://doi.org/https://doi.org/10.1002/(SICI)1097-0207(20000430)47:12<2039::AID-NME872>3.0.CO;2-1

Colin, S., & Costello, J. H. (1996). Relationship between morphology and hydrodynamics during swimming by the hydromedusae aequorea victoria and aglantha digitale. *Arts and Sciences Faculty Publications Roger Williams University*.

Colin, S. P., & Costello, J. H. (2002). Morphology, swimming performance and propulsive mode of six co-occurring hydromedusae. *Journal of experimental biology*, *205*(3), 427–437. https://doi.org/https://doi.org/10.1242/jeb.205.3.427

Collis, S. S., Ghayour, K., Heinkenschloss, M., Ulbrich, M., & Ulbrich, S. (2001). Numerical solution of optimal control problems governed by the compressible navier-stokes equations. *Optimal Control of Complex Structures: International Conference in Oberwolfach, June 4–10, 2000*, 43–55. https://doi.org/10.1007/978-3-0348-8148-7_4

Collis, S. S., Joslin, R. D., Seifert, A., & Theofilis, V. (2004). Issues in active flow control: Theory, control, simulation, and experiment. *Progress in aerospace sciences*, *40*(4-5), 237–289. https://doi.org/https://doi.org/10.1016/j.paerosci.2004.06.001

Costello, J. H., Colin, S. P., & Dabiri, J. O. (2008). Medusan morphospace: Phylogenetic constraints, biomechanical solutions, and ecological consequences. *Invertebrate Biology*, *127*(3), 265–290. https://doi.org/https://doi.org/10.1111/j.1744-7410.2008.00126.x

Costello, J. H., Colin, S. P., Dabiri, J. O., Gemmell, B. J., Lucas, K. N., & Sutherland, K. R. (2021). The hydrodynamics of jellyfish swimming. *Annual Review of Marine Science*, *13*(1), 375–396.

Dabiri, J. O., Colin, S. P., & Costello, J. H. (2006). Fast-swimming hydromedusae exploit velar kinematics to form an optimal vortex wake. *Journal of Experimental Biology*, *209*(11), 2025–2033. https://doi.org/doi:10.1242/jeb.02242

Dabiri, J. O., Colin, S. P., & Costello, J. H. (2007). Morphological diversity of medusan lineages constrained by animal–fluid interactions. *Journal of Experimental Biology*, *210*(11), 1868–1873. https://doi.org/https://doi.org/10.1242/jeb.003772

Dabiri, J. O., Colin, S. P., Costello, J. H., & Gharib, M. (2005). Flow patterns generated by oblate medusan jellyfish: Field measurements and laboratory analyses. *Journal of Experimental Biology*, *208*(7), 1257–1265. https://doi.org/https://doi.org/10.1146/annurev-marine-031120-091442

Dabiri, J. O., & Gharib, M. (2003). Sensitivity analysis of kinematic approximations in dynamic medusan swimming models. *Journal of Experimental Biology*, *206*(20), 3675–3680. https://doi.org/https://doi.org/10.1242/jeb.00597

Daniel, T. L. (1983). Mechanics and energetics of medusan jet propulsion. *Canadian Journal of Zoology*, *61*(6), 1406–1420. https://doi.org/https://doi.org/10.1139/z83-190

Daniel, T. L. (1995). Invertebrate swimming: Integrating internal and external mechanics. *Symposia of the Society for Experimental Biology*, *49*, 61–89.

Demont, M. E., & Gosline, J. M. (1988). Mechanics of jet propulsion in the hydromedusan jellyfish, polyorchis penicillatus: I. mechanical properties of the locomotor structure. *Journal of Experimental Biology*, *134*(1), 313–332. https://doi.org/https://doi.org/10.1242/jeb.134.1.313

Dobrinsky, A., & Collis, S. (2000). Adjoint parabolized stability equations for receptivity prediction. *Fluids 2000 Conference and Exhibit*, 2651. https://doi.org/https://doi.org/10.2514/6.2000-2651

Dular, M., Bajcar, T., & Širok, B. (2009). Numerical investigation of flow in the vicinity of a swimming jellyfish. *Engineering Applications of Computational Fluid Mechanics*, *3*(2), 258–270. https://doi.org/https://doi.org/10.1080/19942060.2009.11015269

Eldredge, J. D. (2007). Numerical simulation of the fluid dynamics of 2d rigid body motion with the vortex particle method. *Journal of Computational Physics*, *221*(2), 626–648. https://doi.org/https://doi.org/10.1016/j.jcp.2006.06.038

Feitl, K., Millett, A., Colin, S., Dabiri, J. O., & Costello, J. H. (2009). Functional morphology and fluid interactions during early development of the scyphomedusa aurelia aurita. *The Biological Bulletin*, *217*(3), 283–291. https://doi.org/10.1086/BBLv217n3p283

Frame, J., Lopez, N., Curet, O., & Engeberg, E. D. (2018). Thrust force characterization of free-swimming soft robotic jellyfish. *Bioinspiration & biomimetics*, *13*(6), 064001. https://doi.org/10.1088/1748-3190/aadcb3

Gemmell, B. J., Colin, S. P., & Costello, J. H. (2018). Widespread utilization of passive energy recapture in swimming medusae. *Journal of Experimental Biology*, *221*(1), jeb168575. https://doi.org/https://doi.org/10.1242/jeb.168575

Gemmell, B. J., Colin, S. P., Costello, J. H., & Dabiri, J. O. (2015). Suction-based propulsion as a basis for efficient animal swimming. *Nature communications*, *6*(1), 8790. https://doi.org/10.1038/ncomms9790

Gemmell, B. J., Costello, J. H., Colin, S. P., Stewart, C. J., Dabiri, J. O., Tafti, D., & Priya, S. (2013). Passive energy recapture in jellyfish contributes to propulsive advantage over other metazoans. *Proceedings of the National Academy of Sciences*, *110*(44), 17904–17909. https://doi.org/https://doi.org/10.1073/pnas.1306983110

Gemmell, B. J., Dabiri, J. O., Colin, S. P., Costello, J. H., Townsend, J. P., & Sutherland, K. R. (2021). Cool your jets: Biological jet propulsion in marine invertebrates. *Journal of Experimental Biology*, *224*(12), jeb222083. https://doi.org/https://doi.org/10.1242/jeb.222083

Gemmell, B. J., Du Clos, K. T., Colin, S. P., Sutherland, K. R., & Costello, J. H. (2021). The most efficient metazoan swimmer creates a 'virtual wall'to enhance performance. *Proceedings of the Royal Society B*, *288*(1942), 20202494. https://doi.org/https://doi.org/10.1098/rspb.2020.2494

Gemmell, B. J., Troolin, D. R., Costello, J. H., Colin, S. P., & Satterlie, R. A. (2015). Control of vortex rings for manoeuvrability. *Journal of The Royal Society Interface*, *12*(108), 20150389. https://doi.org/http://dx.doi.org/10.1098/rsif.2015.0389

Giorgio-Serchi, F., & Weymouth, G. D. (2016). Drag cancellation by added-mass pumping. *Journal of fluid Mechanics*, *798*, R3. https://doi.org/https://doi.org/10.1017/jfm.2016.353

Herschlag, G., & Miller, L. (2011). Reynolds number limits for jet propulsion: A numerical study of simplified jellyfish. *Journal of theoretical biology*, *285*(1), 84–95. https://doi.org/https://doi.org/10.1016/j.jtbi.2011.05.035

Hoerner, S. F. (1965). Fluid dynamic drag. *Midland Park, NJ*, 16–35.

Hoover, A., & Miller, L. (2015). A numerical study of the benefits of driving jellyfish bells at their natural frequency. *Journal of theoretical biology*, *374*, 13–25. https://doi.org/https://doi.org/10.1016/j.jtbi.2015.03.016

Hoover, A. P., Griffith, B. E., & Miller, L. A. (2017). Quantifying performance in the medusan mechanospace with an actively swimming three-dimensional jellyfish model. *Journal of Fluid Mechanics*, *813*, 1112–1155. https://doi.org/https://doi.org/10.1017/jfm.2017.3

Hoover, A. P., Porras, A. J., & Miller, L. A. (2019). Pump or coast: The role of resonance and passive energy recapture in medusan swimming performance. *Journal of Fluid Mechanics*, *863*, 1031–1061. https://doi.org/https://doi.org/10.1017/jfm.2018.1007

Joshi, S. N., & Gujarathi, Y. S. (2016). A review on active and passive flow control techniques. *International Journal on Recent Technologies in Mechanical and Electrical Engineering*, *3*(4), 1–6.

Kim, K., Baek, S.-J., & Sung, H. J. (2002). An implicit velocity decoupling procedure for the incompressible navier–stokes equations. *International journal for numerical methods in fluids*, *38*(2), 125–138. https://doi.org/https://doi.org/10.1002/fld.205

Lauber, M., Weymouth, G. D., & Limbert, G. (2022). Immersed boundary simulations of flows driven by moving thin membranes. *Journal of Computational Physics*, *457*, 111076. https://doi.org/10.1016/j.jcp.2022.111076

Leclère, L., & Röttinger, E. (2017). Diversity of cnidarian muscles: Function, anatomy, development and regeneration. *Frontiers in cell and developmental biology*, *4*, 157. https://doi.org/https://doi.org/10.3389/fcell.2016.00157

Lipinski, D., & Mohseni, K. (2009). Flow structures and fluid transport for the hydromedusae sarsia tubulosa and aequorea victoria. *Journal of Experimental Biology*, *212*(15), 2436–2447. https://doi.org/https://doi.org/10.1242/jeb.026740

McHenry, M. J., & Jed, J. (2003). The ontogenetic scaling of hydrodynamics and swimming performance in jellyfish (aurelia aurita). *Journal of experimental biology*, *206*(22), 4125–4137. https://doi.org/https://doi.org/10.1242/jeb.00649

Mecanna, S., Loisy, A., & Eloy, C. (2025). A critical assessment of reinforcement learning methods for microswimmer navigation in complex flows. *arXiv preprint arXiv:2505.05525*. https://doi.org/https://doi.org/10.1140/epje/s10189-025-00522-2

Megill, W. M., Gosline, J. M., & Blake, R. W. (2005). The modulus of elasticity of fibrillin-containing elastic fibres in the mesoglea of the hydromedusa polyorchis penicillatus. *Journal of Experimental Biology*, *208*(20), 3819–3834. https://doi.org/https://doi.org/10.1242/jeb.01765

Miles, J. G., & Battista, N. A. (2019). Don't be jelly: Exploring effective jellyfish locomotion. *arXiv preprint arXiv:1904.09340*.

Oppenheim, A. V., & Schafer, R. W. (2010). *Discrete-time signal processing* (3rd ed.). Prentice Hall.

Pallasdies, F., Goedeke, S., Braun, W., & Memmesheimer, R.-M. (2019). From single neurons to behavior in the jellyfish aurelia aurita. *elife*, *8*, e50084. https://doi.org/10.7554/eLife.50084

Park, S. G., Chang, C. B., Huang, W.-X., & Sung, H. J. (2014). Simulation of swimming oblate jellyfish with a paddling-based locomotion. *Journal of Fluid Mechanics*, *748*, 731–755. https://doi.org/https://doi.org/10.1017/jfm.2014.206

Park, S. G., Kim, B., Lee, J., Huang, W.-X., & Sung, H. J. (2015). Dynamics of prolate jellyfish with a jet-based locomotion. *Journal of Fluids and Structures*, *57*, 331–343. https://doi.org/https://doi.org/10.1016/j.jfluidstructs.2015.07.002

Peng, J., & Alben, S. (2012). Effects of shape and stroke parameters on the propulsion performance of an axisymmetric swimmer. *Bioinspiration & biomimetics*, *7*(1), 016012. https://doi.org/10.1088/1748-3182/7/1/016012

Peskin, C. S. (2002). The immersed boundary method. *Acta numerica*, *11*, 479–517. https://doi.org/https://doi.org/10.1017/S0962492902000077

Peterson, J. (1990, June). *Albert technical memo #5: How to use knot vectors* (tech. rep.) (Internal technical memorandum). Apple Computer.

Rabault, J., Kuchta, M., Jensen, A., Réglade, U., & Cerardi, N. (2019). Artificial neural networks trained through deep reinforcement learning discover control strategies for active flow control. *Journal of fluid mechanics*, *865*, 281–302. https://doi.org/https://doi.org/10.1017/jfm.2019.62

Rabault, J., Ren, F., Zhang, W., Tang, H., & Xu, H. (2020). Deep reinforcement learning in fluid mechanics: A promising method for both active flow control and shape optimization. *Journal of Hydrodynamics*, *32*(2), 234–246. https://doi.org/https://doi.org/10.1007/s42241-020-0028-y

Ren, F., Rabault, J., & Tang, H. (2021). Applying deep reinforcement learning to active flow control in weakly turbulent conditions. *Physics of Fluids*, *33*(3). https://doi.org/https://doi.org/10.1063/5.0037371

Sahin, M., & Mohseni, K. (2009). An arbitrary lagrangian–eulerian formulation for the numerical simulation of flow patterns generated by the hydromedusa aequorea victoria. *Journal of Computational Physics*, *228*(12), 4588–4605. https://doi.org/https://doi.org/10.1016/j.jcp.2009.03.027

Sahin, M., Mohseni, K., & Colin, S. P. (2009). The numerical comparison of flow patterns and propulsive performances for the hydromedusae sarsia tubulosa and aequorea victoria. *Journal of Experimental Biology*, *212*(16), 2656–2667. https://doi.org/https://doi.org/10.1242/jeb.025536

Schaadt, M., Widmer, C. L., & Sowinski, N. (2017). Jellyfish. *Marine ornamental species aquaculture*, 457–473.

Sotiropoulos, F., & Yang, X. (2014). Immersed boundary methods for simulating fluid–structure interaction. *Progress in Aerospace Sciences*, *65*, 1–21. https://doi.org/https://doi.org/10.1016/j.paerosci.2013.09.003

Villanueva, A., Vlachos, P., & Priya, S. (2014). Flexible margin kinematics and vortex formation of aurelia aurita and robojelly. *PLoS One*, *9*(6), e98310. https://doi.org/https://doi.org/10.1371/journal.pone.0098310

von Montfort, G. M., Costello, J. H., Colin, S. P., Morandini, A. C., Migotto, A. E., Maronna, M. M., Reginato, M., Miyake, H., & Nagata, R. M. (2023). Ontogenetic transitions, biomechanical trade-offs and macroevolution of scyphozoan medusae swimming patterns. *Scientific Reports*, *13*(1), 9760. https://doi.org/https://doi.org/10.1038/s41598-023-34927-w

Wang, X., Liu, S., Yu, Y., Yue, S., Liu, Y., Zhang, F., & Lin, Y. (2023). Modeling collective motion for fish schooling via multi-agent reinforcement learning. *Ecological Modelling*, *477*, 110259. https://doi.org/https://doi.org/10.1016/j.ecolmodel.2022.110259

Weymouth. (2025). *Parametricbodies.jl* [GitHub repository]. https://github.com/WaterLily-jl/ParametricBodies.jl

Weymouth, G. D., & Font, B. (2025). Waterlily. jl: A differentiable and backend-agnostic julia solver for incompressible viscous flow around dynamic bodies. *Computer Physics Communications*, 109748. https://doi.org/https://doi.org/10.1016/j.cpc.2025.109748

Weymouth, G. D., & Lauber, M. (2024). Using biot-savart to shrink eulerian domains while maintaining or improving external flow accuracy. https://doi.org/https://doi.org/10.48550/arXiv.2404.09034

Weymouth, G., & Yue, D. K. (2011). Boundary data immersion method for cartesian-grid simulations of fluid-body interaction problems. *Journal of Computational Physics*, *230*(16), 6233–6247. https://doi.org/https://doi.org/10.1016/j.jcp.2011.04.022

Wilson, M. M., & Eldredge, J. D. (2011). Performance improvement through passive mechanics in jellyfish-inspired swimming. *International Journal of Non-Linear Mechanics*, *46*(4), 557–567. https://doi.org/https://doi.org/10.1016/j.ijnonlinmec.2010.12.005

Xiao, J., Duan, J., & Yu, J. (2013). Design and implementation of a novel biomimetic robotic jellyfish. *2013 IEEE International Conference on Robotics and Biomimetics (ROBIO)*, 988–993. https://doi.org/10.1109/ROBIO.2013.6739592

Zachariah, T., & Mitchell, M. A. (2006). Invertebrates. In M. A. Mitchell & T. N. Tully (Eds.), *Manual of exotic pet practice* (pp. 11–38). Elsevier.

Zimmerman, K. L., Jamshidi, A. D., Buckenberger, A., & Satterlie, R. A. (2019). Organization of the subumbrellar musculature in the ephyra, juvenile, and adult stages of aurelia aurita medusae. *Invertebrate Biology*, *138*(3), e12260. https://doi.org/https://doi.org/10.1111/ivb.12260

A

Statistical Convergence Algorithm

```
"""
    find_stationary_index(
        signal;
        window_size,
        tol_mean = 1e-3,
        tol_std = 1e-3,
        n_consecutive = 3
    )

Finds the index after which a signal is statistically stationary
based on windowed mean and standard deviation convergence.
"""
function find_stationary_index(
    signal::AbstractVector;
    window_size::Int,
    tol_mean::Float64=1e-3,
    tol_std::Float64=1e-3,
    n_consecutive::Int=3
)
    n = length(signal)
    nwin = fld(n, window_size)

    means = zeros(nwin)
    stds = zeros(nwin)

    # Compute window statistics
    for i in 1:nwin
        w = signal[(i-1)*window_size+1:i*window_size]
        means[i] = mean(w)
        stds[i] = std(w)
    end

    count = 0
    for i in 2:nwin
        dmean = abs(means[i] - means[i-1]) / max(abs(means[i-1]), eps())
        dstd = abs(stds[i] - stds[i-1]) / max(stds[i-1], eps())

        if dmean < tol_mean && dstd < tol_std
            count += 1
            if count   n_consecutive
                # Return index in original signal
                return (i - n_consecutive) * window_size + 1
```

```
            end
        else
            count = 0
        end
    end

    return nothing  # no stationary region found
end
```

B

Unfiltered Force Convergence

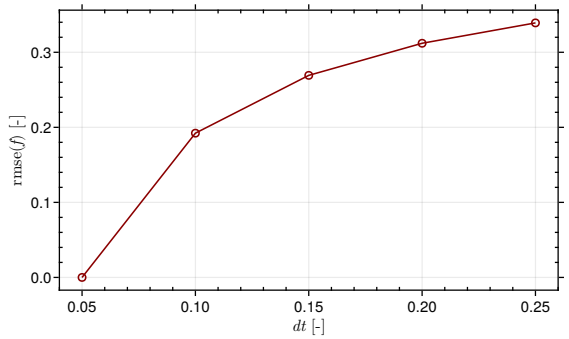

(a) The root mean square error of the unfiltered hydrodynamic force over varying time step Δt, using the smallest time step as a 'truth' value.

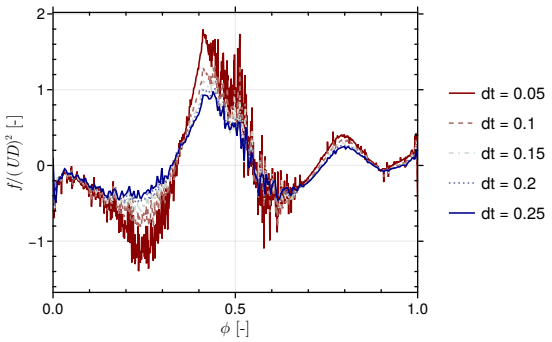

(b) Variation of the unfiltered hydrodynamic force over time for varying time steps.

Figure B.1: Convergence of the unfiltered force signal for varying time steps.

C

Vorticity Fields of Two-Dimensional Model

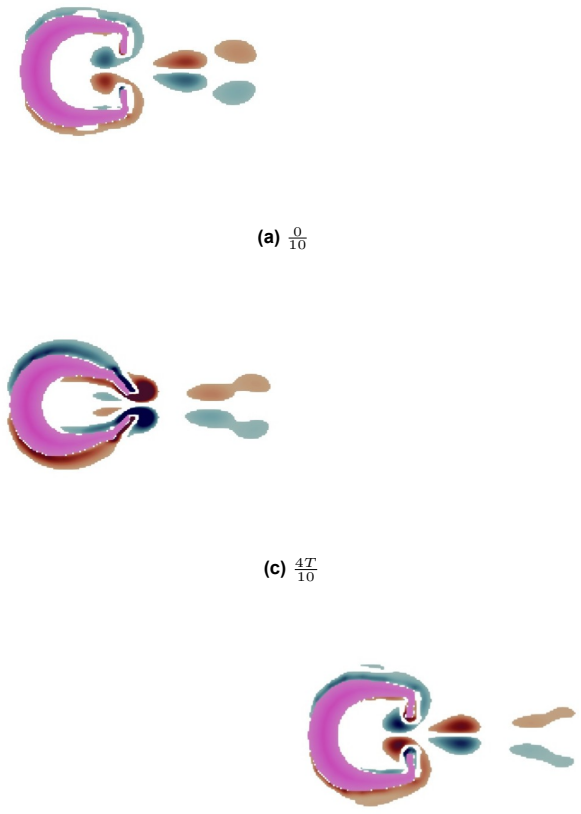

(a) $\frac{0}{10}$ **(b)** $\frac{2T}{10}$

(c) $\frac{4T}{10}$ **(d)** $\frac{6T}{10}$

(e) $\frac{8T}{10}$

Figure C.1: Vorticity fields of one evolved motion cycle of the two-dimensional model.

D

Vorticity Fields of Quarter Model

(a) t_0

(b) $t_0 + \frac{2T}{10}$

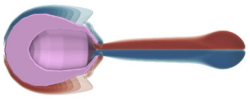

(c) $t_0 + \frac{4T}{10}$

(d) $t_0 + \frac{6T}{10}$

(e) $t_0 + \frac{8T}{10}$

Figure D.1: Vorticity contours of the quarter 3D model at several time steps in 1 fully evolved motion cycle.